DTU Wind

Modeling of multi-rotor wind farms

Yann Xavier Frank Birnie-Scott

DTU Wind-M-0578
July 2023

Author: Yann Xavier Frank Birnie-Scott

DTU Wind-M-0578
July 2023

Title:
Modeling of multi-rotor wind farms

Project period:
November 2022 - July 2023

ECTS: 45

Education: Master of Science

Supervisor(s):

Paul van der Laan
Mads Chr. Baungaard
DTU Wind and Energy Systems

Dries Allerts
TUDelft

Mikkel Kiilerich Østerlund
Vestas Wind System A/S

Remarks:
This report is submitted as partial fulfillment of the requirements for graduation in the above education at the Technical University of Denmark.

Technical University of Denmark
Department of Wind and Energy Systems
Frederiksborgvej 399
DK-4000 Roskilde
www.wind.dtu.dk

Acknowledgement

Thanks to all of those who made this possible. Thanks to the ones I shared laughs and tears with and the ones that unconditionally love and support me.

Special thanks to Paul and Mads from whom I have learned a lot and were vital for the development of this thesis.

To my master colleagues and peers, strive for acting in an eco-friendly way.

Yann Birnie-Scott
København, July 2023

Merci pour les roses, merci pour les épines.

Jean d'Ormesson

Abstract

The recurred idea of developing multi-rotor wind turbines has led to the need of more accurate surrogate wake models which allow for a fast annual energy production (AEP) calculation and further understanding of the aerodynamic power losses of multi-rotor wind turbines.

The present thesis develops a surrogate wake model of a multi-rotor-two turbine validated against computational fluid dynamics (CFD) simulations of type RANS-AD. The outcome is a superposition model of an analytical representation of the wake which base function coefficients are stored in look-up tables as a function of the wind inflow conditions affecting the turbine. The derived surrogate model is able to predict the overall wind farm efficiency with more than 90% accuracy while compared to the RANS-AD model.

Towards the end of the thesis, a comparison between a single-rotor wind farm of 18 V29 turbines and a multi-rotor wind farm composed by nine 2R-V29 turbines (hypothetical turbine) is evaluated through RANS-AD simulations within the same wind-farm area. The energy ouput showed to be highly dependent on the wind-farm geometry, but the wind direction average suggest that 5% more energy yield is obtained from the multi-rotor-farm for velocities below rated speed.

Contents

Nomenclature **vii**

1 Introduction **1**
1.1 Global and local coordinate systems . . . 2
1.2 Self-similarity . . . 3
1.3 State of the art . . . 3
1.3.1 Atmospheric Boundary Layer structure . . . 3
1.3.2 Analytical models of the wake velocity deficit . . . 4
1.3.3 Velocity deficit superposition models . . . 6
1.3.4 Analytical models of the wake added turbulence . . . 7
1.3.5 Added turbulence intensity superposition methods . . . 8

2 Simulation setup **9**
2.1 Governing equations and turbulence model . . . 9
2.1.1 RANS . . . 10
2.1.2 Turbulence model k-ε-f_P . . . 10
2.2 Inflow model of an atmospheric surface layer . . . 10
2.3 Boundary conditions . . . 11
2.4 Solver . . . 13
2.5 Wind turbines . . . 14
2.6 Actuator disk . . . 14
2.7 Mesh . . . 15
2.7.1 Mesh dependency study . . . 16
2.7.2 Single multi-rotor turbine simulation . . . 19
2.7.3 Four inline turbines simulations . . . 19
2.7.4 Wind farm simulations . . . 20

3 2R-V29 wake and model fitting **21**
3.1 RANS of a single MR2 . . . 22
3.2 Analytical model fitting . . . 22
3.3 Power relationship with U_∞ and I_∞ . . . 23

4 Wake superposition model **26**
4.1 Superposition method . . . 26
4.2 Four 2R-V29 turbines inline . . . 28

5 Multi-rotor wind farm modeling **33**
5.1 Existing engineering wake models . . . 33
5.2 Multi-rotor wind farm results . . . 34

6 Single-rotor wind farm vs. multi-rotor wind farm **37**
6.1 Single-rotor wind farm results . . . 38
6.2 Power output comparison . . . 38
6.3 Discussion . . . 42

7 Conclusion **43**
7.1 Future work . . . 44

Bibliography **45**

A Test-run with a single Vestas 4R-V29 **49**

B 2R-V29 wake model **51**
B.1 Algorithm used to build the look-up tables $\Psi(I_\infty, U_\infty, \hat{x})$ . . . 51

B.2 Surrogate model compared to RANS model on a single 2R-V29 turbine 51

C Wake superposition model **57**
C.1 Computing $I_{\infty,i}$ and $U_{\infty,i}$ from the $z = z_h$ plane 57
C.1.1 Computing $I_{\infty,i}$ 57
C.1.2 Computing $U_{\infty,i}$ 59
C.2 I^+ superposition model 59
C.3 $\Delta U/U_\infty$ superposition model 63

D Multi-rotor wind farm model vs RANS, additional results **65**

Nomenclature

Abbreviations

Abbreviation	Definition
ABL	Atmospheric Boundary Layer
AEP	Annual energy production
ASL	Atmospheric Surface Layer
CFD	Computational Fluid Dynamics
DTU	Technical University of Denmark
LUT	Look-up table
MR2	Multi-Rotor wind turbine with two rotors at equal height
MR4	Multi-Rotor wind turbine with two pairs of rotors at two different heights
MRWT	Multi-Rotor Wind Turbine
PWE	PyWakeEllipSys [DTU Wind and Energy Systems, 2023]
SRWT	Single-rotor wind turbine
TKE	Turbulent kinetic energy (k)

Symbols

Symbol	Definition	Unit
A_0	Rotor area of the V29 turbine	[m^2]
C_P	Power coefficient	[-]
C_T	Thrust coefficient	[-]
D_0	V29 turbine diameter	[m]
f_v	Non-dimensional volumetric forces normalized by $\rho \mathscr{U}^2 \mathscr{L}^{-1}$	[-]
I	Turbulence intensity based on the turbulent kinetic energy (k)	[-]
I_∞	Turbulence intensity at the inlet of the CFD, at $z = z_{\text{ref}}$	[-]
$I_{\infty,i}$	Free-stream turbulence intensity of the i^{th} turbine at z_h	[-]
I^+	Added turbulence intensity	[-]
$\mathscr{L}$	Characteristic length scale	[m]
N_{CD}	Cells per diameter	[-]
p	Non-dimensional mean pressure normalized by $\rho \mathscr{U}^2$	[-]
P	Wind turbine output power	[W]
Re	Reynolds number	[-]
S	Spatial scale parameter	[m]
t	Non-dimensional time normalized by $\mathscr{T}$	[-]
$\mathscr{T}$	Characteristic time scale	[s]
$\mathscr{U}$	Characteristic velocity scale	[m s^{-1}]
u_i	Non-dimensional mean velocity component i (normalized by $\mathscr{U}$)	[-]
U_∞	Inflow mean velocity at z_{ref} at the inlet of the CFD domain	[m s^{-1}]
$U_{\infty,i}$	Free-stream velocity of the i^{th} turbine at z_h	[m s^{-1}]
x_i	i coordinate on the main Cartesian reference system	[m]
$\hat{x_i}$	i coordinate on the local Cartesian reference system	[m]
z_0	Roughness length	[m]

Symbol	Definition	Unit
z_1	Cell center height of the closest cell to the bottom wall	[m]
z_h	Hub height	[m]
z_{ref}	Reference height of the specified U_∞ and I_∞, in general $z_{\text{ref}} = z_h$	[m]
Δ_1	Cell length within the wake refinement box	[m]
ε	Non-dimensional dissipation of turbulent kinetic energy normalized by $\mathscr{U}^2\mathscr{T}^{-1}$	[-]
k	Non-dimensional turbulent kinetic energy normalized by $\mathscr{U}^2$	[-]
λ	Tip speed ratio	[-]
μ	Dynamic viscosity	[Pa s]
ν	Kinematic viscosity	[m^2s^{-1}]
ν_t	Eddy viscosity	[m^2s^{-1}]
ρ	Density	[kg m^{-3}]
τ_w	Wall friction stress	[Pa]
u_τ	Friction velocity	[m s^{-1}]
Ψ	Look-up table symbol	[-]

1 Introduction

Wind is a vital energy source to meet future energy needs while mitigating the effects of climate change and ensuring energy security. It is a profitable renewable resource which is expected to keep on developing substantially all over the world.

Energy security concerns caused by Russias invasion of Ukraine have motivated countries to increasingly turn to renewables such as wind and solar to reduce reliance on imported fossil fuels, whose prices have spiked dramatically. Global renewable power capacity is now expected to grow by 2 400 GW over the 2022-2027 period, an amount equal to the entire power capacity of China today, according to [IEA, 2022]. This massive expected increase is 30% higher than the amount of growth forecasted in 2021, highlighting how quickly governments have thrown additional policy weight behind renewables. Actual geopolitical events in Europe have led to ambitious renewable energy targets, which account for almost 95% of the increase in global power capacity before 2026 [IEA, 2022]. Meeting these targets demands a substantial increase in renewable capacity in the near future, including in wind energy. This not only implies the planning and installation of new wind farms, but also the design of more efficient ones.

Figure 1.1: Vestas 4R-V29 multi-rotor wind turbine [van der Laan et al., 2019].

The earliest concept of multi-rotor wind turbine (MRWT) dates back from 1874 where Danish multi-rotor-two turbines were used to pump water [Verma, 2014, Baungaard, 2019]. A MRWT has several wind turbine rotors mounted on a single support structure as seen in Figure 1.1. The initial motivation for making multi-rotors appeared in the difficulty of making very large blades due to technology limitations, this was overcome by modern glass composites and thus the multi-rotor idea was left aside until recently [Verma, 2014]. Nowadays, the long blades dimension are rising manufacturing costs and limiting their transport to be maritime exclusive. Therefore, MRWT are of interest due to two particular benefits: their shorter blades and their faster wake recovery.

Regarding the blade size, the current generation wind turbines are up-scaled into multi megawatt range in terms of output power. However, the energy benefit from the turbine is offset by the increased mass and cost. 18 MW wind turbines are now feasible with rotor diameters up to 260 m, according to [Loz, 2023]. The question is, how much bigger can wind turbines get realistically? One concept worth considering, and the one that is the subject of this thesis, is to have more than one rotor on a single support structure. Such turbines could offer the advantage of standardization, mass production, transportation and ease of installation.

Regarding the faster wake recovery benefit, multi-rotor-turbines have shown to generate higher turbulence intensity in the near wake, which triggers a faster recovery of the wake [van der Laan et al., 2019], thus allowing for the turbine downstream to operate under a higher wind speed, thereby limiting wake losses. Hence, the multi-rotor concept allows for higher energy efficiency and wind farms where turbines are closer together, consequently increasing the energy density of the wind farm.

Even though the multi-rotor wind turbine concept has existed for a long time there is an absence of multi-rotor analytical models. Therefore, it is necessary to count with an accurate analytical model to allow a fast AEP calculation and multi-rotor wind-farm optimization; this being the first and main objective of the present work:

Conceive an engineering model to represent the wake of a two-rotors wind turbine.

A two-rotors wind turbine is defined as having one tower and two nacelles at the same hub-height, they are also referred as MR2 turbines. Then, the industrial partner, Vestas® , suggested a second research question which complements the study of [van der Laan and Abkar, 2019], formulated as:

What is the power output difference between a wind farm with N MR2 turbines and a wind farm with $2N$ *single rotor turbines if the total wind farm area and the rotor-type were to be kept equal?*

In order to tackle both objectives, the thesis is structured as follows: the present chapter introduces key concepts and the literature review of existing engineering wake models, chapter 2 explains the CFD setup, governing equations and used meshes. Then, chapter 3 conceives a surrogate model based on approximating the hub height wake profile of a single MR2 turbine with chosen base functions and storing their coefficients in look-up tables. Thereafter, chapter 4 obtains a method to merge the single MR2 wakes obtained previously. Afterwards, chapter 5 tests the developed surrogate model in a wind-farm scenario and compares it to engineering models that are currently used within the industry. Then, chapter 6 investigates a particular case of the second research question, since it compares the power output of a wind farm with 18 single rotor turbines with a layout of nine MR2 turbines. Finally, the whole thesis is concluded in chapter 7.

1.1. Global and local coordinate systems

Two Cartesian coordinate systems are used along the present report, a global coordinate system (x, y, z) which is located at the centroid of the simulated wind farm and a local coordinate system $(\hat{x}, \hat{y}, \hat{z})$. Both $z = 0$ and $\hat{z} = 0$ planes are coincident with the top of the aerodynamic roughness height z_0, which is defined as the height with null mean velocity as seen in Figure 1.2.

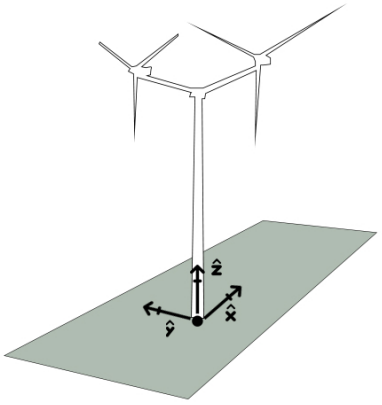

(a) Local coordinate system.

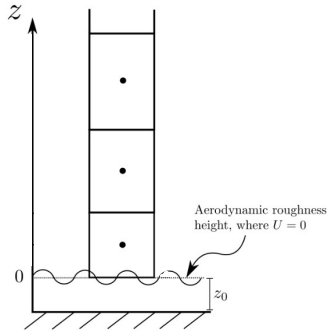

(b) Global z component which is equivalent to the local $\hat{z}$ component. Courtesy of Mads Baungaard.

Figure 1.2: coordinate system description

1.2. Self-similarity

Since the main objective of the present project is to develop an engineering model, some analytical models will be presented along the way and thus it is necessary to understand the concept of self-similarity.

A flow quantity, Φ, is self similar if the shape is the same in any scale [Pope, 2000]. Considering a turbine operating at a constant thrust coefficient C_T and subjected to a turbulent flow with constant ambient turbulence intensity at hub height at hub height, I_∞. Some existing analytical wake models define the velocity deficit as a function of the downstream distance from the turbine $\hat{x}$ and the radial distance from the turbine's horizontal axis $\hat{r}$ as:

$$\Phi(\hat{x},\hat{r}) = \frac{U_\infty - U_w(\hat{x},\hat{r})}{U_\infty} = \frac{\Delta U}{U_\infty}, \tag{1.1}$$

where U_∞ is the inflow velocity and U_w is the wake velocity at a given $(\hat{x},\hat{r})$ distance from the turbine. Defining the scaled variable:

$$\xi = \frac{\hat{r}}{\sigma(\hat{x})}, \tag{1.2}$$

where σ is the characteristic wake width which is a function of the downstream distance from the turbine $(\hat{x})$. Then, the velocity deficit $\Phi(\hat{x},\hat{r})$ is self-similar if it can be expressed as the multiplication of two independent functions, $\mathscr{F}_1$ and $\mathscr{F}_2$, that depend on $\hat{x}$ and ξ respectively, as:

$$\Phi(\hat{x},\xi) = \mathscr{F}_1(\hat{x}) \times \mathscr{F}_2(\xi). \tag{1.3}$$

Therefore, if we sample the wake at any given downstream distance, the wake will conserve its shape.

1.3. State of the art

In this section, the state of knowledge in the domain of wake velocity deficit, turbulent intensity and wake superposition will be established by revising the existing literature. This will be the starting point to build up the methodology that will lead to the aim of the present work, to characterize the wake of a double rotor wind turbine (MR2).

The chapter is structured as follows, subsection 1.3.1 introduces the atmospheric boundary layer, subsection 1.3.2 presents the existing engineering or analytical wake models for the velocity deficit of an horizontal axis wind turbine and subsection 1.3.4 presents the analytical models for the added turbulence.

1.3.1. Atmospheric Boundary Layer structure

The atmospheric boundary layer (ABL) is our main wind resource located in the lower region of the troposphere. The physics of the ABL is influenced by: geostrophic winds, aerodynamic roughness height z_0, Coriolis effects and thermal conditions.

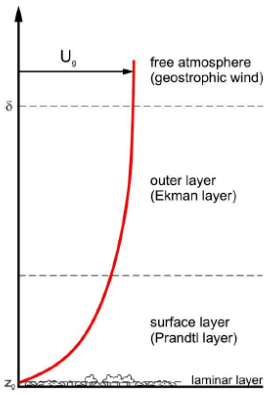

Figure 1.3: wind speed distribution and regions of the ABL [Satyam and Bin-Khalid, 2019].

As seen in Figure 1.3, the ABL is divided in three zones defined by [Kaimal and Finnigan, 1994] as:

- **The laminar layer**: is the region directly in contact with the earth which is defined by the roughness height z_0 and highly dominated by viscous effects. Assuming a constant shear stress τ equal

to the wall shear stress $\tau_w = \sqrt{u_\tau/\rho}$, where u_τ is the viscous velocity, by dimensional analysis we get:

$$z^+ = u^+, \tag{1.4}$$

where $z^+ = z u_\tau/\nu$, $u^+ = u/u_\tau$, u is the mean velocity of the first vertical cell element which center's distance to the wall is z [Pope, 2000], ν is the kinematic viscosity and u_τ is the friction velocity defined as: $u_\tau = \rho\tau_w^2$. Thus, within this viscous sub-layer (laminar layer) the velocity varies linearly with the distance from the wall. This relationship agrees with the experiments for $z^+ < 5$ [Sumer and Fuhrman, 2020]. Therefore, the height of the laminar layer δ_l is defined as

$$\delta_l = 5\frac{\nu}{u_\tau}, \tag{1.5}$$

which is much smaller than the aerodynamic roughness length z_0.

- **The surface layer**: which typically accounts for 10% of the ABL where the log-wind profile is valid. The latter can be derived through dimensional analysis assuming that the shear stress is still constant $\tau \approx \tau_w$, and neglecting viscous and thermal effects, thus obtaining

$$u^+ = \frac{1}{\kappa}\ln\left(\frac{z+z_0}{z_0}\right), \tag{1.6}$$

where κ is the Von Kármán constant [Pope, 2000].

- **The Ekman layer**: is the top zone of the ABL, which is mainly driven by the geostrophic winds that are governed by pressure gradients and Coriolis forces.

Furthermore, the thermal stability will affect the velocity and turbulence of the ABL. There are three different cases of thermal stability: stable, neutral and unstable. The thermal conditions may vary as a function of the daytime, cloud condition and sun albedo. In a stable atmosphere the vertical variation of temperatures tend to reduce the turbulence, while in an unstable condition the turbulence is increased. For a neutral condition the temperature has no effect on the turbulence. These aspects of the thermal stability are characterized by the potential temperature θ which is defined as:

$$\theta = T + \frac{gz}{C_p}, \tag{1.7}$$

where T is the air temperature, g the acceleration due to gravity, z the height and C_p the specific heat of the air under constant pressure. Thus, the thermal effects are defined as:

- Stable if $\frac{\partial\theta}{\partial z} > 0$
- Neutral if $\frac{\partial\theta}{\partial z} = 0$
- Unstable if $\frac{\partial\theta}{\partial z} < 0$

Within the scope of this work, a neutral atmospheric condition will be considered in order to focus on the wind shear generated turbulence.

Wind profile of a neutral atmospheric surface layer
The neutral atmospheric surface layer (ASL) hypothesis defines a logarithmic wind profile [Kaimal and Finnigan, 1994] described for our selected coordinate system[1] as:

$$U(z) = \frac{u_\tau}{\kappa}\ln\left(\frac{z+z_0}{z_0}\right), \tag{1.8}$$

where z_0 is the roughness height, $\kappa = 0.4$ is the Von Karman constant.

1.3.2. Analytical models of the wake velocity deficit

Several analytical wake models have been used to predict the velocity deficit within wind farms due to their simplicity and low computational cost. Starting from inviscid models that employ the 1D axial momentum theory and vortex cylinder models to derive the Betz limit and so estimate the wake deficit [Hansen, 2008]. Then, the load distribution on the rotor and velocity deficit was refined by applying blade element momentum (BEM) theory and vortex systems models [Glauert, 1935, Branlard and Gaunaa, 2015].

[1] If z=0 were taken at the ground level instead of the top of the roughness height z_0, then the log-profile would be $U(z) = \frac{u_\tau}{\kappa}\ln\left(\frac{z}{z_0}\right)$.

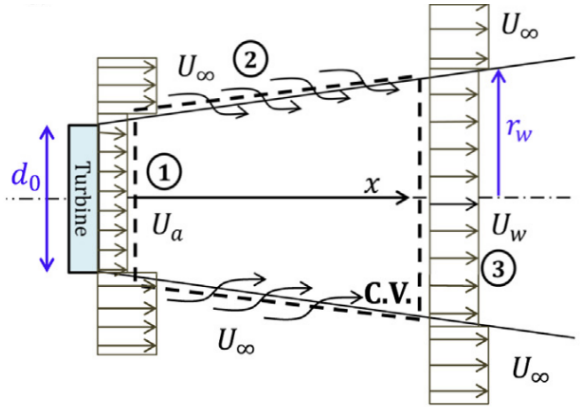

Figure 1.4: Schematic of the Jensen velocity deficit model. Image from [Bastankhah and Porté-Agel, 2014].

Top-hat model

Figure 1.4 shows one of the pioneering analytical model, the Jensen top-hat profile proposed by [Jensen, 1983], which is only based on the conservation of mass and assumes a uniform velocity deficit of the wake:

$$\frac{\Delta U}{U_\infty} = \frac{U_\infty - U_w}{U_\infty} = \frac{1-\sqrt{1-C_T}}{\left(1+\frac{2k_{\text{wake}}x}{D_0}\right)^2}, \tag{1.9}$$

where U_∞ is the freestream velocity, U_w the wake velocity, C_T the thrust coefficient, k_{wake} is a constant called the rate of wake expansion, D_0 the rotor diameter and x is the downwind distance from the turbine.

A top-hat model derived from both the mass and momentum conservation equations is then proposed by [Frandsen et al., 2006], where the normalized velocity deficit is expressed as:

$$\frac{\Delta U}{U_\infty} = \frac{1}{2}\left(1-\sqrt{1-2\frac{A_0}{A_{\text{w}}}C_{\text{T}}}\right), \tag{1.10}$$

where A_0 is the rotor area (located at $x=0$) and $A_w(x)$ is the wake area. Jensen assumed $A_0 = A_w(x=0)$, however Frandsen assumes $A_w(x=0) = \beta A_0$ where β is a function of C_T as

$$\beta = \frac{1}{2}\frac{1+\sqrt{1-C_T}}{\sqrt{1-C_T}}. \tag{1.11}$$

Gaussian model

Since many experiments and research studies observed a self similar Gaussian like behaviour of the velocity deficit of the wake of a turbine [Chamorro and Porté-Agel, 2009], an axis-symmetric Gaussian far-wake model was proposed by [Bastankhah and Porté-Agel, 2014], where the velocity deficit is defined as:

$$\frac{\Delta U}{U_\infty} = C_G(\hat{x}/D_0) \times \exp\left(-\frac{1}{2}\left(\frac{\hat{r}/D_0}{\sigma_G}\right)^2\right), \tag{1.12}$$

where $\hat{x}$ is the axial distance from the turbine, σ_G is the characteristic wake width (standard deviation of the Gaussian) and $\hat{r}$ is the radial distance from the rotor's horizontal axis.

As seen, the Gaussian model express the velocity deficit as the product of the maximum velocity deficit $C_G(\hat{x}/D_0)$ and a shape function that depends on $\hat{r}/(D_0\sigma_G)$ thus being self-similar.

Expressing Equation 1.12 in Cartesian coordinates and replacing C_G and σ_G by the functions derived in [Bastankhah and Porté-Agel, 2014], we get

$$\frac{\Delta U}{U_\infty} = \left(1-\sqrt{1-\frac{C_{\text{T}}}{8\left(k^*\frac{\hat{x}}{D_0}+\varepsilon\right)^2}}\right) \times \exp\left[-\frac{1}{2}\frac{\left(\frac{\hat{y}}{D_0}\right)^2+\left(\frac{\hat{z}}{D_0}\right)^2)}{\left(k^*\frac{\hat{x}}{D_0}+\varepsilon\right)^2}\right], \tag{1.13}$$

where $\hat{x},\hat{y},\hat{z}$ are the streamwise, lateral and vertical coordinates based on the local coordinate system of the turbine respectively. The wake growth is defined by $\sigma = k^*\hat{x}/D_0 + \varepsilon$, where $\varepsilon = 0.25\sqrt{\beta}$ and k^* is the wake growth rate which is linearly proportional to the turbulence intensity I.

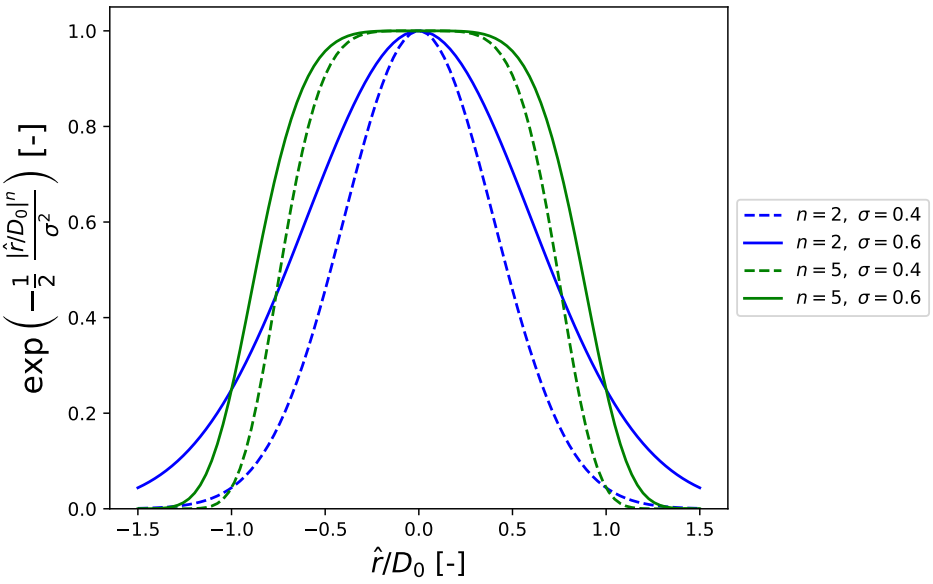

Figure 1.5: Gaussian profile ($n = 2$, blue color) and super-Gaussian ($n = 5$, green color) profiles for two wake width σ values.

Super-Gaussian model

So far, no analytical wake model has been exclusively developed for multi-rotor wind turbines, but some models meant for single rotor turbines might be able to represent multi-rotor wakes as well. Since multi-rotor wakes tend to a top-hat shape in the near wake, we will then introduce the super-Gaussian wake model.

Figure 1.5 shows high order Gaussian functions that resembles to a top-hat in the center of the wake but decays as a Gaussian in its extremes. The high-order Gaussian model proposed by [Blondel and Cathelain, 2020] describes the velocity deficit as:

$$\frac{\Delta U}{U_\infty} = C_{SG}\left(\frac{\hat{x}}{D_0}\right) \times \exp\left[-\frac{1}{2}\frac{(\hat{r}/D_0)^n}{\sigma_{SG}^2}\right], \tag{1.14}$$

where C_{SG} is the maximum velocity deficit, σ_{SG} is the wake width and n is the Gaussian order. It is expected for n to smoothly converge to the Gaussian profile in the far wake. This event, when the wake profile converge to a self-similar Gaussian, symbolises the transition to the far wake.

1.3.3. Velocity deficit superposition models

This section presents four wake superposition models since most commonly wind turbines are part of a whole wind farms and thus interact with neighbouring wakes.

Analogous to the point source pollutant dispersion, the following linear superposition method presented by [Lissaman, 1979] is proposed:

$$\frac{U_\infty - U_i}{U_\infty} = \sum_k^N \frac{U_\infty - U_{k,i}}{U_\infty}, \tag{1.15}$$

where N is the total number of wind turbines, $U_\infty(z)$ is the freestream velocity, U_i is the velocity at the turbine i and $U_{k,i}$ is the velocity deficit of turbine k at the location of the turbine i. Later, a superposition of energy deficit is proposed by [Katic et al., 1986] as

$$\frac{U_\infty - U_i}{U_\infty} = \frac{\sqrt{\sum_k^N (U_\infty - U_{k,i})^2}}{U_\infty}. \tag{1.16}$$

By doing so, Katic expect to *"conserve the mean kinetic energy deficit"* which is a debatable argument due to the turbulent dissipation of mean kinetic energy.

Since the two superposition methods presented so far are referenced to U_∞, the accumulation of many wakes can lead to nonphysical negative velocities. Thus [Voutsinas et al., 1990] proposed the following linear superposition model

$$\frac{U_\infty - U_i}{U_\infty} = \sum_k^N \frac{U_k - U_{k,i}}{U_\infty}, \tag{1.17}$$

where U_k is the velocity immediately upstream the turbine. Analogously, [Niayifar and Porté-Agel, 2016] proposed the following quadratic superposition

$$\frac{U_\infty - U_i}{U_\infty} = \frac{\sqrt{\sum_k^N (U_k - U_{k,i})^2}}{U_\infty}, \tag{1.18}$$

where they also make use of the local velocity U_k at the turbine k.

1.3.4. Analytical models of the wake added turbulence

Most wake deficit models presented make use of the wake width σ which depends itself on the turbulence intensity I. Thus, it is indispensable to also model the added turbulence intensity in order to model the wake velocity deficit.

The added turbulence intensity I^+ is calculated as proposed in [Crespo and Hernandez, 1996]

$$I^+ = \sqrt{I^2 - I_\infty^2}, \tag{1.19}$$

where I_∞ is the ambient turbulence intensity which depends on the vertical distance z due to the atmospheric boundary layer profile (ABL), and I is the turbulence intensity in the wake of the studied turbine. Since an Eddy viscosity model is employed to approximate the Reynolds stress tensor, the turbulence is assumed to be isotropic and thus the wake turbulence intensity, I, is computed as

$$I = \frac{\sqrt{\frac{1}{3}\left(\overline{u'u'} + \overline{v'v'} + \overline{w'w'}\right)}}{U_\infty}, \tag{1.20}$$

where the primed variables refer to the oscillating velocity component of Reynolds' decomposition. Replacing the Reynolds stress components with the turbulent kinetic energy, $k = 0.5\overline{u_i' u_i'}$, in Equation 1.20 we get

$$I = \frac{\sqrt{\frac{2}{3}k}}{U_\infty}, \tag{1.21}$$

where $U_\infty(z)$ is the mean inflow velocity. The present thesis will refer to the turbulence intensity I as the total turbulence intensity of Equation 1.21.

Analogous to the velocity deficit, the added turbulence model proposed by [Crespo and Hernandez, 1996] adopts a top-hat shape and follows this proportionality

$$I^+ \propto \frac{1}{\hat{x}^{C_1}}, \tag{1.22}$$

where $C_1 > 0$ is a model constant.

A similar top-hat model proposed by [Frandsen, 2007] follows the function

$$I^+ = \left(C_2 + C_3 \frac{\hat{x}}{\sqrt{C_T}}\right)^{-1}, \tag{1.23}$$

where C_2 and C_3 are model constants.

A self-similar double Gaussian profile proposed by [Ishihara and Qian, 2018] defines the turbulence intensity I^+ on the horizontal plane $z = z_{\text{hub}}$ as

$$\begin{aligned} I^+ = & \frac{1}{C_4(C_T) + C_5(I_0)\,\hat{x} + C_6(C_T, I_0)\,(1 + \hat{x}/D_0)^{-2}} \times \\ & \left[k_1\left(\frac{\hat{r}}{D_0}\right)\exp\left(-\frac{1}{2}\frac{(\hat{y}/D_0 - 0.5)^2}{\sigma^2}\right) + k_2\left(\frac{\hat{r}}{D_0}\right)\exp\left(-\frac{1}{2}\frac{(\hat{y}/D_0 + 0.5)^2}{\sigma^2}\right)\right], \end{aligned} \tag{1.24}$$

where C_4, C_5 and C_6 are model variables that depend on C_T and I_∞, and k_1 and k_2 are variables dependent of the normalized radial position $\hat{r}/D_0$.

Overall, there is no agreement of the axial scaling of the added turbulent intensity $I^+ \propto \hat{x}^{-a}$, meaning that the three exposed models all make use of a different a exponent.

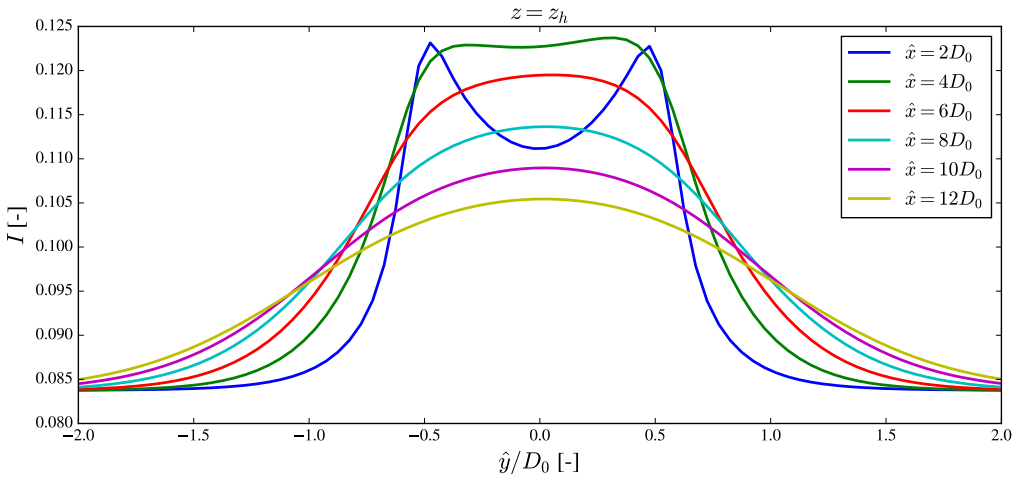

Figure 1.6: turbulence intensity I profile of a single rotor V29 turbine sampled at hub height ($z = z_h$). RANS simulation run with $U_\infty = 8$ m/s and $I_\infty = 8.4\%$ at hub height.

Figure 1.6 shows the wake turbulence intensity I of a single rotor V29 wind turbine sampled at hub height z_h. The profile in the near wake presents two peaks that then merge in the far wake which decays following a self-similar Gaussian profile as observed by [Kermani et al., 2013, Stein and Kaltenbach, 2019]. Therefore, the following double Gaussian function was proposed by [Lingkan and Buxton, 2023] to fit the turbulence intensity profile

$$I_w = C_1\left(\frac{\hat{x}}{D_0}\right) \times \exp\left[-\frac{1}{2}\frac{(\hat{y}/D_0 - y_{c1})^2}{\sigma_1^2}\right] + C_2\left(\frac{\hat{x}}{D_0}\right) \times \exp\left[-\frac{1}{2}\frac{(\hat{y}/D_0 - y_{c2})^2}{\sigma_2^2}\right], \tag{1.25}$$

where C_1, C_2, y_{c1}, y_{c2}, σ_1, σ_2 are model variables that depend on the downstream position $\hat{x}$.

1.3.5. Added turbulence intensity superposition methods

The superposition of turbulence intensity (or turbulent kinetic energy or wind speed standard deviation) has been less studied by the literature. Most of the reviewed papers employ a linear or square summation. Some other studies [Argyle et al., 2018, Niayifar and Porté-Agel, 2016] have shown positive results by only considering the turbulence intensity of the immediate upstream turbine wake, as:

$$I_i = \sqrt{I_\infty^2 + I_{+,i}^2}, \tag{1.26}$$

where the turbulence intensity of the wake of the i^{th} turbine, I_i, is computed from the ambient turbulence intensity I_∞ and the added turbulence intensity of the turbine itself $I_{+,i}$.

On the other hand, an empirically based I superposition method proposed by [Wessel et al., 2007] take into account all of the upstream turbines as:

$$I_i = I_\infty + \sqrt{\sum_i^N I_{+,i}^2}, \tag{1.27}$$

where N is the total amount of wind turbines.

A similar superposition method proposed by [Lingkan and Buxton, 2023] includes the ambient turbulent intensity within the square root as:

$$I_i = \sqrt{I_\infty^2 + \sum_i^N I_{+,i}^2}. \tag{1.28}$$

2
Simulation setup

The analytical model developed in this project is based on higher fidelity RANS-AD CFD models solved on EllipSys3D, a finite volume solver of the Technical University of Denmark (DTU) initially developed by [Michelsen, 1992, Michelsen, 1994, Sørensen, 1995] in FORTRAN, and configured through the python interface, PyWakeEllipSys (PWE).

As a summary of this chapter, RAND-AD CFD simulations are carried out on EllipSys3D over a flat terrain with homogeneous roughness length. The turbulence model employed is k-ε-f_P [van der Lann et al., 2015]. The inflow conditions correspond to an atmospheric surface layer of neutral stability.

First, the RANS governing equations are presented for a steady, incompressible and high Reynolds condition, together with the used turbulence model. Thereafter, the used boundary conditions are presented with the simulated wind turbines and the final part of this chapter is dedicated to the mesh parameters and its mesh-independence study.

2.1. Governing equations and turbulence model

Throughout this project we will assume constant density and viscosity of the air. Furthermore, since the simulated speeds are lower than Mach 0.3, we assume the flow to be incompressible. Thus, our governing equations consist of one equation for the conservation of mass and three for the conservation of momentum.

The mass equation can be re-written using Einstein notation as:

$$\frac{\partial u_i}{\partial x_i} = 0, \tag{2.1}$$

where u_i is the velocity vector and x_i is the Cartesian coordinates, both values are dimensionless and have been normalized with the characteristic velocity $\mathscr{U}$ and the characteristic length scale $\mathscr{L}$, respectively, i.e. $u_i = \tilde{u}_i/\mathscr{U}$ and $x_i = \tilde{x}_i/\mathscr{L}$, where the *tilde* denotes the dimensional flow variable.

In a similar way, the momentum equation can be written dimensionless as:

$$\frac{\mathscr{L}}{\mathscr{U}\mathscr{T}}\frac{\partial(u_i)}{\partial t} + \frac{\partial(u_i u_j)}{\partial x_j} = (f_v)_i - \frac{\partial p}{\partial x_i} + \frac{1}{\mathrm{Re}}\frac{\partial^2 u_i}{\partial x_j \partial x_j}, \tag{2.2}$$

where $\mathrm{Re} = \mathscr{L}\mathscr{U}/\nu$ is the Reynolds number, f_v is the dimensionless volumetric force $\left(f_v = \tilde{f}_v \mathscr{L}/\left(\rho\mathscr{U}^2\right)\right)$, p is the dimensionless static pressure $\left(p = \tilde{p}/\left(\rho\mathscr{U}^2\right)\right)$.

Assuming $\mathscr{U} = \mathscr{L}/\mathscr{T}$, where $\mathscr{T}$ is the characteristic time scale, and neglecting the Reynolds number (since it is based on the rotor diameter, $\mathscr{L} = D_0$, which tends to be large), Equation 2.2 can be reformulated as:

$$\frac{\partial(u_i)}{\partial t} + \frac{\partial(u_i u_j)}{\partial x_j} = (f_v)_i - \frac{\partial p}{\partial x_i}, \tag{2.3}$$

which is independent of the Reynolds number. In fact, the Reynolds number is based on the rotor diameter since the wind turbines are modelled by actuator disks and we are only interested in the larger scales. If the airflow over the turbine blades were to be resolved, then the chord length would probably be chosen as characteristic length. Therefore, if all the external forces scale with $\rho\mathscr{U}^2/\mathscr{L}$ and $\mathscr{U} = \mathscr{L}/\mathscr{T}$ then the Navier-Stokes momentum equations are independent of the characteristic scales of velocity $\mathscr{U}$ and length $\mathscr{L}$ [van der Laan et al., 2020].

The full derivation of the governing equations can be found in [Kundu et al., 2015] and the non-dimensionalization and scaling law used is further explained in [van der Laan et al., 2020].

2.1.1. RANS

Applying the Reynolds average decomposition where we define each time dependent variable ϕ as the sum of the averaged variable $\overline{\phi}$ and a fluctuating component ϕ':

$$\phi(x_i,t) = \overline{\phi}(x_i) + \phi'(x_i,t), \tag{2.4}$$

then, time averaging the previously defined governing equation and considering steady conditions, we get the following non-dimensional RANS equations:

$$\frac{\partial \overline{u}_i}{\partial x_i} = 0, \tag{2.5}$$

$$\overline{u}_j \frac{\partial \overline{u}_i}{\partial x_j} + \frac{\partial \overline{u'_i u'_j}}{\partial x_j} = \left(\overline{f_v}\right)_i - \frac{\partial \overline{p}}{\partial x_i}, \tag{2.6}$$

where $-\overline{u'_i u'_j}$ is the dimensionless Reynolds stress tensor, which will be modeled by the turbulence model.

2.1.2. Turbulence model k-ε-f_P

The k-ε-f_P model [van der Lann et al., 2015] is an eddy viscosity model introduced to overcome the poor modeling of velocity gradients areas (i.e. wind turbine wakes) by introducing the turbulence scale limiter f_P to the standard k-ε model, thus limiting the overshoot of turbulent viscosity ν_t in areas of high shear.

The Reynolds stress tensor $-\overline{u'_i u'_j}$ is modeled through the Boussinesq hypothesis as:

$$-\overline{u'_i u'_j} = \nu_t \left(\frac{\partial \overline{u}_i}{\partial x_j} + \frac{\partial \overline{u}_j}{\partial x_i}\right) - \frac{2}{3} k \delta_{ij}, \tag{2.7}$$

where $k = \frac{1}{2}\overline{u'_i u'_i}$ is the turbulent kinetic energy and ν_t is the turbulent viscosity which is modeled as:

$$\nu_t = C_\mu f_P \frac{k^2}{\varepsilon}, \tag{2.8}$$

where ε is the turbulent dissipation, $C_\mu = 0.03$ (for a neutral ASL) and f_P is defined as a function of the shear parameter σ:

$$f_P(\sigma/\tilde{\sigma}) = \frac{2 f_0}{1 + \sqrt{1 + 4 f_0 (f_0 - 1)\left(\frac{\sigma}{\tilde{\sigma}}\right)^2}}, \quad f_0 = \frac{C_R}{C_R - 1}, \tag{2.9}$$

where the shear parameter, σ, is defined as $\sigma \equiv \frac{k}{\varepsilon}\sqrt{\left(\frac{\partial \overline{u}_i}{\partial x_j}\right)^2}$, and $C_R = 4.5$ and $\tilde{\sigma} = 1/\sqrt{C_\mu}$ [van der Lann et al., 2015].

Moreover, the model adds the two following transport equations:

$$\frac{Dk}{Dt} = \frac{\partial}{\partial x_i}\left[\left(\nu + \frac{\nu_t}{\sigma_k}\right)\frac{\partial k}{\partial x_i}\right] + \mathscr{P} - \varepsilon, \qquad \frac{D\varepsilon}{Dt} = \frac{\partial}{\partial x_i}\left[\left(\nu + \frac{\nu_t}{\sigma_\varepsilon}\right)\frac{\partial \varepsilon}{\partial x_i}\right] + \left(C_{\varepsilon,1}\mathscr{P} - C_{\varepsilon,2}\varepsilon\right)\frac{\varepsilon}{k}, \tag{2.10}$$

where $\mathscr{P} = -\overline{u'_i u'_j}\frac{\partial \overline{u}_i}{\partial x_j}$ is the turbulent production term and $\sigma_k, \sigma_\varepsilon, C_{\varepsilon,1}$ and $C_{\varepsilon,2}$ are empirical constants defined in Table 2.1 calibrated to describe a neutral atmospheric boundary layer.

Table 2.1: model constants [van der Lann et al., 2015].

$C_{\varepsilon,1}$	$C_{\varepsilon,2}$	σ_k	σ_ε
1.21	1.92	1.00	1.30

2.2. Inflow model of an atmospheric surface layer

The inlet and top patches inflow profiles follow the analytical[1] neutral atmospheric surface layer (first 10% of the ABL) in equilibrium with the turbulence model meaning that the inflow profile is a solution of

[1] PWE also offers the option of first converging the vertical profile on a 1D precursor CFD simulation making use of the same vertical finite-volume discretization as in the 3D mesh, in order to account for the numerical error and start with a fully evolved vertical profile [van der Laan and Sørensen, 2017]. However, the present work directly uses the analytical log-law as inflow profile, thus causing a profile development at the beginning of the simulation.

the RANS equations. Thus, no thermal effects are taken into account and the velocity profile is dictated by the adiabatic log-law derived through dimensional analysis:

$$U = \frac{u_\tau}{\kappa} \ln\left(\frac{z+z_0}{z_0}\right), \tag{2.11}$$

where U is the mean stream-wise velocity, $\kappa = 0.4$ is the Von Kármán constant, z_0 the roughness length, z the height and u_τ is the friction velocity, defined as $u_\tau = \sqrt{\tau_w/\rho}$, where τ_w is the wall shear stress and ρ is the fluid density. Thereafter, the turbulent kinetic energy k and turbulent dissipation rate ε are derived from the governing equation ([Sumner and Masson, 2012] for full derivation):

$$k = \frac{u_\tau^2}{\sqrt{C_\mu}}, \tag{2.12}$$

$$\varepsilon = \frac{u_\tau^3}{\kappa(z+z_0)}, \tag{2.13}$$

where the eddy viscosity coefficient $C_\mu = 0.03$ is adapted for atmospheric applications by [Sørensen, 1995].

The roughness length, z_0, is then defined by the reference turbulence intensity, I_{ref}, measured at the reference height, z_{ref}, as follows:

$$I(z) = \frac{\sqrt{\frac{2}{3}k}}{U(z)} \xrightarrow{Equation\ 2.12} I(z) = \sqrt{\frac{2}{3}} \frac{u_\tau}{\sqrt[4]{C_\mu} U(z)} \xrightarrow{Equation\ 2.11} I(z) = \sqrt{\frac{2}{3}} \frac{1}{\sqrt[4]{C_\mu}} \frac{\cancel{U(z)}\kappa}{\ln\left(\frac{z+z_0}{z_0}\right)\cancel{U(z)}}, \tag{2.14}$$

$$I_{\text{ref}}(z_{\text{ref}}) = \sqrt{\frac{2}{3}} \frac{\kappa}{\sqrt[4]{C_\mu} \ln\left(\frac{z_{\text{ref}}+z_0}{z_0}\right)}, \tag{2.15}$$

$$z_0 = z_{\text{ref}} \left[\exp\left(\sqrt{\frac{2}{3}} \frac{\kappa}{\sqrt[4]{C_\mu} I_{\text{ref}}} \right) - 1 \right]^{-1}. \tag{2.16}$$

Hence, the inflow model only needs a reference height z_{ref} and a reference turbulence intensity I_{ref} in order to set z_0 [van der Laan et al., 2021].

2.3. Boundary conditions

The inlet and top patches have Dirichlet conditions for the velocity $\vec{U}$, turbulent kinetic energy, k, and the dissipation of turbulent kinetic energy, ε; and the outlet has a Neumann condition for the same variables. A periodic boundary condition is applied to the sides (north and south faces of the box-domain) and a rough-wall condition is assigned to the bottom wall with a uniform roughness length, z_0, which is defined by the inflow I_∞ at a given height.

In all cases the yaw is zero, meaning that the flow is aligned with the actuator disk normal vector.

Table 2.2: summary of the flat-box boundary conditions. ZG stands for zero gradient ($\nabla\phi = 0$).

	p [-]	U [-]	k [-]	ε [-]
Inlet (west face) and top face	ZG	$U_{in}(z)$	k_{in}	$\varepsilon_{in}(z)$
Outlet (east face)	0	ZG	ZG	ZG
North and South faces		periodic		
Bottom face	ZG	rough-wall	k_0	ε_0

Table 2.2 summarizes the applied boundary conditions on the six faces of the flat-box domain. Do note that Ellipsys3D models the flow from west (inlet) to east (outlet) and the whole wind farm rotates when different wind directions are studied. The inlet boundary condition (west face) and top face of the domain follow a logarithmic profile for a neutral atmospheric condition, which neglects Coriolis forces. Thus, the velocity is governed by

$$U_{in}(z) = \frac{u_\tau}{\kappa} \ln\left(\frac{z+z_0}{z_0}\right). \tag{2.17}$$

According to the velocity profile, the turbulent kinetic energy is specified as a constant value given by

$$k_{in} = \frac{u_\tau^2}{\sqrt{C_\mu}}, \tag{2.18}$$

while the dissipation of turbulent kinetic energy, ε, is given by

$$\varepsilon_{in} = \frac{u_\tau^3}{\kappa(z+z_0)}, \tag{2.19}$$

and replacing by Equation 2.18, we get

$$\varepsilon_{in} = \frac{C_\mu^{0.75} k^{1.5}}{\kappa(z+z_0)}, \tag{2.20}$$

thus, resulting in the following expression for the eddy viscosity

$$\nu_t = C_\mu f_P \frac{k^2}{\varepsilon} \xrightarrow[Equation\ 2.19]{Equation\ 2.18} \nu_t = f_P \kappa(z+z_0) u_\tau. \tag{2.21}$$

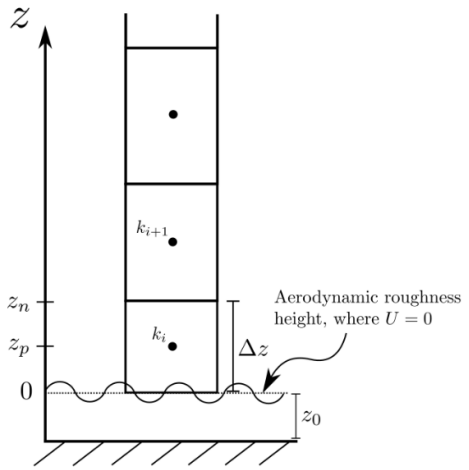

Figure 2.1: wall adjacent cells in accordance with Ellipsys reference system [Baungaard, 2019].

The velocity boundary condition is implemented through the wall skin friction, τ_w, as described in [Peric, 1985]:

$$\tau_w = \rho u_\tau^2 \xrightarrow{Equation\ 2.17} \tau_w = \rho u_\tau \left[\frac{U(z_p)\kappa}{\ln\left(\frac{z+z_0}{z_0}\right)}\right] \xrightarrow{Equation\ 2.18} \tau_w = \rho \left[\sqrt{k_{in}} \sqrt[4]{C_\mu}\right] \left[\frac{U(z_p)\kappa}{\ln\left(\frac{\Delta z+z_0}{z_0}\right)}\right], \tag{2.22}$$

where z_p is the vertical distance in between the first cell-center and the wall, and Δz is the height of the first cell as seen in Figure 2.1. Hence, knowing τ_w, the velocity at the first cell-center is imposed so as to comply

$$\tau_w = (\mu + \mu_t) \frac{\partial U}{\partial z}\bigg|_{z_n}, \tag{2.23}$$

where μ_t is the dynamic Eddy viscosity, and the gradient is computed at the top of the first cell adjacent to the wall, at height $z = z_n$ as per Figure 2.1.

Regarding the turbulent kinetic energy, k, as stated in [Sørensen et al., 2007], it is assumed that the production of k is in balance with the dissipation of it and that the shear stress in the first cell close to the wall is constant, thus $\tau_w = \mu \frac{\partial U}{\partial z} - \rho \overline{u'w'}$.

The boundary condition of ε at the wall complies with:

$$\varepsilon_1 = \frac{u_\tau^3}{\kappa(z_p+z_0)} \xrightarrow{u_\tau = \sqrt{k_{in}\sqrt{C_\mu}}} \varepsilon_1 = \frac{k_{in}^{1.5} C_\mu^{0.75}}{\kappa(z_p+z_0)}, \tag{2.24}$$

where the subscript 1 refers to the value at the first vertical cell and z_p is the distance from the wall to the center of the latter cell.

Regarding the wind turbines, each rotor is replaced by stiff permeable disks which input a pressure jump on the cells of the domain as a function of the averaged speed through the disk itself $\langle U \rangle_{AD}$.

2.4. Solver

The RANS equations are solved by EllipSys3D, which is a finite volume flow solver originally developed by [Sørensen, 1995, Michelsen, 1992] and still under continuous development by [DTU Wind and Energy Systems, 2023].

The QUICK scheme [Leonard, 1979] is employed to discretize the advection terms of the transport equations and the second-order-central-difference scheme is used for the diffusion term. The SIMPLE sequential solving algorithm [Patankar, 1980] is used to solve the three momentum equations, the equation for k and the transport equation fro ε, while also including the Poisson equation[2]. Moreover, in order to avoid a velocity-pressure decoupling, the Rhie-Chow algorithm is used in EllipSys3D [Réthoré and Sørensen, 2012].

In order to speed up the convergence of the numerical integration process, a grid-sequencing strategy is used [Michelsen, 1992]. Therefore, first a coarse grid (twice as coarse) simulation will be solved until all the residuals[3] fall below the defined threshold of 10^{-5} before mapping the solution to the finest grid and iterate until the residuals fall below the cutoff residual once again. The latter mesh-swap is thus responsible for the residual jump of Figure 2.2.

The CFD simulations of the present project are considered as converged when all the residuals of the finest mesh fall bellow 10^{-5}.

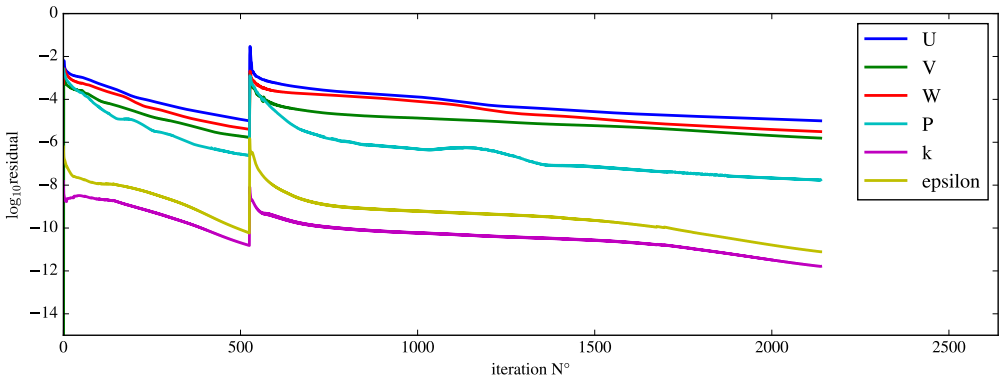

Figure 2.2: residual behaviour of the RANS CFD simulations with a two stages grid sequencing algorithm.

[2]The Poisson equation is obtained from applying the divergence operator on both sides of the momentum equation and replacing with the mass conservation equation ($\nabla \cdot U$).

[3]The local imbalance of a conserved variable is computed for each cell of the control volume and the residual in PyWakeEllipSys is then the L1-norm of all the cells' imbalance of the studied variable.

2.5. Wind turbines

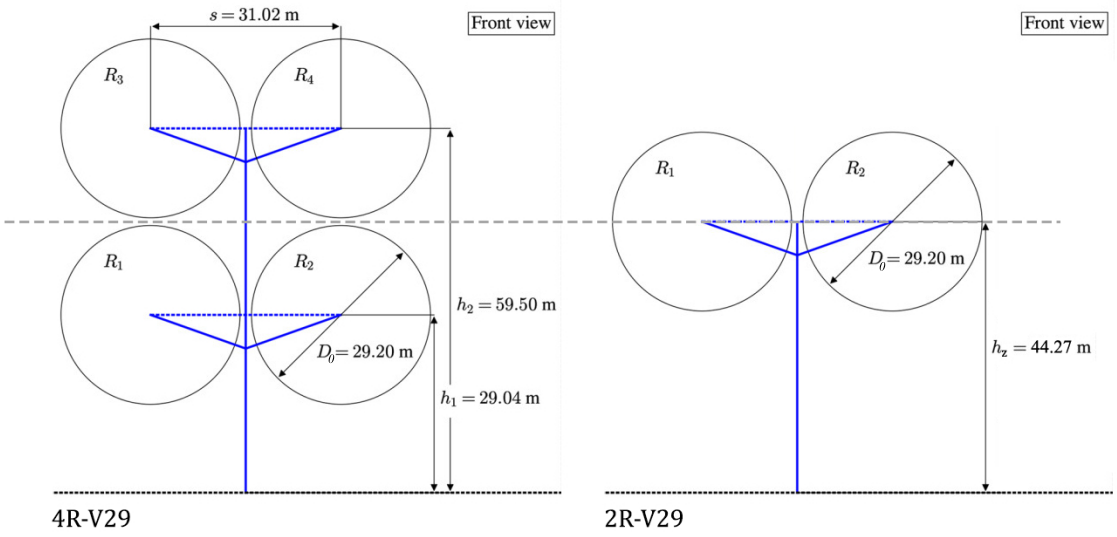

Figure 2.3: front view sketch of the 4R-V29 wind turbine taken from [van der Laan et al., 2019] and the illustrative 2R-V29.

The PyWakeEllipsys (PWE) workflow is tested and validated with the 4R-V29 turbine from Vestas® . The latter workflow validation can be found in Appendix A. Then, a fictitious wind turbine referred as the 2R-V29 is used as MR2 turbine to derive the wake model and compute the wind farm analysis and its comparison with single V29 turbines. The 2R-V29 turbine consist of two V29 rotors located on the same plane and at the hub height: z_h = 44.27 m. Both rotors are distanced a distance of 31.02 m (as in the 4R-V29 turbine).

Finally, a single rotor Vestas® V29 turbine with the same hub height (z_h = 44.27 m) as the 2R-V29 is employed in order to address the second research question of the present thesis which aims to study the power output difference in between a single-rotor wind farm and a multi-rotor-farm where the number of rotors and total farm-area are conserved.

Table 2.3: technical specification of the 4R-V29 turbine the fictitious 2R-V29 turbine and the V29 turbine used throughout the project.

Wind turbine	4R-V29	2R-V29	V29
Diameter D_0 [m]	29.2	29.2	29.2
Hub height z_h [m]	59.5 and 29.04	44.27	44.27
Horizontal distance between rotors axis [m]	31.02	31.02	-
Yaw angle [°]	0	0	0
Toe-out angle [°]	0	0	-
Maximum rotation speed [rpm]	41.3	41.3	41.3
Cut-in wind speed [m/s]	4	4	4
Cut-out wind speed [m/s]	25	25	25

2.6. Actuator disk

This project makes use of actuator disks to represent the wind turbines. Therefore, the rotor is replaced by a permeable stiff disk that introduces both the thrust and tangential forces generated by each wind turbine as a function of the local flow through the disk. In EllipSys-3D, the actuator disk method is based on the algorithm described in [Réthoré et al., 2014, Troldborg et al., 2015], where a discrete body force is represented as pressure jumps on the cell faces.

Based on the AD grid study carried by [Baungaard, 2019], the AD polar grid is discretized with

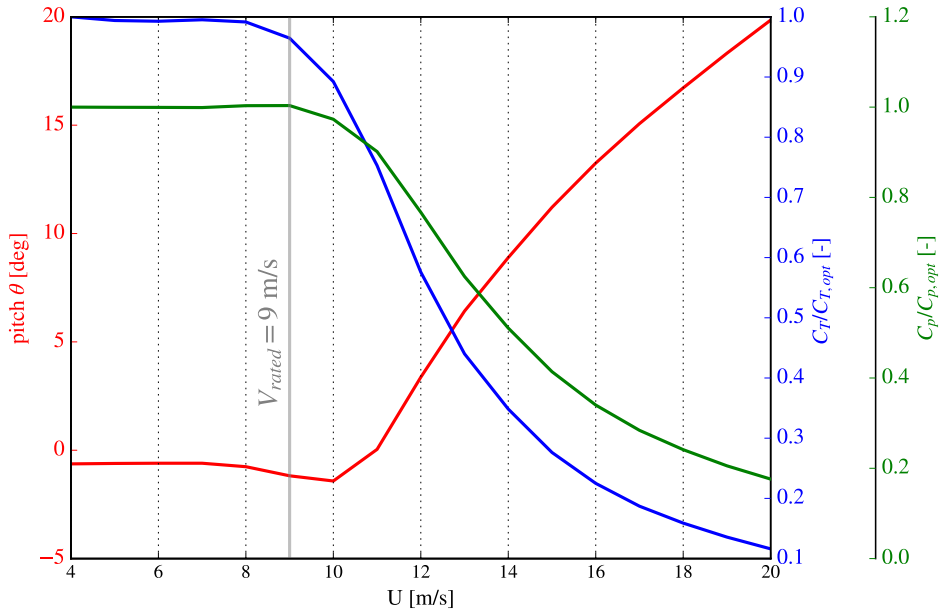

Figure 2.4: single rotor V29 turbine performances. The thrust and power coefficients have been normalized by their optimal values (obtained below rated wind speed) due to confidentiality reasons.

64 elements along the rotor radius ($N_R = 64$) and 64 elements along the azimuthal axis ($N_\theta = 64$) to distribute both the normal and tangential forces based on the local air velocity and the airfoil data of the turbine.

The applied method is described as *method III* in PWE, which takes as input the blade aerodynamic data: $C_T(U_\infty, r)$, $C_P(U_\infty, r)$ and the tip speed ratio $\lambda(U_\infty)$. Additionally, a calibration simulation is run beforehand in order to correctly model the forces of the turbines that are operating in the wake of upstream rotors. For example, when a turbine operates in the wake of another, then the freestream velocity variable, U_∞, of the shaded turbine is unknown. Therefore, after the calibration process the C_T coefficient is saved as a function of the average velocity through the actuator disk of the respective turbine, $\langle U_{AD} \rangle$, instead of U_∞. Hence, the following scaling is applied:

$$C_T^* = C_T \left(\frac{U_\infty}{\langle U_{AD} \rangle} \right)^2 = \frac{T}{\frac{1}{2}\rho A_0 U_\infty^2} \left(\frac{U_\infty}{\langle U_{AD} \rangle} \right)^2 = \frac{T}{\frac{1}{2}\rho A_0 U_{AD}^2}, \tag{2.25}$$

$$C_P^* = C_P \left(\frac{U_\infty}{\langle U_{AD} \rangle} \right)^3 = \frac{P}{\frac{1}{2}\rho A_0 U_\infty^3} \left(\frac{U_\infty}{\langle U_{AD} \rangle} \right)^3 = \frac{P}{\frac{1}{2}\rho A_0 U_{AD}^3}, \tag{2.26}$$

where T is the thrust, P is the power, ρ is the air density and A_0 is the actuator disk area (rotor area). The calibration simulation consist of one actuator disk which is run through all its wind speed, U_∞, range to then extract $\langle U_{AD} \rangle$ and compute C_T^* and C_P^*. Finally, C_T^*, C_P^* and rpm are available in a look up table as function of $\langle U_{AD} \rangle$ and will be accessed by PWE [DTU Wind and Energy Systems, 2023] during the simulations if the force control flag is activated.

2.7. Mesh

This thesis makes use of structured meshes with a flat terrain of constant roughness whose parameters are schematized in Figure 2.5. It can include up to two refinement boxes signaled in blue (wind turbine wake refinement box) and in magenta (wind farm scales refinement box). When different wind directions are simulated, the mesh is kept unchanged, the wind direction is always aligned with the x-axis, and the position of the actuator disks is rotated with respect to the wind farm centroid. Thus, the wind farm rotates with respect to its centroid which coincides with the origin of the mesh coordinate system.

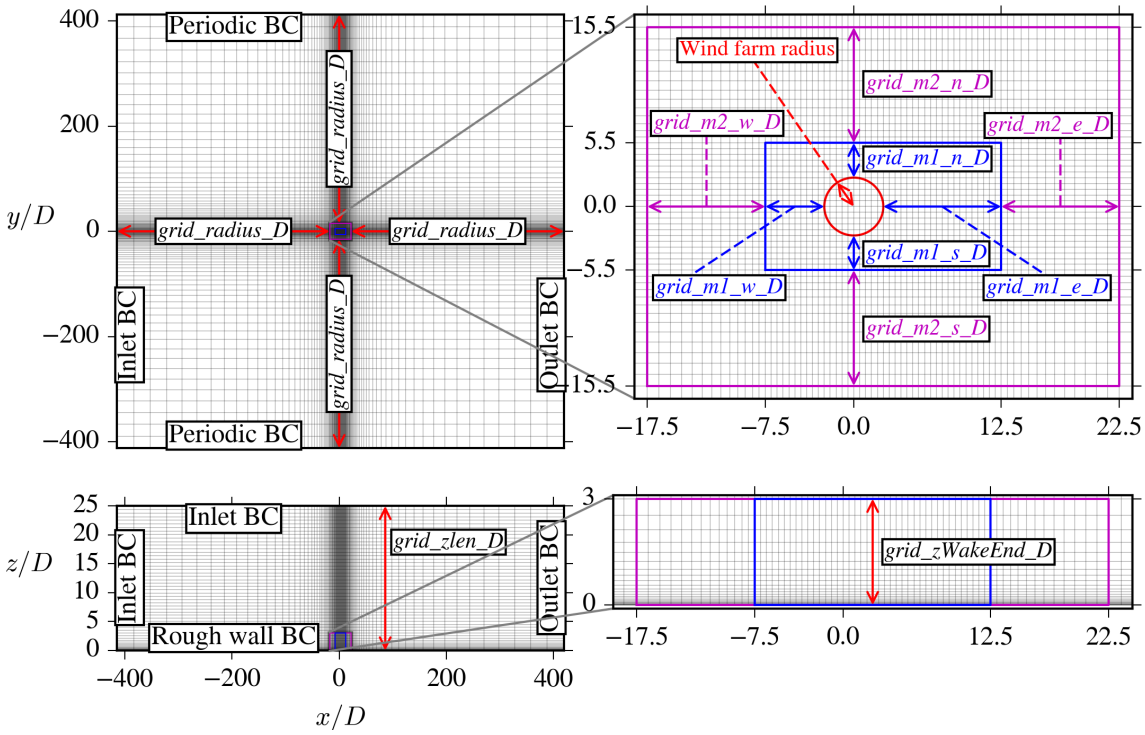

Figure 2.5: structured grid parameters [DTU Wind and Energy Systems, 2023].

Regarding the turbine wake refinement box, the inner-most refinement box, the grid spacing is denoted by Δ_1 and the upstream, downstream, side boundaries and height of the box are denoted by $m1_w$, $m1_e$, $m1_{n,s}$ and mz respectively. PWE also allows for a wind-farm wake refinement box, magenta refinement box of Figure 2.5, which will not be used in this project.

Regarding the higher resolution towards the rough-wall boundary condition of the bottom face, the first cell height (closest cell to the wall) is defined by z_1.

2.7.1. Mesh dependency study

A mesh dependency study is performed for an inflow conditions where the wake deficit is the largest, hence, at high C_T and low turbulence intensity, I_∞. The latter case is chosen in order to evaluate different mesh resolutions and select the coarsest mesh that gives an acceptable error. This is a key process in order to run cost efficient simulations whose results are mesh independent.

In order to evaluate the worst case scenario, the mesh independence study is run with a 2R-V29 turbine subjected to $U_\infty = 8$ m/s and $I_\infty = 5\%$ at $z = z_{\text{hub}}$. The used mesh and refined domain are specified in Table 2.5, except for the number of cells per diameter, $N_{CD} = D_0/\Delta_1$, used within the refinement box, which effect will be studied in the present section. The variable D_0 denotes the diameter of one of the rotors of the turbine i.e. $D_0 = 29.2$ m for both the single-rotor V29 turbine and the multi-rotor 2R-V29 turbine or 4R-V29.

Grids

The actuator disk (AD) forces are input from a 2D polar grid with a uniform azimuthal and radial discretization with N_θ elements along the azimuth and N_R elements along the radius of the rotor. Then, the polar grid forces are extrapolated to the Cartesian mesh where the rotor diameter is discretized with N_{CD} cells in each direction and the grid spacing in the refined domain is denoted as Δ_1, hence $N_{CD} = D_0/\Delta_1$.

Order analysis

Table 2.4: Actuator disk and mesh resolution used for the order analysis.

Grid level (n)	$N_{CD} = D_0/\Delta_1$	h_n
1	16	1
2	8	2
3	4	4

The same simulation is run on three different mesh resolutions (grid levels) to estimate the error decrease order when the mesh resolution is increased. Table 2.4 shows the evaluated mesh resolutions.

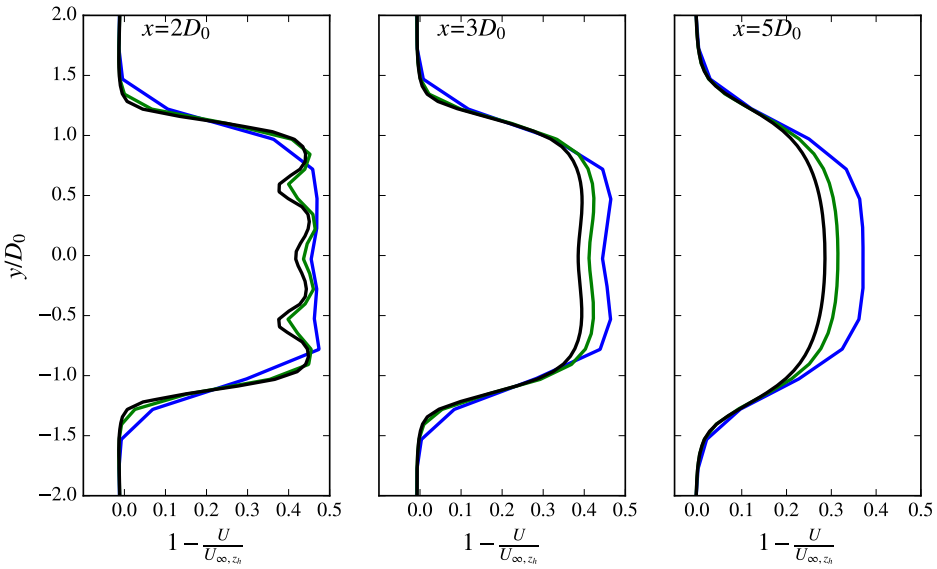

Figure 2.6: evaluation of different grid levels for a single 2R-V29 turbine located at x=0, subjected to $U_\infty = 8$ m/s and $I = 5\%$ at hub height.

Figure 2.6 shows the velocity deficit at hub height for the three different grid levels modelled. The disk averaged velocity deficit $\frac{1}{A_0}\int \frac{\Delta U}{U_\infty} dA$ is chosen as the basis for the order analysis, where A_0 is the rotor disk area. Thus, the discretization error ϵ_n is estimated by the following Taylor expansion:

$$\epsilon_n = \left[\frac{1}{A_0}\int \frac{\Delta U}{U_\infty} dA\right]_n - \left[\frac{1}{A_0}\int \frac{\Delta U}{U_\infty} dA\right]_{\text{exact}} = g_1 h_n + g_2 h_n^2 + g_3 h_n^3 + \mathcal{O}(h_n^4), \tag{2.27}$$

where n is the grid level. Figure 2.7 shows the multi-order analysis for the three evaluated grid levels and their respective error ϵ_n compared to the Richardson extrapolation [Richardson, 1911]. For $x > 5D_0$, the lower the grid level, the lower the error; thus showing a convergence toward the exact solution.

The third grid level (n=1) represents the peak velocity deficit shifted in the axial direction and also presents the highest error. This explains why in the very near wake, $2D_0 < x < 5D_0$ the coarser mesh seems to be the most accurate. With a $\epsilon_1 = 13\%$ at $x = 5.2D_0$, despite being the most computational expensive grid, the $n = 1$ grid is chosen to run the single MR2 turbine RANS-AD simulations since it presents an error $\epsilon_1 < 15$ % in the down-wind zone of interest ($2 < x/D_0 < 20$).

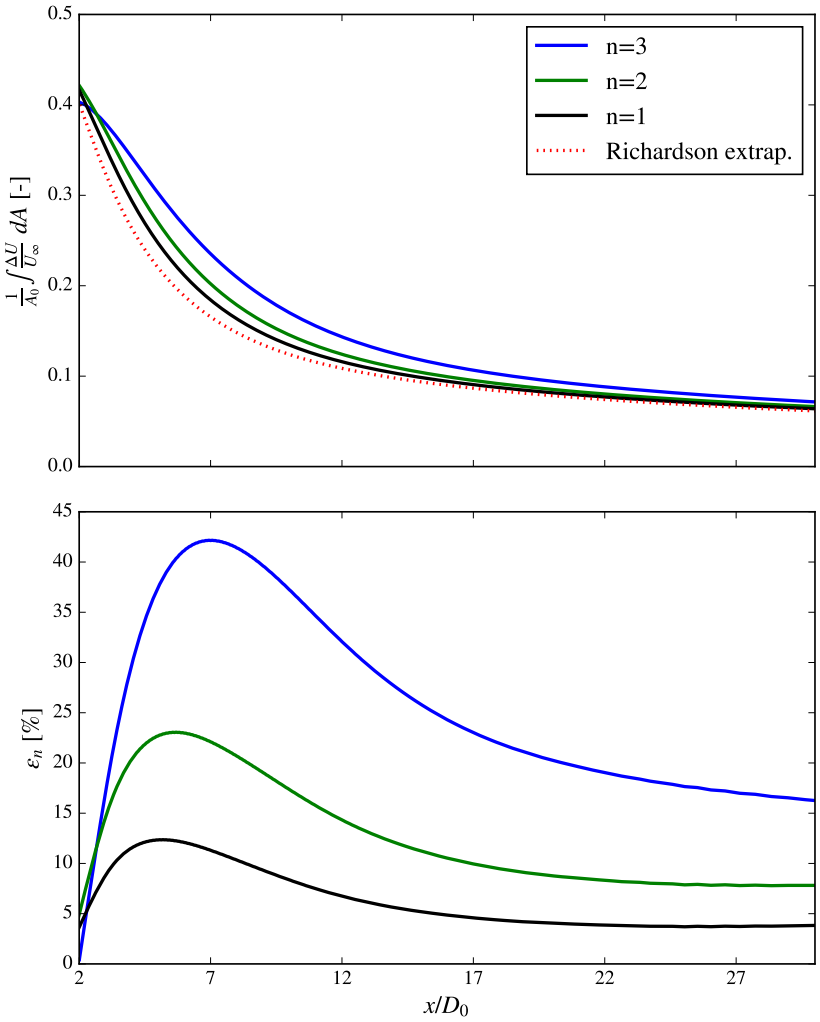

Figure 2.7: multi order analysis of three grid levels for a single 2R-V29 turbine located at x=0, subjected to $U_\infty = 8$ m/s and $I = 5\%$ at hub height.

2.7.2. Single multi-rotor turbine simulation

In the case of a single multi-rotor turbine being simulated, a refinement box is used to better capture the wake of the turbine since the axial velocity and turbulent kinetic energy fields will later be used to fit the base functions as part of the analytical surrogate model. Based on Figure 2.5, the mesh outer bounds and the refinement box dimensions are shown in Table 2.5, thus giving an outer domain of $110D_0 \times 110D_0 \times 50D_0$ (length × width × height) analogous to the domain used in [van der Laan et al., 2019]. The described domain results in a blockage ratio for a single 4R-V29 turbine of $\pi/(110 \times 50) = 0.057\%$ and a blockage ratio of $0.5\pi/(110 \times 50) = 0.028\%$ for a 2R-V29 turbine.

Table 2.5: Single turbine mesh geometrical parameters normalized by one rotor diameter D.

		PWE variable	Normalized variable
Outer domain		grid_radius_D	55
		grid_zlen_D	50
First cell height	z_1	grid_zFirstCell_D	0.5
Grid growth ratio		grid_r	1.2
AD polar resolution	N_θ	adgrid_ntheta	64
	N_R	adgrid_nr	64
Refinement box Wake domain	$N_{CD} = D_0/\Delta_1$	grid_cells1_D	16
	$m1_w$	grid_m1_w_D	3
	$m1_n$	grid_m1_n_D	5
	$m1_e$	grid_m1_e_D	20
	$m1_s$	grid_m1_s_D	5
Height of the wake refinement box		grid_zWakeEnd_D	3

2.7.3. Four inline turbines simulations

Regarding the simulation of four multi-rotor turbines in a row with a uniform turbine inter-spacing $S = [3,5,7,9]D_0$, the mesh outer bounds are expanded to $1000D_0 \times 1000D_0 \times 50D_0$ (length x width x height) analogous to the domain used in [van der Laan and Abkar, 2019]. The described domain results in a blockage ratio for an inline row of 2R-V29 turbines of $(\pi/2)/(1000 \times 50) = 3.1 \times 10^{-3}\%$.

Table 2.6: Four inline MR2 turbines mesh geometrical parameters normalized by one rotor diameter D_0.

		PWE variable	Normalized variable
Uniform turbine inter-spacing	S/D_0	-	[3, 5, 7, 9]
Outer domain		grid_radius_D	500
		grid_zlen_D	50
First cell height	z_1	grid_zFirstCell_D	0.5
Grid growth ratio		grid_r	1.2
AD polar resolution	N_θ	adgrid_ntheta	64
	N_R	adgrid_nr	64
Refinement box Wake domain	$N_{CD} = D_0/\Delta_1$	grid_cells1_D	16
	$m1_w$	grid_m1_w_D	$1.5 \times S + 2$
	$m1_n$	grid_m1_n_D	5
	$m1_e$	grid_m1_e_D	$1.5 \times S + 20$
	$m1_s$	grid_m1_s_D	5
Height of the wake refinement box		grid_zWakeEnd_D	3

2.7.4. Wind farm simulations

This section presents two types of wind-farm layout configuration, a 3×3×MR2 wind farm sketched in Figure 2.8a and a 18×SR wind farm layout of Figure 2.8b.

A 3×3 wind farm configuration of MR2 turbines of the type 2R-V29 spaced a distance S in between towers is subjected to different wind directions and wind speeds in order to test the analytical wake model under non-aligned and partly-overlapping wake conditions.

Then, 18 single rotor wind turbines (18×SR) of the type V29 are located within a square of equal area than the 3×3×MR2 wind farm of Figure 2.8a with a layout defined according to the packing theory of congruent non-overlapping circles [Lubachevsky and Graham, 2004].

This last set of 18×SR turbine simulations is studied to answer whether it's better to locate 18 rotors as single-rotor turbines or in a MR2 configuration.

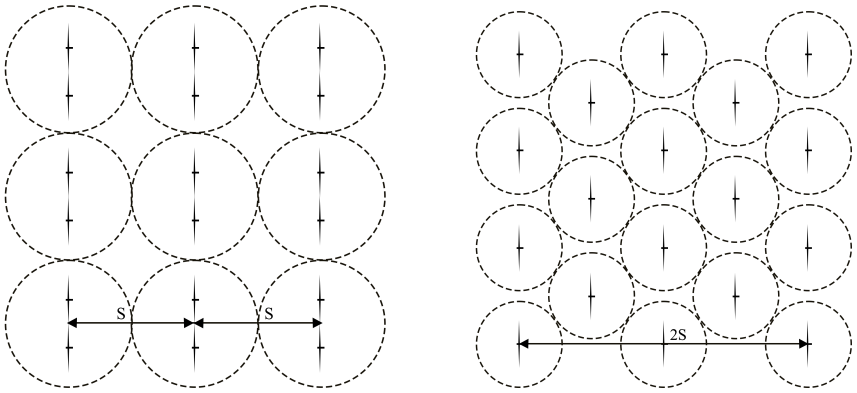

(a) 3×3×MR2 wind farm layout. **(b)** 18×SR wind farm layout.

Figure 2.8: Multi-rotor and single rotor layouts where the total wind farm area, $4S^2$, and the number of rotors is kept equal.

In order to reduce the CPU demand, the wind farm simulations have been run using 8 cells to discretize the rotor diameter, $N_{CD} = 8$, instead of 16. This will result in a maximum of 23% difference of the velocity deficit in comparison to the Richardson extrapolation as seen in subsection 2.7.1.

Table 2.7: wind farm mesh geometrical parameters normalized by one rotor diameter D_0.

		PWE variable	Normalized variable
Spatial scale parameter	S/D_0	-	[5, 7]
Outer domain		grid_radius_D grid_zlen_D	500 50
First cell height Grid growth ratio	z_1	grid_zFirstCell_D grid_r	0.5 1.2
AD polar resolution	N_θ N_R	adgrid_ntheta adgrid_nr	64 64
Refinement box Wake domain	$N_{CD} = D_0/\Delta_1$ $m1_w$ $m1_n$ $m1_e$ $m1_s$	grid_cells1_D grid_m1_w_D grid_m1_n_D grid_m1_e_D grid_m1_s_D	**8** $\sqrt{2} \times S + 5$ $\sqrt{2} \times S + 3$ $\sqrt{2} \times S + 20$ $\sqrt{2} \times S + 3$
Height of the wake refinement box		grid_zWakeEnd_D	3

3

2R-V29 wake and model fitting

This section studies the wake of a single MR2 turbine and fits the different proposed analytical base functions to the MR2 wakes obtained through RANS-AD simulations. First, a set of RANS-AD simulations of a single MR2 turbine are run for a range of ambient turbulence intensities, I_∞, and freestream speed, U_∞, to then map both a double-Gaussian profile and a high order Gaussian model (super-Gaussian) to the velocity deficit, $\Delta U/U_\infty$. Furthermore, the super-Gaussian base function is also used to map the added turbulence intensity, I^+, at the hub height plane, $z = z_h$.

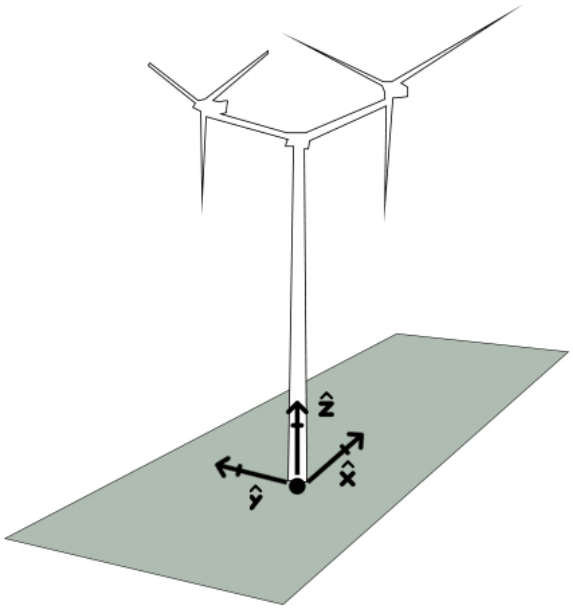

Figure 3.1: local coordinate system which origin is located at the base of the turbine of interest.

Throughout the present report, the origin of the main Cartesian coordinate system is located at the centroid of the studied wind farm, where x is always pointing in the direction of U_∞, and z is pointing upward. Figure 3.1 shows the local reference system which is characterised by $(\hat{x}, \hat{y}, \hat{z})$, and defines spacial coordinates with respect to the turbine of interest.

First a set of RANS simulations are run for a range of freestream wind speeds, U_∞, and turbulence intensities, I_∞, measured at the hub height, z_h. Then, for each simulation and axial position, $\hat{x}$, the velocity deficit profile, $\Delta U/U_\infty$, is fitted with both a high order Gaussian function and a double Gaussian base function. The added turbulence intensity, $I^+ = \sqrt{I^2 - I_\infty^2}$, on the other hand, is only mapped with the high order Gaussian base function, since it showed the best fit in comparison to the double-Gaussian shape and a tetra-Gaussian function. The latter being inspired from the research of [Lingkan and Buxton, 2023] who found that the turbulence intensity of a single-rotor wake adopts a double-Gaussian shape; ergo the author of the present thesis believed that two rotors, one next to the other, should generate a turbulence intensity shaped as a tetra-Gaussian function, but no positive results were found while trying to fit a function with few degrees of freedom (fitting coefficients). Consequently only the super-Gaussian function is presented and used to fit the added turbulence intensity profile of the 2R-V29 turbine.

Finally, the base function coefficients are stored in look-up tables (LUT) as a function of the wind conditions: U_∞, I_∞ and as a function of the local axial distance $\hat{x}$. Furthermore, the power produced by the MR2 turbine is also included in the LUT as a function of U_∞ and I_∞ so as to allow for wind farm optimizations. The LUT building instructions are summarized in algorithm 2 of section 4.1.

Reynolds-number similarity of the wind farm simulations can be used to reduce the number of iterations by running wind speed flow cases consecutively because only local changes needs to be recalculated after the first simulation has converged

3.1. RANS of a single MR2

A set of RANS-AD simulations are run with a combination of ambient turbulence intensities, I_∞ = [5, 10, 15, 20, 30]%, and wind speeds[1], U_∞ = [4, 5, 6, 7, 8, 10, 13, 16] m/s, at hub height for a single MR2 turbine (2R-V29) standing in the middle of the domain described in subsection 2.7.2. Due to the Reynolds number independence of the RANS equations explained in section 2.1, it is then not needed to model all wind speeds in PyWakeEllipSys, but only the ones with different C_T, C_P and tip-speed-ratio, λ [van der Laan et al., 2022]. Thus, resolving the time averaged velocity, (U,V,W), the averaged pressure, p, the dissipation of turbulent kinetic energy, ε, and the turbulent kinetic energy, $k = 0.5\overline{u_i' u_i'}$. The wake turbulence intensity, I, is computed as

$$I = \frac{\sqrt{\frac{2}{3}k}}{U_\infty}, \tag{3.1}$$

and the added turbulence intensity is calculated as

$$I^+ = \sqrt{I^2 - I_\infty^2}. \tag{3.2}$$

Furthermore, the velocity deficit is defined as:

$$\frac{\Delta U}{U_\infty} = \frac{U - U_\infty}{U_\infty}. \tag{3.3}$$

Since the analytical model is developed for the hub height plane ($z = z_h$), both the velocity field, U, and the turbulent kinetic energy, k, are sampled at hub height.

3.2. Analytical model fitting

From EllipSys3D, we resolve the wake of a single MR2 turbine for a range of U_∞ and I_∞. In this section each wake is sampled at hub height for each local axial position ranging from two diameters upstream the turbine until 50 diameters downstream[2] ($-2D_0 < \hat{x} < 50D_0$) and the selected base-functions are fitted to the wake. Then the function coefficients are saved in a look-up table as a function of the axial position, $\hat{x}$, U_∞ and I_∞.

From the list of models presented in subsection 1.3.2, the following two base functions have shown the best fit of the velocity deficit $\Delta U/U_\infty$ profile:

Super Gaussian

$$\frac{\Delta U}{U_\infty} = C_{SG} \times \exp\left(-\frac{1}{2}\frac{\hat{y}^{n_{SG}}}{\sigma_{SG}^2}\right), \tag{3.4}$$

Double Gaussian

$$\frac{\Delta U}{U_\infty} = C_{DG} \times \left(\exp\left(-\frac{1}{2}\frac{(\hat{y} - n_{DG}\ (\mathrm{arm}/D_0))^2}{\sigma_{DG}^2}\right) + \exp\left(-\frac{1}{2}\frac{(\hat{y} + n_{DG}\ (\mathrm{arm}/D_0))^2}{\sigma_{DG}^2}\right)\right), \tag{3.5}$$

where the arm/D_0 variable is the normalized distance from the MR2 centroid to the rotors' axis; and C_{SG}, σ_{SG}, n_{SG}, C_{DG}, σ_{DG} and n_{DG} are function coefficients that are fitted for each $\hat{x}$ position using the

[1] The latter wind speeds correspond to a turbine C_T = [0.818, 0.813, 0.812, 0.814, 0.811, 0.73, 0.36, 0.184].

[2] Do note that the refinement box extends up to $20D_0$ east of the wind turbine as defined in subsection 2.7.2. Hence, we expect a poorer resolution of the far-wake past this point.

Trust Region Reflective non-linear least squares algorithm [Branch et al., 1999] built in the python library *scipy.optimize.curve_fit*. The outcome of the latter fitting process is illustrated at three downstream positions in Figure 3.3. It is seen that both functions tend to a second order Gaussian in the far-wake.

The super-Gaussian base function is also used to fit the added turbulence intensity, I^+, which is illustrated at three downstream positions in Figure 3.4. As observed, the I^+ also tends to a second-order-Gaussian in the far-wake.

Therefore, the fitted model coefficient are stored in look-up tables as a function of the local axial position $\hat{x}$, and the freestream variables I_∞ and U_∞ seen by the turbine at hub height z_h.

3.3. Power relationship with U_∞ and I_∞

Since the power produced by a turbine is a quantity of interest used to optimize wind farm layouts, the power produced by the 2R-V29 turbine is saved in a look-up table as a function of the U_∞ and I_∞.

Figure 3.2 shows the variation of $\langle U \rangle_{AD}$ and power extracted from the RANS-AD simulation as a function of U_∞ and I_∞. We thus observe that for a given I_∞, there is a monotonic growth of the $\langle U \rangle_{AD}$ and power with U_∞. Figure 3.2b shows the normalized power produced by the 2R-V29 turbine for the range of U_∞ and I_∞ used to train the model. The fact that the power is more sensitive to variations of U_∞ than I_∞ will later be taken into account in section C.2 to opt for a better accuracy of the wake velocity model over the turbulence intensity model.

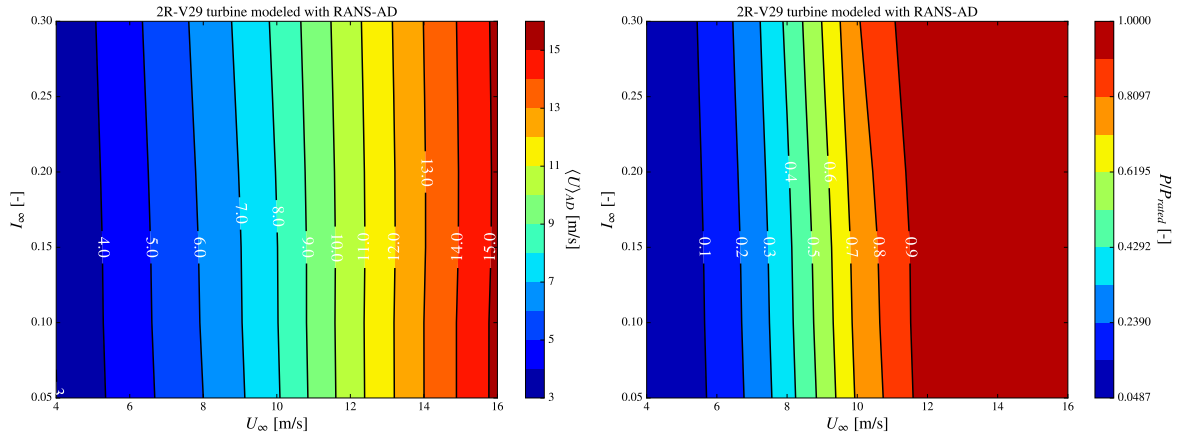

(a) $\langle U \rangle_{AD}$ **(b)** normalized aerodynamic power

Figure 3.2: sampled parameters of a single 2R-V29 turbine as a function of I_∞ and U_∞ at hub height.

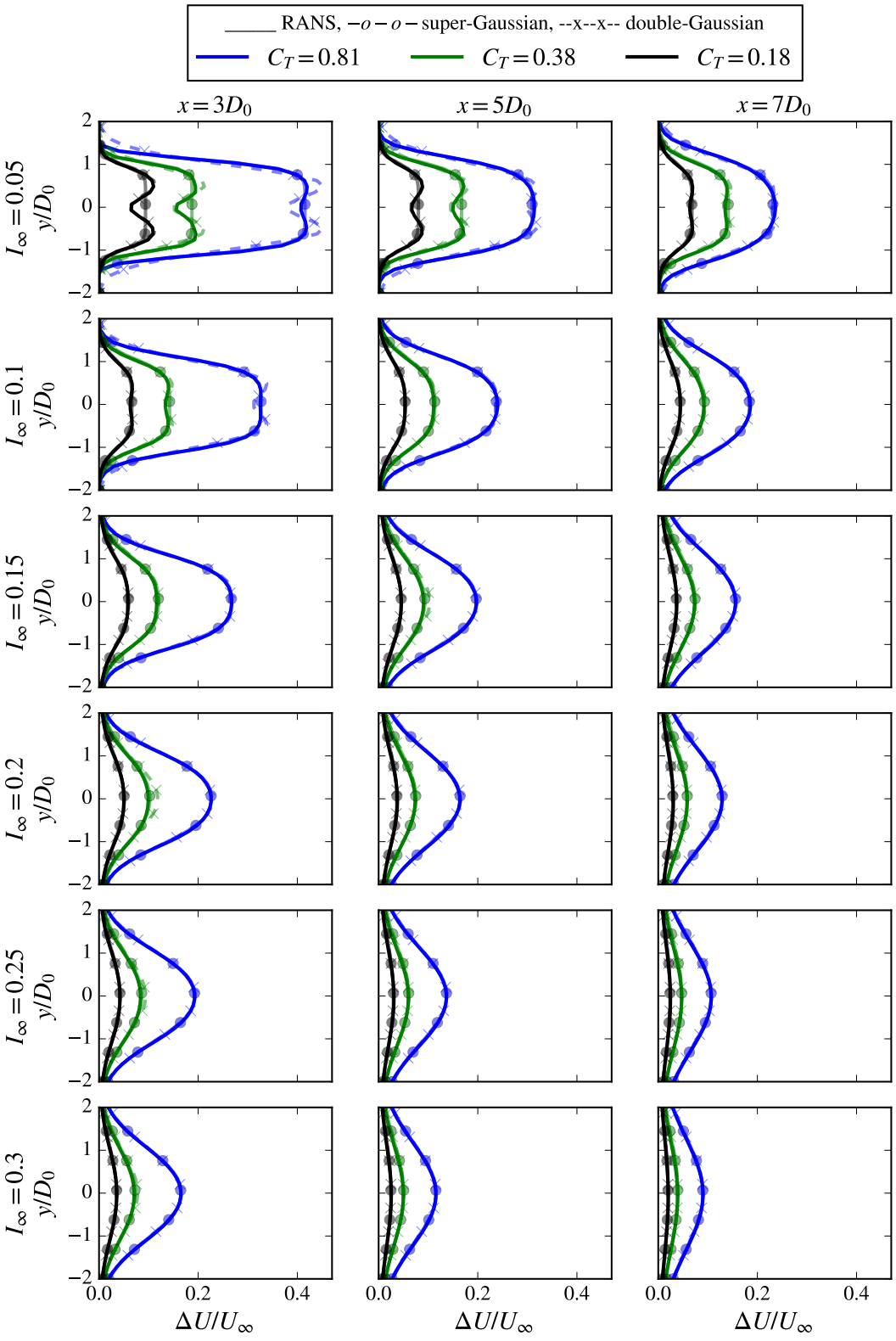

Figure 3.3: velocity deficit, $\Delta U/U_\infty$, of the 2R-V29 turbine sampled at three different downstream positions for the RANS simulation and both the fitted super-Gaussian and double-Gaussian models.

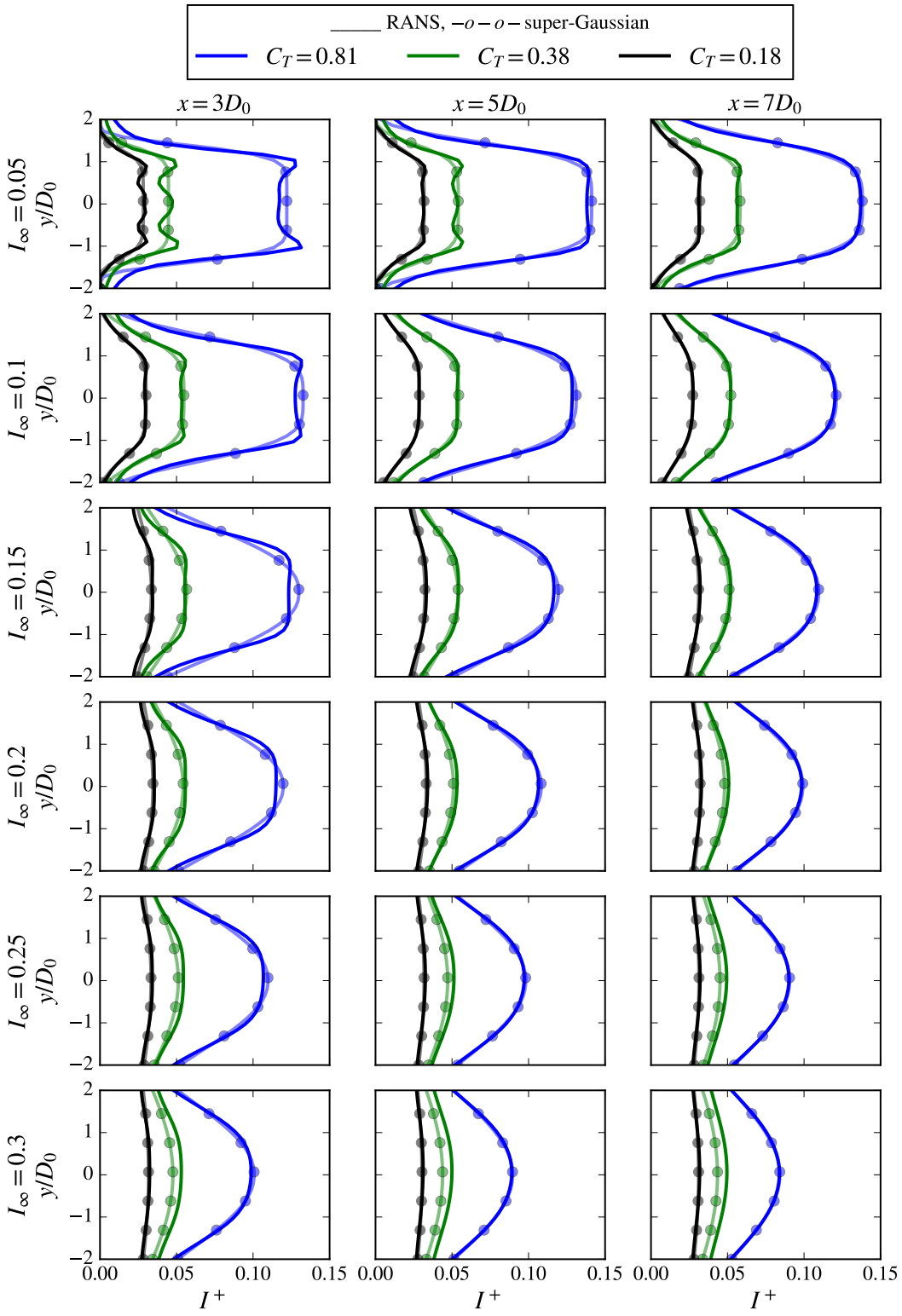

Figure 3.4: added turbulence intensity, $I^+ = \sqrt{I^2 - I_\infty^2}$, of the 2R-V29 turbine sampled at three different downstream positions for the RANS simulation and the fitted super-Gaussian model for I^+.

4

Wake superposition model

In chapter 3, the following three sets of function coefficients (C, σ and n) are stored in look-up tables $\Psi(U_\infty, I_\infty, \hat{x})$ as a function of the axial position $\hat{x}$ and the ambient conditions I_∞ and U_∞ at z_h:

- The super-Gaussian coefficients that fit the velocity deficit $\frac{\Delta U}{U_\infty}$ of a single 2R-V29 turbine wake.
- The double-Gaussian coefficients that fit the velocity deficit $\frac{\Delta U}{U_\infty}$ of a single 2R-V29 turbine wake.
- The super-Gaussian coefficients that fit the added turbulence intensity I^+ of a single 2R-V29 turbine wake.

Furthermore, the power output of the single 2R-V29 turbine is stored in an additional look-up table $\Psi(U_\infty, I_\infty)$ as a function of the I_∞ and U_∞ at z_h.

The present chapter derives a wake superposition model in order to represent the accumulated wake of four aligned 2R-V29 turbines.

4.1. Superposition method

Figure 4.1 sketches the superposition algorithm which following steps are run from the most upstream turbine, $i = 1$, gradually moving up to the most down-wind turbine, $i = N$:

1. Initialize $\Delta U/U_\infty$ and I^+ of the hub height plane, $z = z_h$, as zero.
2. Sample the velocity $U_{\infty,1}$ and turbulence intensity $I_{\infty,1}$ of the two segments[1] that result from intersecting the 2R-V29 turbine rotors with the hub height plane, and average i.e. $U_{\infty,1} = \langle U \rangle_{\text{AD},z_h,1}$ and $I_{\infty,1} = \langle I \rangle_{\text{AD},z_h,1}$. Both $U_{\infty,1}$ and $I_{\infty,1}$ then represent the freestream ambient wind conditions seen by the first turbine ($i = 1$) at hub height.
3. Access the look-up table (LUT) with both $U_{\infty,1}$ and $I_{\infty,1}$ to obtain the produced power, P_1, the velocity deficit, $\frac{\Delta U}{U_{\infty,1}}$, and the added turbulent intensity, I_1^+, of this first MR2 turbine. The teal colored variables represent variables extracted from the LUT.
4. Reconstruct the accumulated wake by linearly summing the velocity deficit as

$$\frac{\Delta U}{U_\infty} = \sum_{i=1}^{1} \frac{\Delta U}{U_{\infty,i}} \frac{U_{\infty,i}}{U_\infty}, \tag{4.1}$$

   and the added turbulence intensity as

$$I = I_\infty + \sqrt{\sum_{i=1}^{1} I_{+,i}^2}. \tag{4.2}$$

5. Move on to the second upstream turbine position ($i = 2$) to then sample and compute: $U_{\infty,2} = \langle U \rangle_{\text{AD},z_h,2}$ and $I_{\infty,2} = \langle I \rangle_{\text{AD},z_h,2}$.
6. Access the look-up table (LUT) with both $U_{\infty,2}$ and $I_{\infty,2}$ to obtain: P_2, $\frac{\Delta U}{U_{\infty,2}}$ and I_2^+.

[1] In geometry, a segment is a continuous line bounded in between two defined end-points that contains all the points that are on the line and in between the end-points.

(7) Reconstruct the accumulated wake by linearly summing the velocity deficit as

$$\frac{\Delta U}{U_\infty} = \sum_{i=1}^{2} \frac{\Delta U}{U_{\infty,i}} \frac{U_{\infty,i}}{U_\infty}, \tag{4.3}$$

and the added turbulence intensity as

$$I = I_\infty + \sqrt{\sum_{i=1}^{2} I_{+,i}^2}. \tag{4.4}$$

(8) etc.

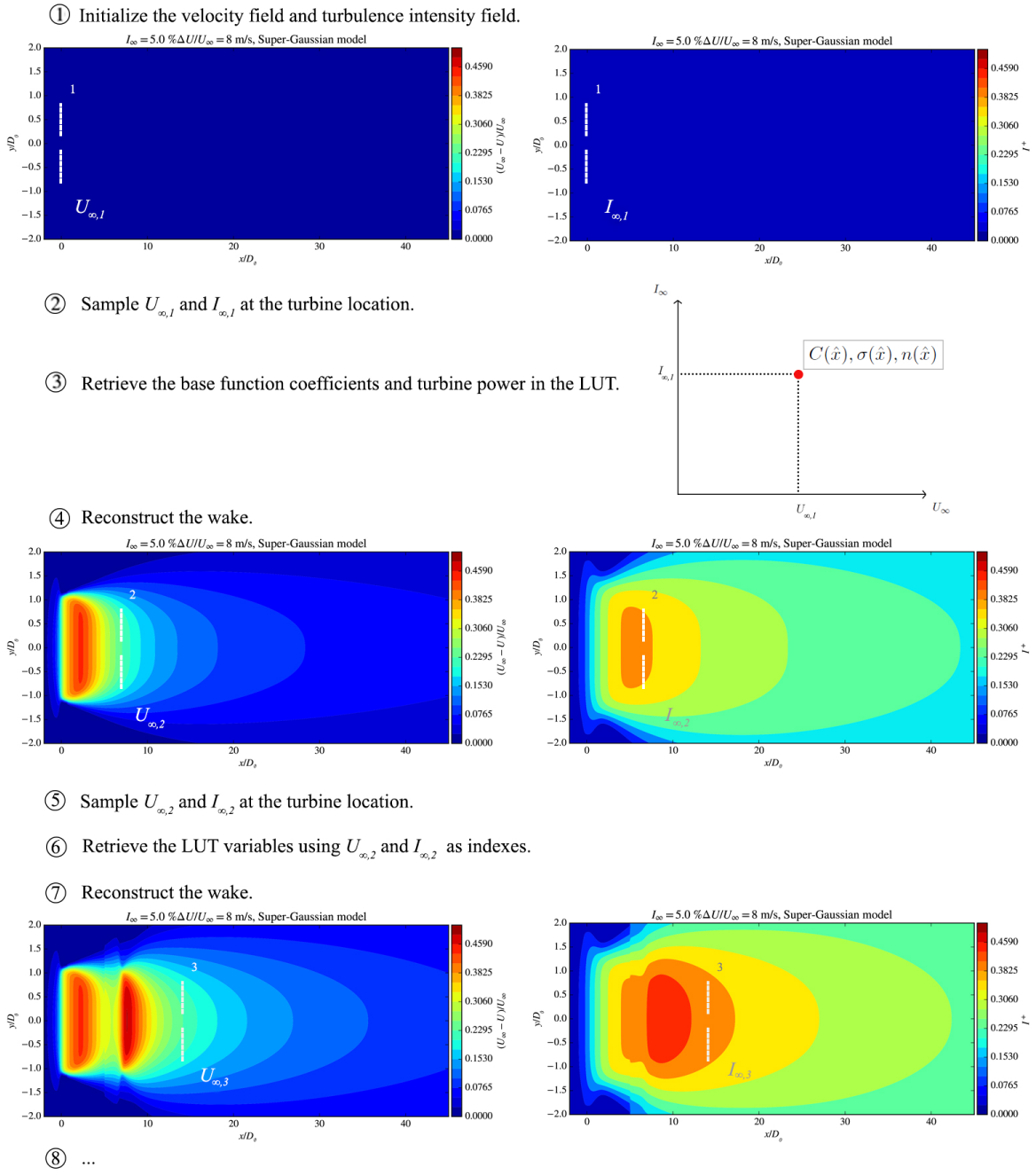

Figure 4.1: graphical representation of the superposition algorithm used to build the accumulated wake of a wind farm composed of 2R-V29 turbines.

Both variables $U_{\infty,i}$ and $I_{\infty,i}$ refer to the freestream atmospheric variables seen by the i^{th} turbine at hub height. Hereunder, algorithm 1 presents the complete step by step description to construct an accumulated wake from the set of individual MR2 wakes stored in the look-up tables, Ψ.

Algorithm 1: MR2 wake superposition modus operandi.

input : Look up tables $\Psi(I_\infty, U_\infty, \hat{x})$ generated by algorithm 2, inflow wind conditions and MR2 turbine locations within the wind farm.

output: Accumulated velocity deficit field $\Delta U/U_\infty$ and added turbulence intensity I^+ at $z = z_h$.

1 Initialize the velocity U and turbulence intensity I field with the inflow conditions U_∞ and I_∞ respectively;
2 Sort the wind turbines WTs by their axial position x;
3 N=0;
4 **for** WT_i *in* WTs **do**
5 N=N+1;
6 Sample and compute the freestream wind conditions seen by the MR2 turbine i as: $U_{\infty,i} = \langle U \rangle_{AD,zh,i}$ and $I_{\infty,i} = \langle I \rangle_{AD,zh,i}$, where the operator $\langle\ \rangle_{AD,zh,i}$ refers to the average of the two geometrical segments obtained by intersecting both actuator disks of the i^{th} MR2 turbine with the hub height plane ($z = z_h$);
7 Obtain the velocity deficit $\frac{\Delta U}{U_{\infty,i}}$, the added turbulence intensity, I_i^+, and the power, P_i, of the i^{th} turbine from the look-up table: $\Psi(U_{\infty,i}, I_{\infty,i}, \hat{x})$;
8 Linearly superpose the velocity deficit as $\frac{\Delta U}{U_\infty} = \sum_{i=1}^{N} \frac{\Delta U}{U_{\infty,i}} \frac{U_{\infty,i}}{U_\infty}$;
9 Superpose the turbulence intensity as: $I = I_\infty + \sqrt{\sum_{i=1}^{N} I_{+,i}^2}$;
10 **end**

Since the model only resolves the hub height plane, the sampling methods: $U_{\infty,i} = \langle U \rangle_{AD,zh,i}$ and $I_{\infty,i} = \langle I \rangle_{AD,zh,i}$ are chosen as representative of the wind turbine operating conditions after having compared three different sampling methods in section C.1. Then, the linear velocity superposition model is defined after comparing two models: linear sum and the root of squared sum in section C.3. Finally, the turbulence intensity superposition model is selected so as to better predict the wake velocity, despite over-predicting the wake turbulence intensity. The latter since the output power of the MR2 turbine is more sensitive to the velocity than to the turbulence intensity as seen in Figure 3.2b. The complete study of three different turbulence intensity superposition methods is addressed in section C.2. The fully defined surrogate model is now tested for an aligned row of four 2R-V29 turbines in section 4.2 and for a 3×3 wind farm in chapter 5.

4.2. Four 2R-V29 turbines inline

The present section tests the fully defined surrogate model for a row of four aligned 2R-V29 wind turbines with a varying range of turbines inter-spacing, $3D_0 \leq S \leq 9D_0$, subjected to a range of atmospheric U_∞ and I_∞. Table 4.1 presents the sampling and superposition methods used to merge the single wakes, where the teal colored variables represent variables extracted from the look-up tables.

Table 4.1: surrogate model setup to handle wake superposition. N is the total number of MR2 turbines.

$U_{\infty,i}$ sampling method	$\langle U \rangle_{\mathrm{AD},z_h,i}$
$I_{\infty,i}$ sampling method	$\langle I \rangle_{\mathrm{AD},z_h,i}$
I^+ superposition method	$I = I_\infty + \sqrt{\sum_{i=1}^{N} I_{+,i}^2} \rightarrow I^+ = \sqrt{I^2 - I_\infty^2}$
$\Delta U/U_\infty$ superposition method	$\sum_{i=1}^{N} \left[\frac{\Delta U}{U_{\infty,i}} \right] \frac{U_{\infty,i}}{U_\infty}$

This section tests two combinations of look-up table surrogate model based on the following functions:

- Super-Gaussian $\frac{\Delta U}{U_\infty}$ LUT + super-Gaussian I^+ LUT
- Double-Gaussian $\frac{\Delta U}{U_\infty}$ LUT + super-Gaussian I^+ LUT

Both the super-Gaussian LUT model and the double-Gaussian model are compared to the higher fidelity RANS simulations where two main parameters are selected as representative of the model accuracy:

- the wind farm power, and
- the wake profile at the potential 5^{th} turbine location.

Figure 4.2 shows the normalized power output of the four MR2 turbines obtained through the surrogate models and compared to the RANS simulation for an inflow condition of U_∞ = 8 m/s, thus at maximum loading (C_T). As expected, the wake velocity deficit recovers faster for higher I_∞ thus allowing down-wind turbines to produce more power.

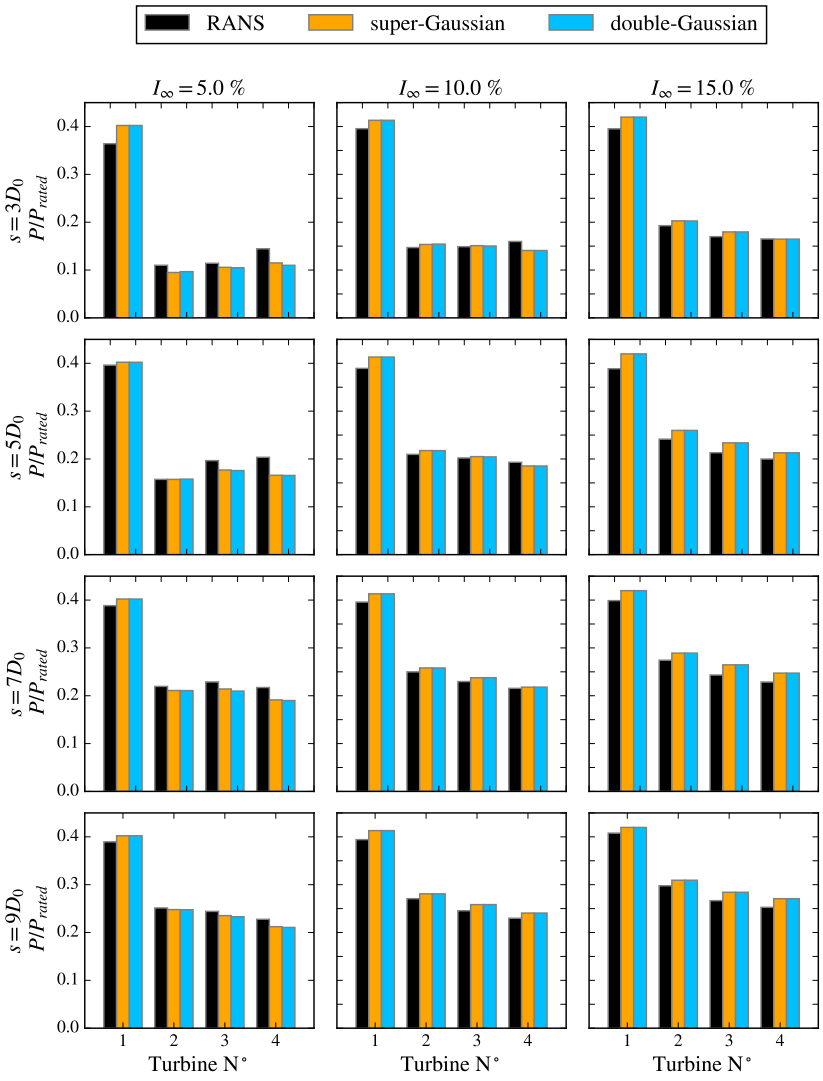

Figure 4.2: power output normalized by the rated power of each 2R-V29 turbine for an inflow condition of $U_\infty = 8$ m/s as a function of the inter-spacing distance, S, and the turbulence intencity, I_∞, at hub height.

The relative power error of each turbine i is computed as

$$\text{ERR}_{P_i,\text{model}} = \frac{|P_{i,\text{RANS}} - P_{i,\text{model}}|}{P_{i,\text{RANS}}}, \tag{4.5}$$

where P_i is the output power of the i^{th} MR2 turbine. Moreover, the whole wind farm relative error is computed as

$$\text{ERR}_{WFP,\text{model}} = \frac{|\sum_{i=1}^{N} P_{i,\text{RANS}} - P_{i,\text{model}}|}{\sum_{i=1}^{N} P_{i,\text{RANS}}}, \tag{4.6}$$

where N is the total number of 2R-V29 turbines i.e. $N = 4$.

Table 4.2: $\mathrm{ERR}_{WFP,\text{super-Gauss}}$ [%] for $U_\infty = 8$ m/s at z_h.

		I_∞ [%]		
		5	10	15
inter-spacing	$3D_0$	2.0	0.9	4.8
	$5D_0$	5.4	2.7	8.0
	$7D_0$	3.3	3.3	6.6
	$9D_0$	1.3	4.6	4.8

Table 4.3: $\mathrm{ERR}_{WFP,\text{double-Gauss}}$ [%] for $U_\infty = 8$ m/s at z_h.

		I_∞ [%]		
		5	10	15
inter-spacing	$3D_0$	2.6	0.8	4.7
	$5D_0$	5.5	2.6	8.0
	$7D_0$	3.9	3.3	6.6
	$9D_0$	1.7	4.6	4.8

Table 4.2 shows the relative error of the total wind farm power predicted by the LUT model based on the super-Gaussian function for $\Delta U/U_\infty$. Analogously, Table 4.3 shows the relative error for the LUT model based on the double-Gaussian function. Both models show similar power outputs and thus similar errors with an average error of approximately 4%. These similarities are expected since both double- and super-Gaussian velocity deficits tend to a second-order Gaussian function in the far-wake as seen in Figure 4.3 which shows the velocity deficit profile at an hypothetical fifth turbine location.

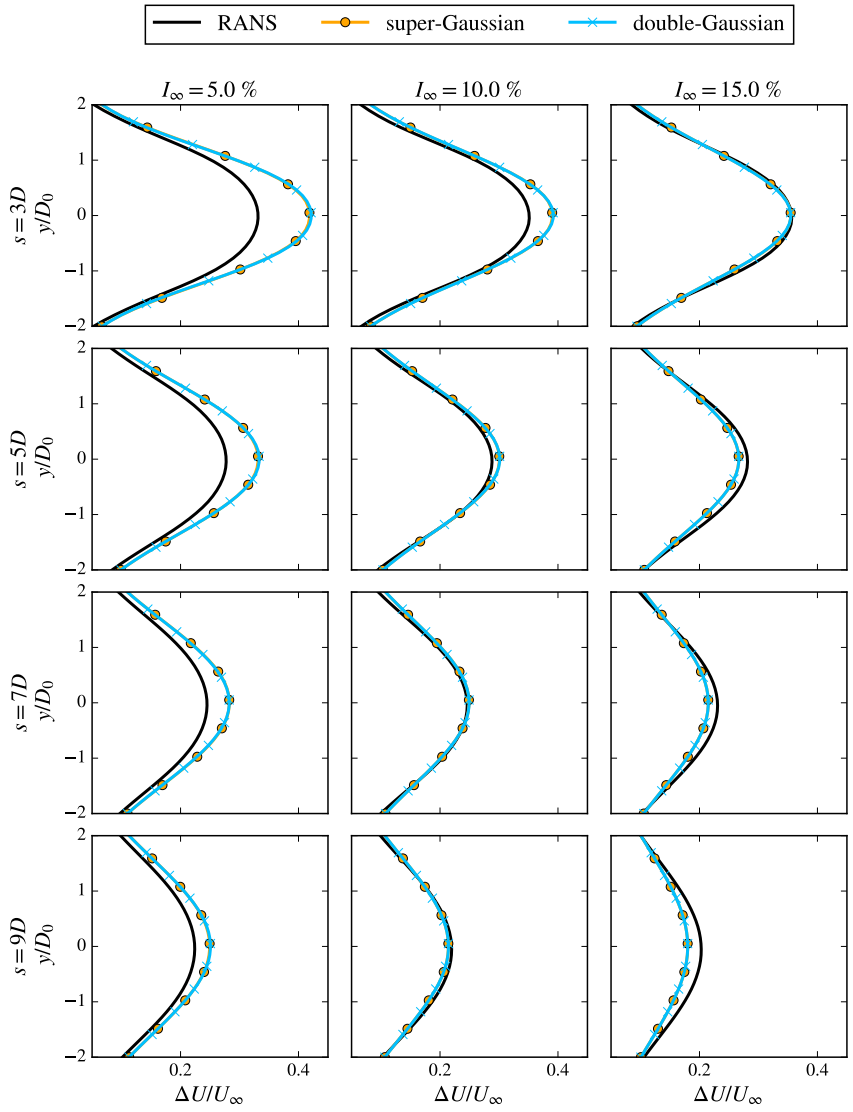

Figure 4.3: velocity deficit profile at the axial position of the potential 5^{th} MR2 turbine. The RANS profile is compared to the $\Delta U/U_\infty$ LUT model based on the super-Gaussian function and the $\Delta U/U_\infty$ LUT model based on the double-Gaussian function.

Figure 4.3 shows the velocity deficit profile at the location of the potential fifth turbine if the inter-space distance were to be kept equal. It is seen that both super-Gaussian and double-Gaussian models predict similar wake profiles at this location. Compared to the higher fidelity RANS simulation, there is an over-estimation of $\Delta U/U_\infty$ for $I_\infty = 5\%$ and a slight under-estimation at high I_∞ and greater inter-spaces.

At $I_\infty = 5\%$ there is an under-estimation of the wake recovery. In order to find out the cause of the $\Delta U/U_\infty$ over-estimation, the accumulated wake obtained at $U_\infty = 8$ m/s, $I_\infty = 5\%$ and $S = 3D_0$ (worst case scenario) is sketched in Figure 4.4. As it is expected, the added turbulence intensity I^+ is overestimated due to the used turbulence intensity superposition selected in section C.2. Therefore, the $\Delta U/U_\infty$ over-estimation of the accumulated wake might be due to the velocity deficit superposition method, which may not be linear in the very near wake[2]. Similar results were found in [Gunn et al., 2016] where the linear superposition of single-rotor wakes leads to an overestimation of the velocity deficit.

At $I_\infty = 15\%$, the wake $\Delta U/U_\infty$ is under-predicted for the higher inter-spacing distances i.e. $S = 9D_0$. The latter, might be attributed to the over-prediction of the wake turbulence intensity which triggers a faster wake recovery compared to the RANS simulations. This over-estimation of the wake recovery is also causing the over-prediction of output power seen in Figure 4.2 for $I_\infty = 15\%$.

[2]Very near wake since the distance of $3D_0$ is accounted from tower to tower, thus there is a minimum physical clearance of $1D_0$ between rotor tips.

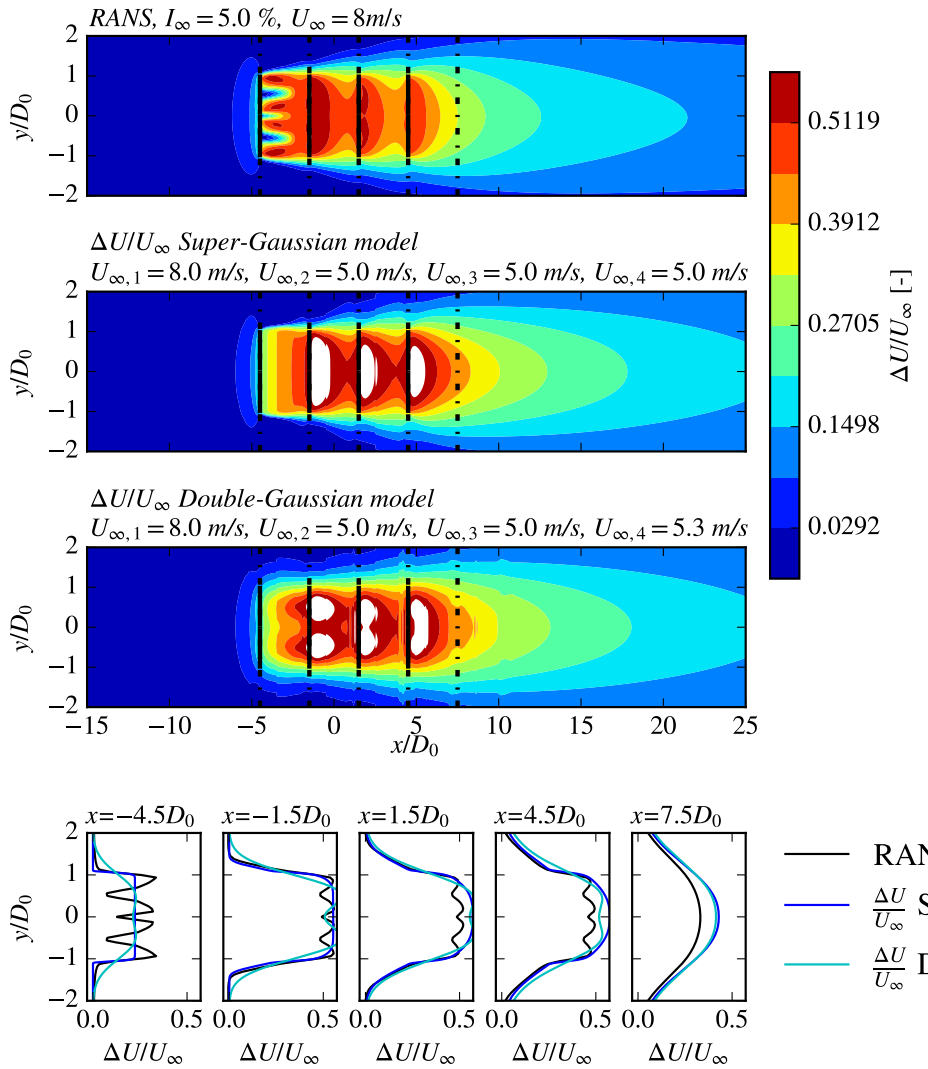

(a) $\Delta U/U_\infty$ profile

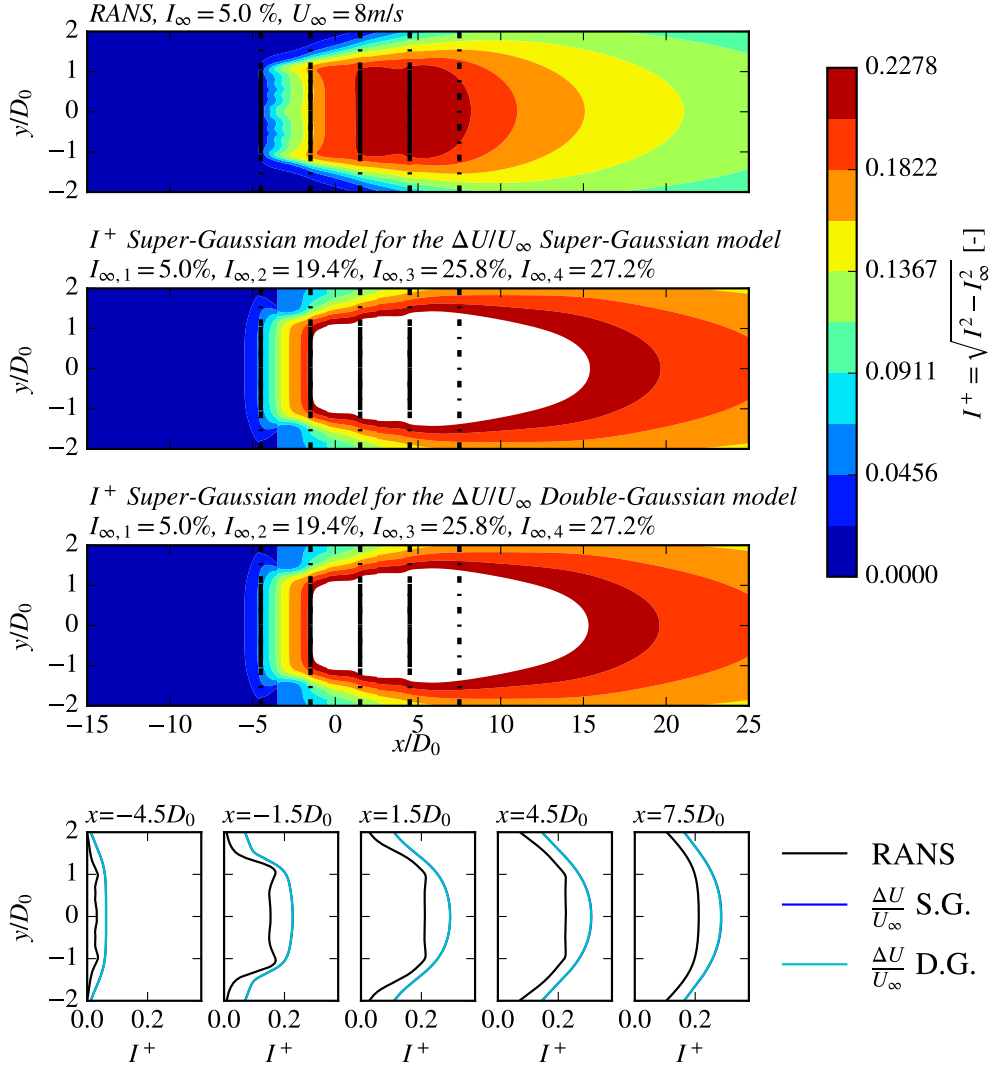

(b) I^+ profile

Figure 4.4: wake of four aligned MR2 turbines distanced $3D_0$ and subjected to $U_\infty = 8$ m/s and $I_\infty = 5\%$. The top row is obtained from RANS simulations, the second row correspond to the $\Delta U/U_\infty$ LUT model with the super-Gaussian base function and the third row corresponds to the LUT model with the double-Gaussian base function.

5
Multi-rotor wind farm modeling

So far, two combinations of analytical surrogate wake model based on look-up tables have been derived and compared against higher fidelity RANS simulations of a set of four aligned MR2 turbines modeled for a range of inter-spacing distances, and a range of U_∞ and I_∞, where an accuracy greater than 90 % (in comparison to RANS) has been observed while computing the total output power of the four aligned turbines.

This chapter aims to test the derived LUT surrogate models in a wind-farm environment for a generic squared layout of 3×3 MR2 wind turbines of the type 2R-V29. In order to do so, RANS-AD simulations are run for a range of turbine inter-spacing $S = [5,7]D_0$ subjected to $I_\infty = 5\%$ and a range of $U_\infty = [8,10,13,16]$ m/s at z_h as summarized in Table 5.1. For the sake of shortening the computational time, only the lowest turbulence intensity, $I_\infty = 5\%$, is evaluated and eight cells are used to discretize one rotor diameter ($N_{CD} = 8$) within the wake refinement box instead of 16.

The mesh implemented in the present section is described in subsection 2.7.4. To study the influence from the 360° wind directions on the wind farm, we took advantage of the wind farm rotational-symmetric layout [van der Laan et al., 2022] and thus saved computational time by only modelling a span of 90°.

Table 5.1: simulated configurations for the $3\times3\times$MR2 wind farm layout.

Inter-spacing S [m]	$5D_0$	$7D_0$
Modelled wind directions [°]	[0, 10, 20, 30, 40, 50, 60, 70, 80]	[0, 15, 30, 45, 60, 75]
U_∞ [m/s]	$[8,10,13,16]$	
I_∞ [%]	5	

To estimate the performances of the LUT surrogate models in comparison to already existing engineering models applied in the industry, the Park2 model and the turbo-Gaussian-deficit are included in the analysis.

5.1. Existing engineering wake models

This section introduces two engineering wake models, the PARK2 and the turbo-Gaussian model, both traditionally implemented in the industry to quickly iterate in between different wind farm designs i.e. to maximize the power output.

Park2

Park2 is the revised wind farm wake model derived by DTU Wind Energy [Rathmann et al., 2018]. The model makes use of the classical top-hat velocity deficit profile

$$\Delta U_i(\hat{x}) = U_{\infty,i}\left[1-\sqrt{1-C_T\left(U_{\infty,i}\right)}\right]\left[\frac{D_0}{D_i^{\text{wake}}\,\hat{x}}\right]^2, \tag{5.1}$$

where $U_{\infty,i}$ is the freestream velocity felt by the i^{th} turbine. Then, C_T is the thrust coefficient and D_0 is the turbine rotor diameter i.e. $D_0 = 29.2$ m for the V29 turbine. Moreover, the wake diameter D_i^{wake} at a relative distance $\hat{x}$ from the turbine rotor is defined as

$$D_i^{\text{wake}}(\hat{x}) = D_0 + 2k\hat{x}, \tag{5.2}$$

where $k = 0.06$ is the calibrated wake expansion coefficient according to [Rathmann et al., 2018].

When wakes are combined, the local incident wind speed U_i is used to compute each wake deficit, and the partial overlap of the i^{th} wake upstream of turbine j is taken into account within the linear sum of the velocity:

$$U_j = U_\infty - \sum_i^{N_j^+} \Delta U_i(\hat{x}_j) \frac{A_{i,j}^{\text{overlap}}}{A_0}, \tag{5.3}$$

where N_j^+ is the number of rotors located up-wind turbine j, $\hat{x}_j$ is the axial distance from turbine i to turbine j, $A_{i,j}^{\text{overlap}}$ is the overlapping area of the wake i on the rotor j; and A_0 is the V29 rotor area defined as $A_0 = \pi D_0^2/4$ for the present thesis.

Turbo-Gaussian-deficit

Also known as the TurbOPark model, it is based on the Gaussian wind speed deficit of [Bastankhah and Porté-Agel, 2014] presented in Equation 1.3.2

$$\Delta U_i(\hat{x}) = U_{\infty,i} C_i(\hat{x}) \exp\left[-\frac{\hat{r}^2}{2\sigma_{w,i}^2(\hat{x})} \right], \tag{5.4}$$

where $\hat{x}$ is the axial distance from the local i^{th} turbine's reference system, $\hat{r}$ is the local radial distance, and the characteristic wake width of the i^{th} turbine wake is defined as

$$\frac{\sigma_{w,i}(\hat{x})}{D_0} = \epsilon_i + \frac{A I_\infty}{\beta} \left(\sqrt{\left(\alpha + \beta \hat{x}/D_0\right)^2 + 1} - \sqrt{1+\alpha^2} - \ln\left[\frac{\left(\sqrt{\left(\alpha + \beta \hat{x}/D_0\right)^2 + 1} + 1\right)\alpha}{\left(\sqrt{1+\alpha^2}+1\right)\left(\alpha + \beta \hat{x}/D_0\right)} \right] \right), \tag{5.5}$$

where $\alpha = c_1 I_\infty$, $\beta = c_2 I_\infty / \sqrt{C_{T,i}(U_{\infty,i})}$. $c_1 = 1.5$ and $c_2 = 0.8$ according to [Frandsen, 2007], the wake expansion calibration parameter $A = 0.04$ according to [Nygaard et al., 2020], and the initial wake width at $\hat{x} = 0$ is defined as

$$\epsilon_i = 0.25 \left(\frac{1 + \sqrt{1 - C_T\left(U_{\infty,i}\right)}}{2\sqrt{1 - C_T\left(U_{\infty,i}\right)}} \right)^{1/2}. \tag{5.6}$$

Finally, the peak deficit variable C_i is defined as

$$C_i(\hat{x}) = 1 - \sqrt{1 - \frac{C_{T,i}\left(U_{\infty,i}\right)}{8\left(\sigma_{w,i}(\hat{x})/D_0\right)^2}}. \tag{5.7}$$

5.2. Multi-rotor wind farm results

Figure 5.1 shows the RANS and engineering models predicted efficiency of the 3×3 MR2 wind farm spaced $S = 5D_0$, subjected to $I_\infty = 5\%$ and $U_\infty = 8$ m/s at hub height. The left side corresponds to the modelled 90°, and the right side contains the same information but symmetrically rotated.

The total efficiency η of the wind farm as a function of the wind speed and wind direction, is computed as

$$\eta(U_\infty, \text{WD}) = \frac{1}{N} \sum_{i=1}^{N} \frac{P_i(\text{WD})}{P_{\text{rated}}}, \tag{5.8}$$

where N is the total amount of rotors, P is the modelled output power and P_{rated} is the rated power of the rotor, i.e. the rated power of the Vestas® V29 turbine.

For the sake of brevity, only the most dissimilar case ($S = 5D_0$ and $U_\infty = 8$ m/s at z_h) is shown in Figure 5.1, and the model performances with respect to RANS simulations are compared for $S = 5D_0$ in Table 5.2. However, the full set of results can be found in Appendix D.

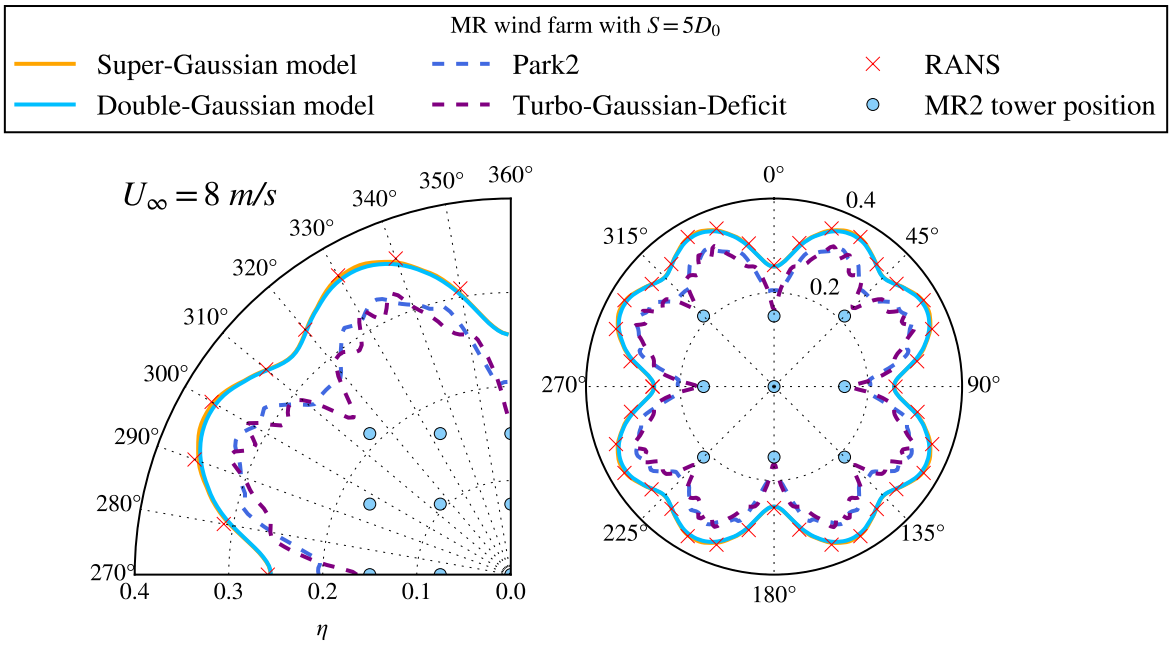

Figure 5.1: wind farm efficiency as a function of the wind direction for the 3 × 3 MR2 wind farm spaced $S = \mathbf{5}D_0$ and subjected to $I_\infty = 5\%$ and $U_\infty = 8$ m/s at hub height. Results obtained from both double- and super-Gaussian LUT models, Park2 and Turbo-Gaussian-deficit models, all compared against higher fidelity RANS simulations. The left plot is a zoom of the right plot and the wind farm layout is shown with cyan dots.

Based on the efficiency, the wind farm power output difference in between the surrogate models and the RANS model is compared for each wind speed, U_∞, as:

$$E_{\text{model}}(U_\infty, \text{WD}) = \frac{\sum_{i=1}^{N} P_{\text{model},i}(\text{WD}) - \sum_{i=1}^{N} P_{\text{RANS},i}(\text{WD})}{\sum_{i=1}^{N} P_{\text{RANS},i}(\text{WD})}, \tag{5.9}$$

where N is the total amount of wind turbines and P_i refers to the power produced by the i^{th} turbine. Moreover, in order to obtain a global performance of the model, an average over all the RANS-modelled-wind-directions is computed for each wind speed, U_∞, as

$$E_{\text{model, AVG}}(U_\infty) = \frac{\sum_{\text{WD}=1^\circ}^{360^\circ} \left[\sum_{i=1}^{N} P_{\text{model},i}(\text{WD}) - \sum_{i=1}^{N} P_{\text{RANS},i}(\text{WD})\right]}{\sum_{\text{WD}=1^\circ}^{360^\circ} \sum_{i=1}^{N} P_{\text{RANS},i}(\text{WD})}. \tag{5.10}$$

Table 5.2: E_{model} [%] and $E_{\text{model, AVG}}$ [%] for the 3 × 3×MR2 layout with $S = \mathbf{5}D_0$.

Model		Double-Gassian LUT				Super-Gassian LUT				N.O. Jensen				Turbo-Gaussian			
	U_∞ [m/s]	8	10	13	16	8	10	13	16	8	10	13	16	8	10	13	16
Wind direction [°]	0	-1.1	-0.7	0.2	-0.4	-1.2	-0.8	0.1	-0.3	-20.9	-16.3	-0.9	-3.3	-36.6	-37.1	-28.9	-4.5
	10	-2.4	-1.9	0.0	0.2	-2.8	-2.6	-0.5	0.3	-17.3	-14.3	-4.8	-2.3	-16.2	-15.8	-9.6	-2.2
	20	-1.3	-1.6	-0.7	0.2	-2.0	-2.4	-0.9	0.2	-14.7	-12.3	-5.3	-2.0	-15.5	-14.1	-6.7	-2.0
	30	-0.5	-0.8	-1.1	0.1	-1.4	-1.5	-1.2	0.1	-14.4	-12.2	-5.1	-2.1	-12.3	-10.7	-5.4	-2.1
	40	-0.2	-0.5	-1.1	0.2	-0.4	-0.7	-1.1	0.2	-17.3	-14.6	-5.5	-2.1	-15.0	-13.1	-5.8	-2.1
	50	-0.4	-0.8	-1.2	0.2	-0.6	-0.9	-1.2	0.2	-17.4	-14.8	-5.6	-2.1	-15.1	-13.2	-5.9	-2.1
	60	-0.6	-0.7	-1.0	0.1	-1.4	-1.5	-1.2	0.1	-14.4	-12.2	-5.1	-2.1	-12.4	-10.7	-5.4	-2.1
	70	-1.2	-1.5	-0.7	0.2	-1.9	-2.2	-0.9	0.2	-14.6	-12.2	-5.3	-2.0	-15.3	-13.9	-6.7	-2.0
	80	-2.2	-1.7	0.1	0.2	-2.6	-2.3	-0.4	0.3	-17.1	-14.0	-4.6	-2.3	-16.0	-15.5	-9.5	-2.2
	AVG	-1.1	-1.1	-0.6	0.1	-1.6	-1.7	-0.8	0.1	-16.3	-13.5	-4.8	-2.3	-16.6	-15.3	-9.1	-2.4

As shown in Table 5.2, both LUT surrogate models are an order of magnitude more accurate than the Park2 and Turbo-Gaussian models with generic calibrated constants. Qualitatively, this is an expected result since the LUT surrogate models make use of more data from the 2R-V29 turbine i.e. a whole set of individual 2R-V29 wakes run for a range of U_∞ and I_∞, while the Park2 and turbo-Gauss models only use the $C_T(U_\infty)$ curve of the single-rotor V29 turbine. Nonetheless, this analysis shows the quantitative gains of using a more complex surrogate model as it is the case of both double- and super-Gaussian based LUT models.

Both LUT models estimations are in good agreement with RANS results. The greatest difference takes place for the smallest turbine inter-space $S = 5D_0$, $U_\infty = 8$ m/s and WD= 280° with a 2.8% (super-Gaussian model) and 2.4% (double-Gaussian model) underestimation of the total power produced by the wind farm. Figure 5.2 shows the velocity deficit for the latter condition. At WD= 10° the second and third row of MR2 turbines are partially operating in the wake of the upstream turbines, thus leading to a non-uniform loading of both V29 rotors of the MR2 turbine. Looking at the zoomed-in area of the top-right MR2 turbine, it is seen that within the RANS simulation, the upper rotor operates at a higher C_T since its $\langle U \rangle_{AD}$ is greater than the lower rotor which operates in a wake, and thus at a lower C_T. On the other hand, since both LUT surrogate models are build on even base functions[1] and trained on a uniform atmospheric surface layer (ASL) inflow profile, the models cannot represent the asymmetric loading of the MR2 turbine. Instead, they sample both segments resulting from the intersection of the two rotor disks with the $z = z_h$ plane, average the velocity and apply a symmetric wake. Therefore, the models evenly distribute the load in between the two rotors, hence overloading the shaded rotor and thus leading to an excessive velocity deficit as seen on Figure 5.2.

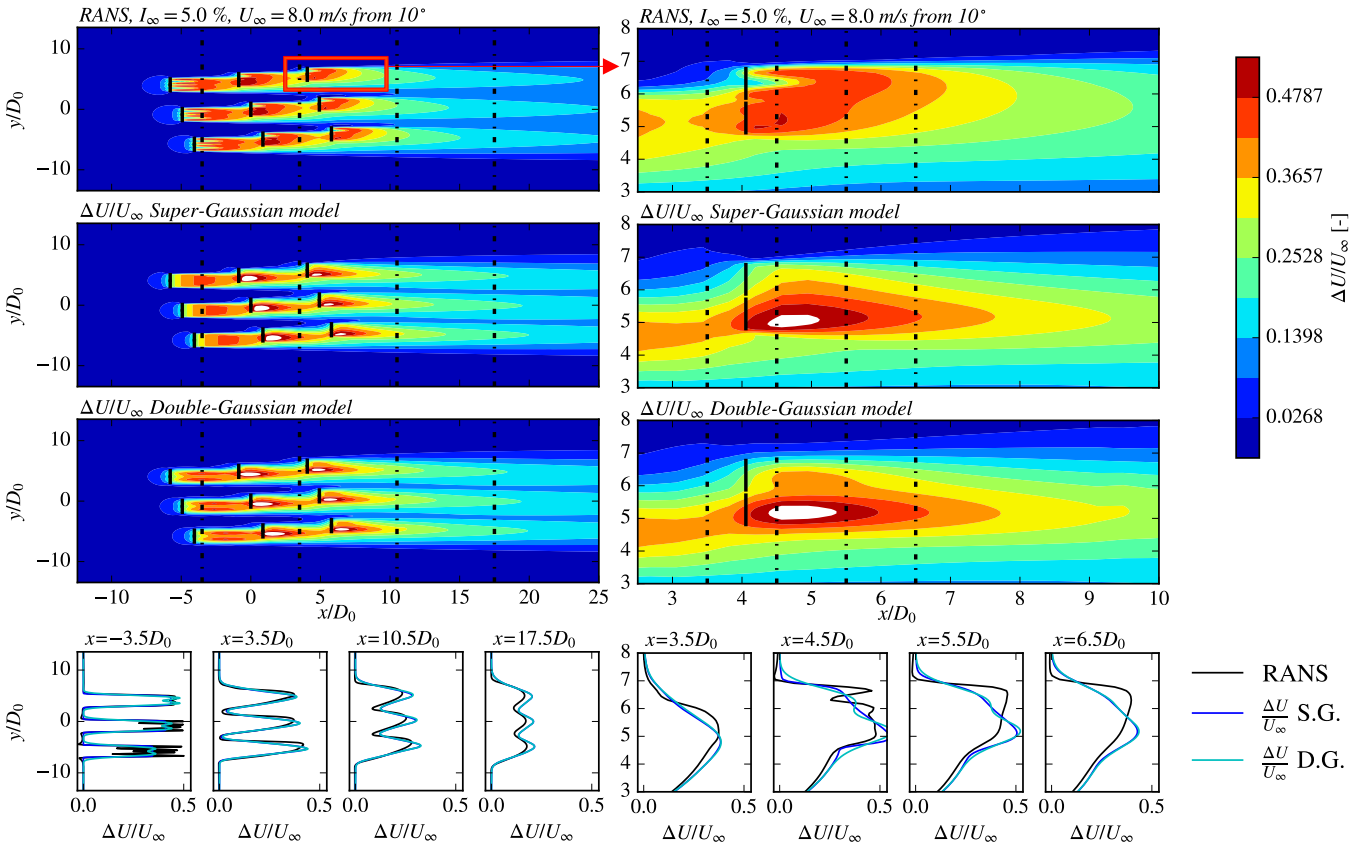

Figure 5.2: velocity deficit of the 3×3 MR2 wind farm spaced $S = 5D_0$, subjected to $I_\infty = 5\%$ and $U_\infty = 8$ m/s from WD= 10° at hub height. $\Delta U/U_\infty$ obtained from RANS simulations and both double- and super-Gaussian LUT surrogate models. The white coloring represents out of scale velocities.

[1] A function $\mathcal{F}$ is even if $\mathcal{F}(\hat{y}) = \mathcal{F}(-\hat{y})$

6

Single-rotor wind farm vs. multi-rotor wind farm

This final chapter evaluates whether the total power output of a wind farm is greater by installing nine multi-rotor turbines of the type 2R-V29 or 18 single rotor turbines of the type V29 if the total wind farm area were to be kept equal.

The mesh implemented in the present section is described in subsection 2.7.4. For the comparison to be fair, both layouts are optimised to maximise the minimum distance in between turbines within the same outer square area of $4S^2$. Since both wind farms are composed of 18 Vestas® V29 rotors, both wind farms have the same total rated power.

For the added turbulence intensity, I^+, of the turbines to lead the wake recovery instead of I_∞, the lowest ambient turbulence intensity, $I_\infty = 5\%$, is evaluated for a range of space factors[1] $S = [5,7]D_0$ and $U_\infty = [8,10,13,16]$ m/s at z_h as summarized in Table 6.1. Indeed, higher ambient turbulence intensities, I_∞, would foster the wake recovery, thus homogenizing the accumulated wakes generated by different types of turbines. To represent every wind direction influence (360°) on both wind farms, we took advantage of the wind farm rotational-symmetric layout [van der Laan et al., 2022] and thus saved computational time by only modelling a span of 90° for the multi-rotor wind farm and a sweep of 180° for the single-rotor wind farm.

Table 6.1: simulated configurations for both the $3 \times 3 \times$MR2 wind farm layout and the $18 \times$SR layout.

Space factor S [m]	$5D_0$	$7D_0$
Modelled wind directions [°]	[0, 10, 20, 30, 40, 50, 60, 70, 80]	[0, 15, 30, 45, 60, 75]
U_∞ [m/s]	$[8,10,13,16]$	
I_∞ [%]	5	

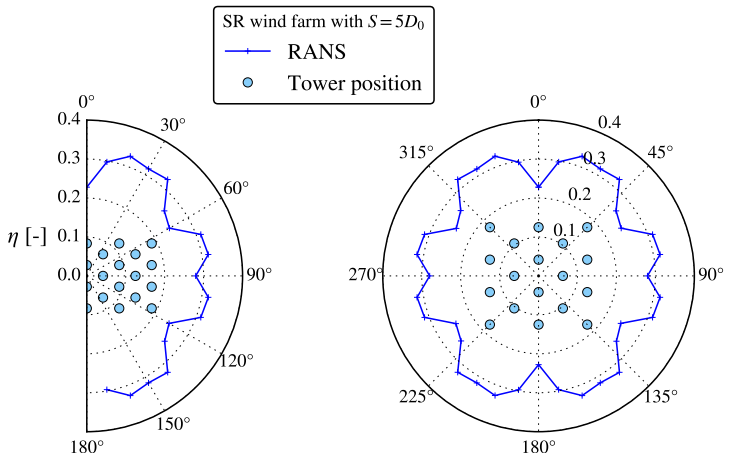

Figure 6.1: wind farm efficiency as a function of the wind direction for the 18 single-rotor wind farm with $S = \mathbf{5}D_0$, subjected to $I_\infty = 5\%$ and $U_\infty = 8$ m/s at z_h. The left plot is a zoom of the right plot and the wind farm layout is shown with cyan dots.

[1]Throughout the present chapter the variable S is referred as the characteristic space factor since for the single-rotor farm it does not represent the inter-spacing in between the V29 turbines.

6.1. Single-rotor wind farm results

This section presents the total power efficiency of the single-rotor wind farm obtained from RANS-AD simulations.

Since the actuator disks input both an axial and tangential load, the wake rotates. Hence, there is a 180° rotational symmetry of the flow of the single-rotor farm. Therefore, only the wind directions of the left image of Figure 6.1 are modelled and then accordingly rotated in order to complete the 360° wind directions.

Due to the turbines layout, there is a higher number of turbines shading each other or tower alignment for $(0°,\ 56°20',\ 90°,\ 123°40') \times n180°$ for $n \in \mathbb{N}$, hence expecting lower wind farm efficiencies around these specific wind directions (WD) as seen in Figure 6.1. Specially for 56°20′ and 123°40′ where two rows of five turbines and two rows of three turbines get aligned.

6.2. Power output comparison

Figure 6.2 sketches the total wind farm efficiency for different wind directions and two studied spacing factors, $S = [5,7]D_0$. In order to compare the power gain of the multi-rotor wind farm over the single-rotor wind farm, the power gain, A_{MR}, is computed as

$$A_{\mathrm{MR}}(U_\infty, \mathrm{WD}) = \frac{\sum_{i=j}^{N_{\mathrm{MR}}} P_{\mathrm{MR},j}(\mathrm{WD}) - \sum_{i=1}^{N_{\mathrm{SR}}} P_{\mathrm{SR},i}(\mathrm{WD})}{\sum_{i=1}^{N_{\mathrm{SR}}} P_{\mathrm{SR},i}(\mathrm{WD})}, \tag{6.1}$$

where $P_{\mathrm{MR},j}$ refers to the power of the j^{th} multi-rotor turbine, $P_{\mathrm{SR},i}$ refers to power of the i^{th} single-rotor turbine, $N_{\mathrm{MR}} = 9$ is the total number of 2R-V29 turbines and $N_{\mathrm{SR}} = 18$ is the total number of V29 turbines. Table 6.2 and Table 6.3 compare the power gain A_{MR} for $S = 5D_0$ and $S = 7D_0$ respectively as a function of the wind direction (WD) for the studied wind speeds.

Then, assuming a uniform wind direction probability, the total power gain of the multi-rotor wind farm is compared with respect to the single-rotor wind farm performances for each studied wind speed, U_∞, as

$$A_{\mathrm{MR,\ total}}(U_\infty) = \frac{\sum_{\mathrm{WD}=1°}^{360°} \left[\sum_{i=j}^{N_{\mathrm{MR}}} P_{\mathrm{MR},j}(\mathrm{WD}) - \sum_{i=1}^{N_{\mathrm{SR}}} P_{\mathrm{SR},i}(\mathrm{WD})\right]}{\sum_{\mathrm{WD}=1°}^{360°} \sum_{i=1}^{N_{\mathrm{SR}}} P_{\mathrm{SR},i}(\mathrm{WD})}. \tag{6.2}$$

Table 6.2: A_{MR} [%] and $A_{\mathrm{MR,\ total}}$ [%], power gain of the MRWF compared to the SRWF for $S = \mathbf{5}D_0$.

Wind direction [°]	U_∞ [m/s] 8	10	13	16
0	10.6	10.8	9.3	0.2
10	1.7	-0.3	-2.6	0.0
20	6.8	6.6	0.9	-0.1
30	12.9	12.1	1.5	-0.2
40	2.5	1.7	-0.2	0.0
50	27.7	26.1	7.4	-1.4
60	46.2	44.6	16.5	-1.5
70	12.0	10.8	1.2	-0.2
80	-4.8	-5.6	-2.9	0.3
90	-9.9	-9.4	-4.8	0.3
100	-4.6	-5.3	-2.7	0.3
110	12.1	10.9	1.2	-0.2
120	46.9	45.5	17.5	-1.6
130	26.9	25.1	6.6	-1.3
140	2.6	1.8	-0.2	0.0
150	13.0	12.2	1.6	-0.2
160	6.7	6.4	0.9	-0.1
170	1.6	-0.3	-2.7	0.0
$A_{\mathrm{MR,\ total}}$	10.6	9.7	2.4	-0.3

Table 6.3: A_{MR} [%] and $A_{\mathrm{MR,\ total}}$ [%], power gain of the MRWF compared to the SRWF for $S = \mathbf{7}D_0$.

Wind direction [°]	U_∞ [m/s] 8	10	13	16
0	7.6	7.7	5.1	0.2
15	1.9	1.6	0.6	0.0
30	10.5	9.1	0.9	-0.1
45	-3.4	-4.4	-1.1	0.4
60	38.4	35.7	8.0	-1.5
75	4.6	4.1	0.8	-0.1
90	-9.6	-9.0	-3.1	0.4
105	4.7	4.2	0.8	-0.1
120	39.2	36.8	8.8	-1.6
135	-3.5	-4.5	-1.1	0.4
150	10.6	9.3	1.0	-0.2
165	1.7	1.3	0.5	0.0
$A_{\mathrm{MR,\ total}}$	7.5	6.7	1.7	-0.2

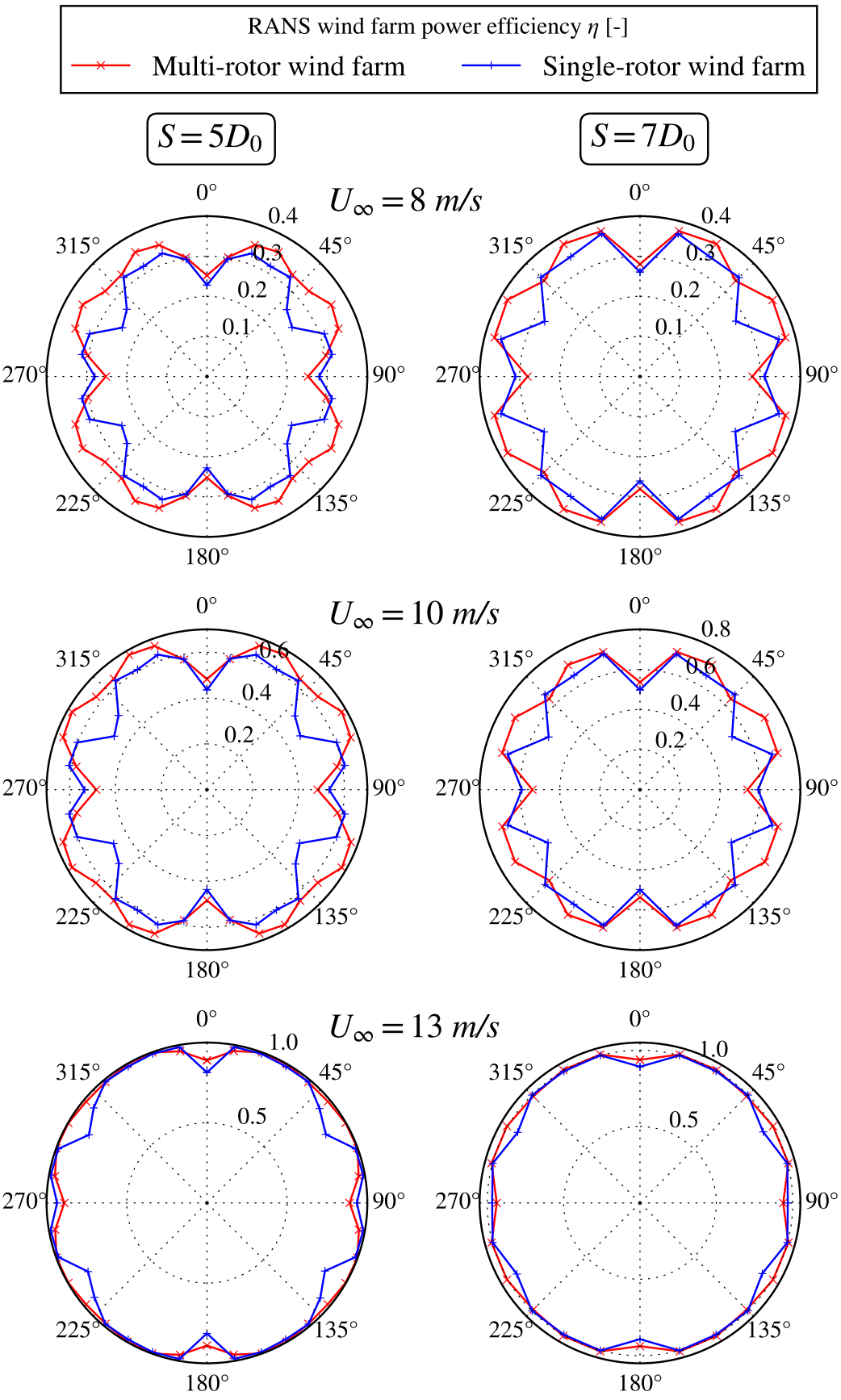

Figure 6.2: multi- and single-rotor wind farm efficiency for different U_∞ as a function of the wind direction for two spacing factors $S = [5,7]D_0$. Results obtained from RANS simulations.

The teal colored power gains that are greater than 20% observed around WD≈ 56° and WD≈ 124° of Table 6.2 and Table 6.3 are due to the previously mentioned high tower alignment of the single-rotor wind farm around those wind directions, which can be visualized in Figure 6.3. Due to the shorter distance in between turbines and the turbine alignment, the single-rotor wind farm operating under this particular condition reaches higher velocity deficits, $\Delta U/U_\infty$, than the multi-rotor wind farm under the same conditions.

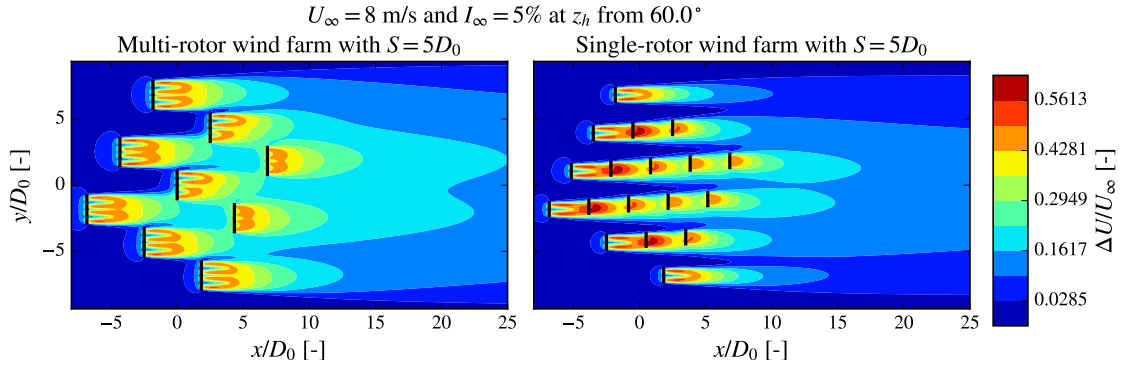

Figure 6.3: velocity deficit of both multi- and single-rotor wind farms with $S = 5D_0$ for $I_\infty = 5\%$ and $U_\infty = 8$ m/s at $z = z_h$ from WD= 60°. Results obtained from RANS simulations.

In general, the more rotors operate in the free-stream, the higher is the wind farm performance, as seen for the WD= 90° condition of Figure 6.4, where the multi-rotor wind farm has six rotors facing the undisturbed incoming wind, while the single-rotor wind farm has seven. Thus, leading to 9.9% higher power production for the single-rotor wind farm.

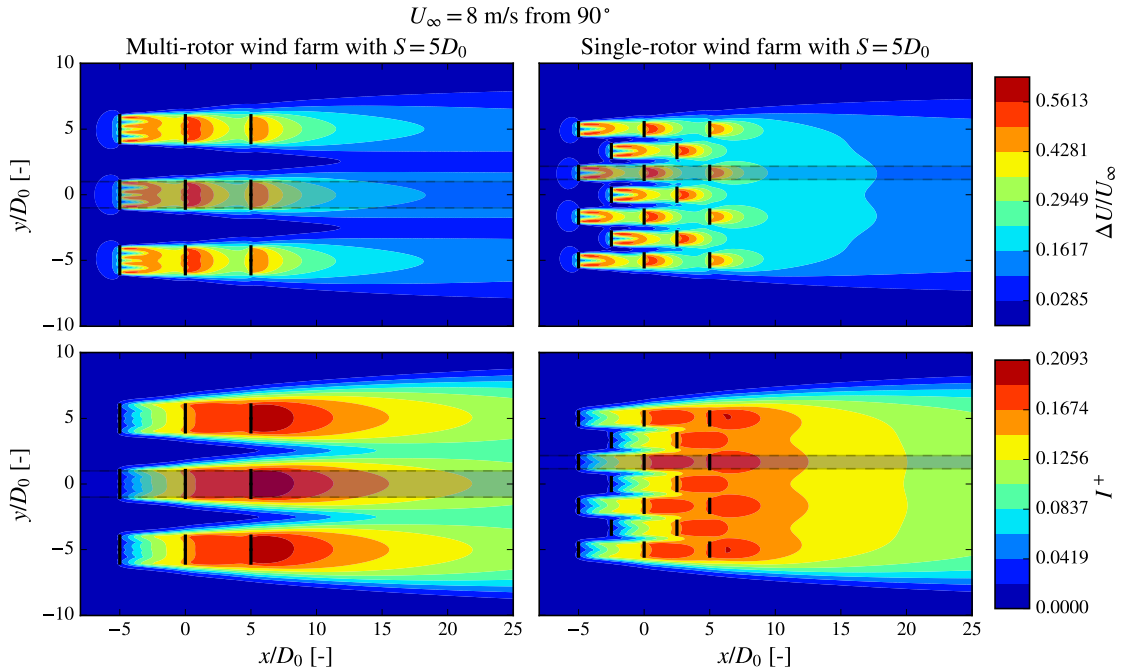

Figure 6.4: first row represents the hub height velocity deficit, $\Delta U/U_\infty$, and the second row sketches the hub height added turbulence intensity, $I^+ = \sqrt{\frac{2}{3}k/U_\infty^2 - I_\infty^2}$, of the multi-rotor wind farm (left) and the single-rotor wind farm (right) with $S = 5D_0$, subjected to $I_\infty = 5\%$ and $U_\infty = 8$ m/s at $z = z_h$ coming from WD= 90°. Results obtained from RANS simulations. The shaded area is further analyzed in Figure 6.5.

The WD= 90° case is unique due to the fact that every turbine is separated an S distance in between each other in the axial direction of the wind. So, the axial velocity and turbulence is further studied for this particular case along the shaded area of Figure 6.4.

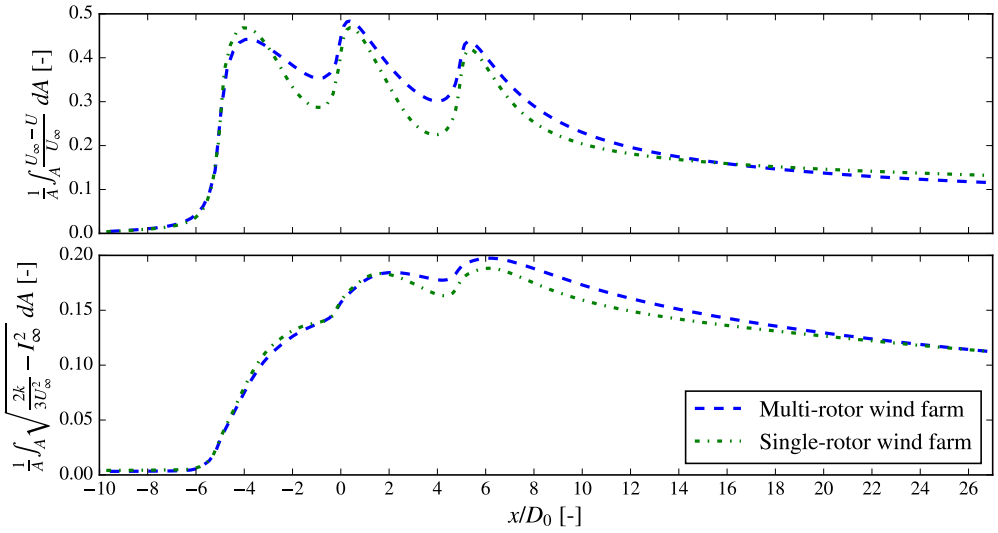

Figure 6.5: RANS predicted wake recovery of the shaded area of Figure 6.4. The first plot represents the actuator disk averaged streamwise velocity deficit and the second sketches the actuator disk averaged added turbulence intensity.

Figure 6.5 shows the actuator disk averaged velocity deficit and added turbulence intensity along the shaded area of Figure 6.4. The streamwise distance is normalized by D_0 and not by the equivalent diameter $D_{eq} = \sqrt{2}D_0$ of the 2R-V29 turbine. Thus, under this scaling, the accumulated single-rotor wake recovers faster than the multi-rotor wake. Nonetheless, the multi-rotor wake adds more turbulence from the second turbine onward ($x > 0D_0$) and thus recovers at a higher rate for $x > 8D_0$.

Figure 6.6 shows the peculiar case when both wind farms with a spacing factor $S = 7D_0$ are subjected to WD= 45°, which is a layout symmetry condition for the multi-rotor wind farm. This condition gives an average speed of 5.55 m/s for the multi-rotor wind farm and 5.63 m/s for the single-rotor wind farm. Thus, leading to a 3 % lower energy production for the multi-rotor farm as seen in Table 6.3. In this case, due to the closer distance of the single-rotor turbines, we observe a greater interaction in between the wakes, specially for the added turbulent intensity I^+.

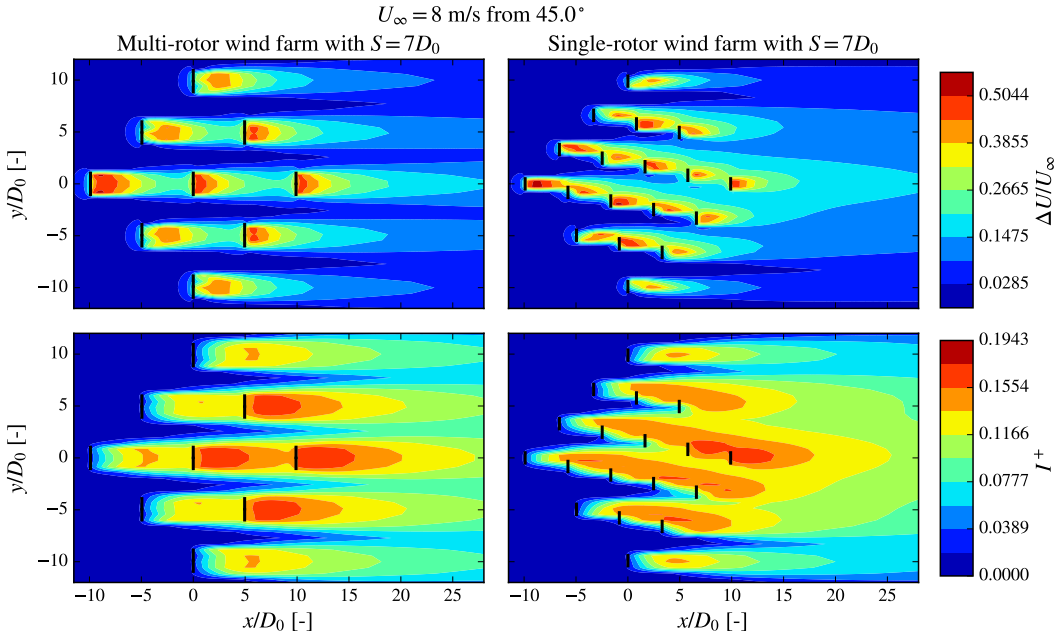

Figure 6.6: first row represents the hub height velocity deficit, $\Delta U/U_\infty$, and the second row sketches the hub height added turbulence intensity, $I^+ = \sqrt{\frac{2}{3}k/U_\infty^2 - I_\infty^2}$, of both wind farms with $S = 7D_0$ for $I_\infty = 5\%$ and $U_\infty = 8$ m/s at $z = z_h$ from WD= 45°. Results obtained from RANS simulations.

Since the RANS-AD disk simulations were run with a Cartesian grid resolution of eight cells per rotor diameter (N_{CD} = 8), the differences of the order of 1% seen at U_∞ = 16 m/s are not further studied. In general terms, we can conclude that above the wind farm rated speed, there is no noticeable difference in between the total power output of both studied wind farms. Moreover, since above rated speed there is a surplus of energy, the wake effects tend to be less harmful since the pitch of the shaded turbines can be turned towards the wind to increase the turbine C_T and C_p.

6.3. Discussion

The multi-rotor layout has shown a total power gains of up to 10% in comparison to the single-rotor wind farm, mainly because the multi-rotor-farm has a lower combination of tower alignments. Furthermore, when turbines get aligned, there is usually a greater physical distance for the wake to recover in between the MR2 turbine-towers than in the single-rotor configuration where inter-spacings are generally smaller. The latter condition leads to higher interaction in between the turbines of single-rotor wind farms, which is seen in general as a more spread added turbulence intensity, I^+, in comparison to the multi-rotor-farm. Additionally, one of the reasons for the multi-rotor-farm to be more efficient is because there are always at least six rotors facing the undisturbed wind due to the MR2 turbine inherent yawing property of simultaneously facing two rotors towards the incoming wind.

It is worth noticing that the total power gain of the multi-rotor layout increases when the space factor, S, is decreased from seven to five. Therefore, the generic multi-rotor wind farms studied layout promises higher energy yields for velocities below rated speed and congested layouts with a small tower-inter-spacing.

7
Conclusion

A set of individual time-averaged wakes of an hypothetical 2R-V29 turbine are resolved by RANS-AD simulations for a range of ambient turbulence intensities, I_∞, and inflow velocities, U_∞, based on a logarithmic inflow profile. Then, for every atmospheric condition, two selected base functions named super- and double-Gaussian were used to approximate the velocity deficit, $\Delta U/U_\infty$, at hub height for each axial position from the turbine. Moreover, the super-Gaussian function was used to approximate the added turbulence intensity, $I^+ = \sqrt{I^2 - I_\infty^2}$, at hub height as a function of the axial position as well. Consequently, look-up tables (LUT) were built with the fitting coefficients of the chosen base functions and the power output of the 2R-V29 turbine, using U_∞ and I_∞ as indexes. This way, either the velocity deficit, $\frac{\Delta U}{U_\infty}\Big|_i$, or the wake added turbulence intensity, I_i^+, on the hub height plane of a 2R-V29 turbine i can be reconstructed by knowing the corresponding freestream conditions seen by the turbine: $U_{\infty,i}$ and $I_{\infty,i}$. The base functions have shown to accurately represent the wake of an individual 2R-V29 turbine for $x > 3D_0$ with greater discrepancies for lower ambient turbulent intensity, I_∞.

Subsequently, a wake superposition method was conceived so as to accurately model of the wake velocity deficit despite over-predicting I^+, since the power output of the turbine is more sensitive to the velocity than to the turbulence intensity. Thus, in order to better estimate the wind turbine efficiency, the accurate modeling of $\Delta U/U_\infty$ is prioritized. This latter mindset leads to a turbulence intensity superposition model $I = I_\infty + \sqrt{\sum_i^N I_{+,i}^2}$ which overestimates the added turbulence intensity if represented as: $I^+ = \sqrt{I^2 - I_\infty^2}$. Hence, suggesting that the representation of I^+ might not be correct, for example: $I^+ = I - I_\infty$ may represent better the added turbulence intensity within the accumulated wake for the chosen turbulence superposition model, but this formulation of I^+ requires further study to address its effects on the velocity deficit. So, while looking for a suitable approximation to represent the merged wakes, it has been found that there is an intrinsic relationship in between the ambient turbulence intensity, I_∞, and the added turbulence intensity of the wakes, I_i^+. Furthermore, the way I^+ is accumulated in a merged wake i.e. by the sum of squares, might not be the same the I_∞ is added i.e. by linear sum, to reconstruct the turbulence intensity field I. Nonetheless, it is clear that the way I^+ is defined will have an effect on how the added turbulence intensity of singular turbines, I_i^+, are superposed in between them in a wind farm scenario.

Once the superposition methods were addressed, the derived surrogate hub height wake model based on analytical functions which coefficients are stored in look-up tables is tested in two different scenarios. First, a layout of four aligned 2R-V29 turbines is studied for a range of turbine inter-spacing, U_∞ and I_∞, where the total wind farm power is estimated with a 94% accuracy for $I_\infty = 5\%$ and 92% accuracy for $I_\infty = 15\%$. The latter is due to an over-estimation of the wake recovery which causes a surplus of output power from the LUT surrogate models in comparison to the power predicted by RANS simulations. Regarding the difference at low I_∞, there is an under-estimation of the wake velocity deficit which increase for lower turbine inter-spacings, thus sighting that the velocity superposition may not be linear in the near wake of the turbine i.e. $x \leq 3D_0$.

Finally, the LUT surrogate models were compared against the RANS model and existing engineering models in a 3×3 2R-V29 turbine layout for different wind directions and two different turbine's inter-spacing $S = 5D_0$ and $S = 7D_0$. The LUT models outcome are in agreement with RANS results, with a maximum wind farm efficiency error of 3% when down-wind turbines are partially shaded by the wake of upstream turbines, thus operating under non-uniform loading conditions. The latter effect is intrinsic to the LUT surrogate models due to the fact that they are based on even analytical functions and trained under a uniform atmospheric surface layer inflow. Thus, in order to correctly represent non-uniform

loading with the chosen analytical functions, these base functions would need more than three degrees of freedom, for example, currently the super-Gaussian function has the following three degrees of freedom: the profile amplitude, the standard deviation and the Gaussian order, but none of them de-centers the profile from the rotors' position. Therefore, it would be interesting to further study how to model and train a new surrogate model able to represent a non-uniform loading.

As a result of the comparison between the LUT surrogate models with the engineering models currently in use in the industry, the derived surrogate models have shown to be an order of magnitude more accurate than both the Park2 and turbo-Gaussian-deficit model while comparing the total wind farm efficiency for different wind speeds and wind directions. Despite being more computational expensive, the surrogate LUT models offer a more accurate prediction of the velocity deficit and thus would improve wind-farm optimization processes oriented toward maximizing the energy yield of a wind farm.

Finally, a layout of 18×V29 turbines and one of 9×2R-V29 turbines within the same wind farm area were RANS-AD modelled. In order to get two comparable cases, a uniform wind probability was chosen and the turbines were located so as to maximize the minimum distance in between each tower. The wind direction average of the specific studied case showed that 5% more energy yield is obtained from the multi-rotor-farm for velocities below rated speed. In general, the multi-rotor wind farm has shown a greater energy yield for velocities below the rated-farm-speed, mainly due to the fact that there are fewer combinations of turbine alignments in a multi-rotor-farm compared to a single-rotor-farm layout with twice as many towers.

7.1. Future work

The present thesis gave an insight of the multi-rotor wake modelling and its complex interaction within wind-farms. This last section will now expand on project sections that can further be studied.

Since the whole 3D wake velocity and turbulence field is available from RANS models, a 3D analytical function can be used to map or fit the wake, in a similar way to what has been done on the 2D hub height plane in the present thesis. Regarding the chosen fitting base function, the more degrees of freedom, the more complex and asymmetric can possibly be the fitted wake. However, this would challenge the fitting algorithm, thus requiring an in depth study of the wake mapping process and maybe foresee the application of machine learning principles.

Regarding the accumulated wake within a wind-farm, further studies can be carried on the observed non-linear superposition of the velocity in the near-wake of multi-rotor turbines, since during this thesis the I^+ superposition method proposed by [Wessel et al., 2007] is implemented to overcome the low wake recovery predicted by the linear velocity superposition for low I_∞. Moreover, additional analysis can be pursued on the interaction of the turbulence intensity added by the turbines with the ambient turbulence intensity, which is closely related to how I^+ is defined.

Finally, the comparison between the multi-rotor and single-rotor wind farms has shown to be highly dependent on the tower layout and wind probability distribution, and hence further study focused on a specific location and wind conditions is required to draw a definitive conclusions.

Bibliography

[Argyle et al., 2018] Argyle, P., Watson, S., Montavon, C., Jones, I., and Smith, M. (2018). Modelling turbulence intensity within a large offshore wind farm. *Wind Energy*, 21(12):1329–1343.

[Bastankhah and Porté-Agel, 2014] Bastankhah, M. and Porté-Agel, F. (2014). A new analytical model for wind-turbine wakes. *Renewable Energy*, 70:116–123.

[Bastankhah et al., 2021] Bastankhah, M., Welch, B. L., Martínez-Tossas, L. A., King, J., and Fleming, P. (2021). Analytical solution for the cumulative wake of wind turbines in wind farms. *Journal of Fluid Mechanics*, 911:A53.

[Baungaard, 2019] Baungaard, M. C. (2019). *Modeling of aerodynamic rotor interaction for multi-rotor wind turbines*. PhD thesis, DTU Wind Energy, Denmark.

[Blondel and Cathelain, 2020] Blondel, F. and Cathelain, M. (2020). An alternative form of the super-gaussian wind turbine wake model. *Wind Energy Science*, 5(3):1225–1236.

[Branch et al., 1999] Branch, M., Coleman, T., and li, Y. (1999). A subspace, interior, and conjugate gradient method for large-scale bound-constrained minimization problems. *SIAM Journal on Scientific Computing*, 21.

[Branlard and Gaunaa, 2015] Branlard, E. and Gaunaa, M. (2015). Cylindrical vortex wake model: right cylinder. *Wind Energy*, 18(11):19731987.

[Chamorro and Porté-Agel, 2009] Chamorro, L. P. and Porté-Agel, F. (2009). A wind-tunnel investigation of wind-turbine wakes: boundary-layer turbulence effects. *Boundary-layer meteorology*, 132:129–149.

[Crespo and Hernandez, 1996] Crespo, A. and Hernandez, J. (1996). Turbulence characteristics in wind-turbine wakes. *Journal of Wind Engineering and Industrial Aerodynamics*, 61(1):71–85.

[Crespo et al., 1999] Crespo, A., Hernández, J., and Frandsen, S. (1999). Survey of modelling methods for wind turbine wakes and wind farms. *Wind Energy*, 2:1–24.

[DTU Wind and Energy Systems, 2023] DTU Wind and Energy Systems (2023). Pywakeellipsys.

[Frandsen, 2007] Frandsen, S. (2007). *Turbulence and turbulence-generated structural loading in wind turbine clusters*. PhD thesis. Risø-R-1188(EN).

[Frandsen et al., 2006] Frandsen, S., Barthelmie, R., Pryor, S., Rathmann, O., Larsen, S., Højstrup, J., and Thøgersen, M. (2006). Analytical modelling of wind speed deficit in large offshore wind farms. *Wind Energy*, 9(1-2):39–53.

[Glauert, 1935] Glauert, H. (1935). *Airplane Propellers*, pages 169–360. Springer Berlin Heidelberg, Berlin, Heidelberg.

[Gunn et al., 2016] Gunn, K., Stock-Williams, C., Burke, M., Willden, R., Vogel, C., Hunter, W., Stallard, T., Robinson, N., and Schmidt, S. (2016). Limitations to the validity of single wake superposition in wind farm yield assessment. In *Journal of Physics: Conference Series*, volume 749, page 012003. IOP Publishing.

[Hansen, 2008] Hansen, M. (2008). *Aerodynamics of Wind Turbines: second edition*. Earthscan, 2 edition.

[IEA, 2022] IEA, I. e. a. (2022). Renewables 2022, analysis and forecast to 2027. *Wind Energy*.

[Ishihara and Qian, 2018] Ishihara, T. and Qian, G. (2018). A new gaussian-based analytical wake model for wind turbines considering ambient turbulence intensities and thrust coefficient effects. *Journal of Wind Engineering and Industrial Aerodynamics*.

[Jensen, 1983] Jensen, N. O. (1983). *Risø-M / 2411, A note on wind generator interaction / [by] N. O. Jensen*.

[Kaimal and Finnigan, 1994] Kaimal, J. C. and Finnigan, J. J. (1994). *Atmospheric boundary layer flows: their structure and measurement*. Oxford university press.

[Katic et al., 1986] Katic, I., Højstrup, J., and Jensen, N. O. (1986). A simple model for cluster efficiency. *PEnergy association conference and exhibition, Rome, Italy*.

[Kermani et al., 2013] Kermani, N., Andersen, S., Sørensen, J., and Shen, W. (2013). Analysis of turbulent wake behind a wind turbine. In Shen, W., editor, *Proceedings of the 2013 International Conference on aerodynamics of Offshore Wind Energy Systems and wakes (ICOWES2013)*. Technical University of Denmark. International Conference on aerodynamics of Offshore Wind Energy Systems and wakes (ICOWES 2013), ICOWES ; Conference date: 17-06-2013 Through 19-06-2013.

[Kundu et al., 2015] Kundu, P. K., Cohen, I. M., and Dowling, D. R. (2015). *Fluid mechanics*. Academic press.

[Leonard, 1979] Leonard, B. (1979). A stable and accurate convective modelling procedure based on quadratic upstream interpolation. *Computer Methods in Applied Mechanics and Engineering*, 19(1):59–98.

[Lingkan and Buxton, 2023] Lingkan, E. H. and Buxton, O. R. (2023). An assessment of the scalings for the streamwise evolution of turbulent quantities in wakes produced by porous objects. *Renewable Energy*, 209:1–9.

[Lissaman, 1979] Lissaman, P. (1979). Energy effectiveness of arbitrary arrays of wind turbines. *Journal of Energy*, 3(6):323–328.

[Loz, 2023] Loz, B. (2023). World's new largest wind turbine. `https://newatlas.com/energy/h260-18mw-biggest-wind-turbine/`. New Atlas, section: Energy.

[Lubachevsky and Graham, 2004] Lubachevsky, B. D. and Graham, R. L. (2004). Minimum perimeter rectangles that enclose congruent non-overlapping circles. *Discret. Math.*, 309:1947–1962.

[Michelsen, 1992] Michelsen, J. A. (1992). Basis3d-a platform for development of multiblock pde solvers. *Report AFM*, 92(876):5.

[Michelsen, 1994] Michelsen, J. A. (1994). *Block structured Multigrid solution of 2D and 3D elliptic PDE's*. Department of Fluid Mechanics, Technical University of Denmark.

[Niayifar and Porté-Agel, 2016] Niayifar, A. and Porté-Agel, F. (2016). Analytical Modeling of Wind Farms: A New Approach for Power Prediction. *Energies*, 9(9):741.

[Nygaard et al., 2020] Nygaard, N. G., Steen, S. T., Poulsen, L., and Pedersen, J. G. (2020). Modelling cluster wakes and wind farm blockage. *Journal of Physics: Conference Series*, 1618(6):062072.

[Patankar, 1980] Patankar, S. (1980). Numerical heat transfer and fluid flow. *International Journal of Heat and Mass Transfer*.

[Peric, 1985] Peric, M. (1985). A finite volume method for the prediction of three-dimensional fluid flow in complex ducts. Ph. D. thesis, University of London.

[Pope, 2000] Pope, S. B. (2000). *Turbulent Flows*. Cambridge University Press.

[Rathmann et al., 2018] Rathmann, O., Hansen, B., Hansen, K., Mortensen, N., and Murcia Leon, J. (2018). *The Park2 Wake Model - Documentation and Validation*. DTU Wind Energy E.

[Réthoré et al., 2014] Réthoré, P.-E., Laan, van der, P., Troldborg, N., Zahle, F., and Sørensen, N. (2014). Verification and validation of an actuator disc model. *Wind Energy*, 17(6):919937.

[Réthoré and Sørensen, 2012] Réthoré, P.-E. and Sørensen, N. (2012). A discrete force allocation algorithm for modelling wind turbines in computational fluid dynamics. *Wind Energy*, 15(7):915–926.

[Richardson, 1911] Richardson, L. F. (1911). Ix. the approximate arithmetical solution by finite differences of physical problems involving differential equations, with an application to the stresses in a masonry dam. *Philosophical Transactions of the Royal Society of London. Series A, Containing Papers of a Mathematical or Physical Character*, 210(459-470):307–357.

[Satyam and Bin-Khalid, 2019] Satyam, S. and Bin-Khalid, U. (2019). Pollutant dispersion analysis on an urban square using sand erosion technique.

[Sørensen, 1995] Sørensen, N. N. (1995). General purpose flow solver applied to flow over hills. Ph. D. thesis at DTU.

[Stein and Kaltenbach, 2019] Stein, V. P. and Kaltenbach, H.-J. (2019). Non-equilibrium scaling applied to the wake evolution of a model scale wind turbine. *Energies*, 12(14).

[Sumer and Fuhrman, 2020] Sumer, B. M. and Fuhrman, D. R. (2020). *Turbulence in coastal and civil engineering*, volume 51. World Scientific.

[Sumner and Masson, 2012] Sumner, J. and Masson, C. (2012). k- ε simulations of the neutral atmospheric boundary layer: analysis and correction of discretization errors on practical grids. *International journal for numerical methods in fluids*, 70(6):724–741.

[Sørensen et al., 2007] Sørensen, N. N., Bechmann, A., Johansen, J., Myllerup, L., Botha, P., Vinther, S., and Nielsen, B. S. (2007). Identification of severe wind conditions using a reynolds averaged navier-stokes solver. *Journal of Physics: Conference Series*, 75(1):012053.

[Troldborg et al., 2015] Troldborg, N., Sørensen, N., Réthoré, P.-E., and van der Laan, M. (2015). A consistent method for finite volume discretization of body forces on collocated grids applied to flow through an actuator disk. *Computers & Fluids*, 119:197–203.

[van der Laan and Abkar, 2019] van der Laan, M. and Abkar, M. (2019). Improved energy production of multi-rotor wind farms. *Journal of Physics: Conference Series*, 1256(1):012011.

[van der Laan et al., 2020] van der Laan, M., Andersen, S., Kelly, M., and Baungaard, M. (2020). Fluid scaling laws of idealized wind farm simulations. volume 1618. IOP Publishing. TORQUE 2020 ; Conference date: 28-09-2020 Through 02-10-2020.

[van der Laan et al., 2019] van der Laan, M. P., Andersen, S. J., Ramos García, N., Angelou, N., Pirrung, G. R., Ott, S., Sjöholm, M., Sørensen, K. H., Vianna Neto, J. X., Kelly, M., Mikkelsen, T. K., and Larsen, G. C. (2019). Power curve and wake analyses of the Vestas multi-rotor demonstrator. *Wind Energy Science*, 4(2):251–271.

[van der Laan et al., 2022] van der Laan, M. P., Andersen, S. J., Réthoré, P.-E., Baungaard, M., Sørensen, J. N., and Troldborg, N. (2022). Faster wind farm aep calculations with cfd using a generalized wind turbine model. *Journal of Physics: Conference Series*, 2265(2):022030.

[van der Laan et al., 2021] van der Laan, M. P., Baungaard, M., and Kelly, M. (2021). Inflow modeling for wind farm flows in rans. volume 1934. IOP Publishing. Wake Conference 2021 ; Conference date: 15-06-2021 Through 17-06-2021.

[van der Laan and Sørensen, 2017] van der Laan, M. P. and Sørensen, N. N. (2017). A 1d version of ellipsys. *DTU Wind Energy E-0141, Technical University of Denmark*.

[van der Lann et al., 2015] van der Lann, P. M., Sørensen, N. N., Réthoré, P.-E., Mann, J., Kelly, M. C., Troldborg, N., Schepers, J. G., and Machefaux, E. (2015). An improved k- model applied to a wind turbine wake in atmospheric turbulence. *Wind Energy*, 18(5):889907.

[Verma, 2014] Verma, P. (2014). Multi Rotor Wind Turbine Design And Cost Scaling. *University of Massachusetts Amherst*.

[Voutsinas et al., 1990] Voutsinas, S., Rados, K., and Zervos, A. (1990). On the analysis of wake effects in wind parks. *Wind Engineering*, pages 204–219.

[Wessel et al., 2007] Wessel, A., Peinke, J., and Lange, B. (2007). Modelling turbulence intensities inside wind farms. In Peinke, J., Schaumann, P., and Barth, S., editors, *Wind Energy*, pages 253–257, Berlin, Heidelberg. Springer Berlin Heidelberg.

A

Test-run with a single Vestas 4R-V29

The present section is used as a test-run to learn how to use *PyWakeEllipsys* [DTU Wind and Energy Systems, 2023] and cross-check the CFD results with the reference RANS-AD [van der Laan et al., 2019].

The inlet conditions correspond to a neutral ASL explained in section 2.2 with the following parameters:

- $U_\infty = 11.5$ m/s at z_{ref}
- $I_\infty = 8.4$ % at z_{ref}
- $z_{\text{ref}} = \frac{z_{\text{hub, 1}} + z_{\text{hub, 2}}}{2} = 44.27$ m

The simulation of this section has been run with the mesh described in subsection 2.7.2 and the AD airfoil calibration force method explained in section 2.6. Just like the reference simulation settings, the AD has been discretized with $N_{CD} = D_0/\Delta_1 = 20$ cells within one V29 rotor diameter.

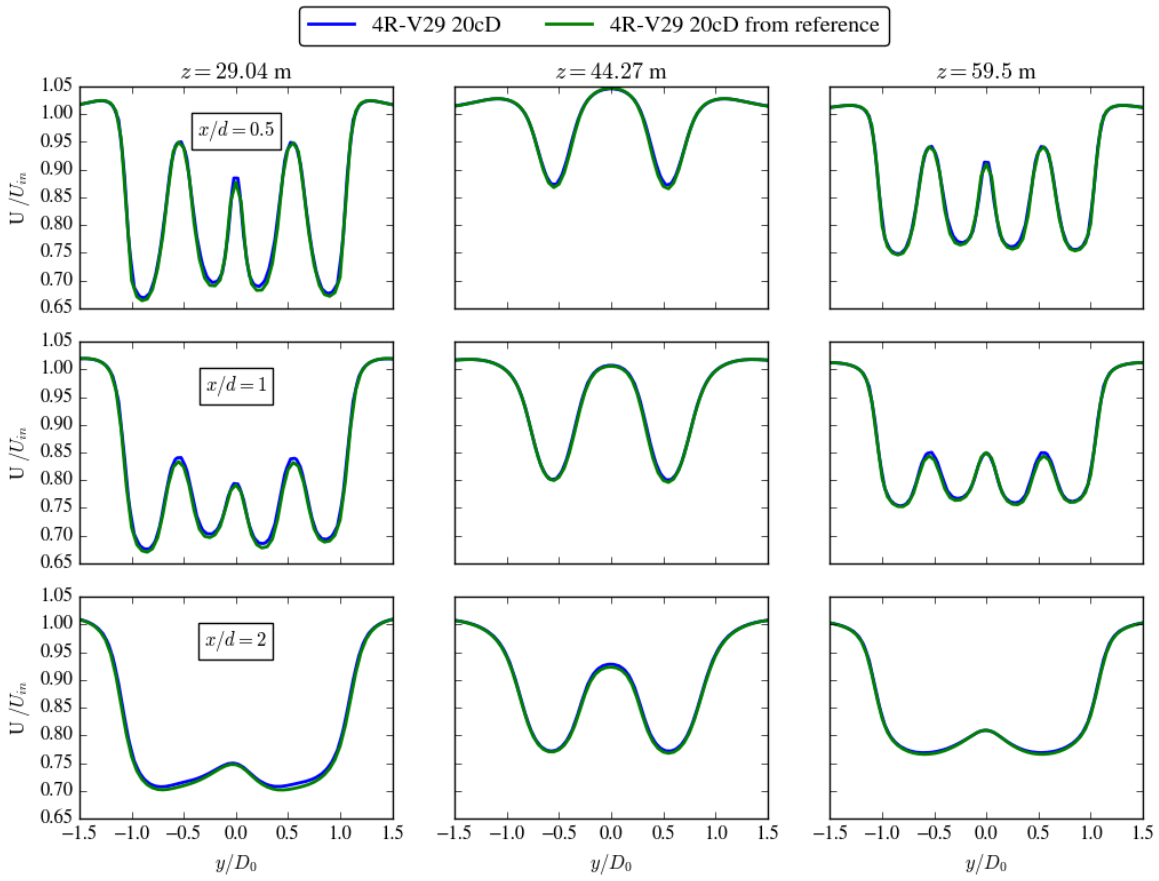

Figure A.1: profiles of stream-wise velocity at three heights and three downstream distances compared to RANS-AD results from [van der Laan et al., 2019].

Regarding the results, the wake velocity profile normalized with the corresponding U_∞ according to the atmospheric surface layer (ASL) is shown in Figure A.1, where the maximum difference with the reference simulation is of 2.8%. Moreover, Figure A.2 shows the turbulence intensity profile with 2.4% maximum discrepancy with the results from [van der Laan et al., 2019].

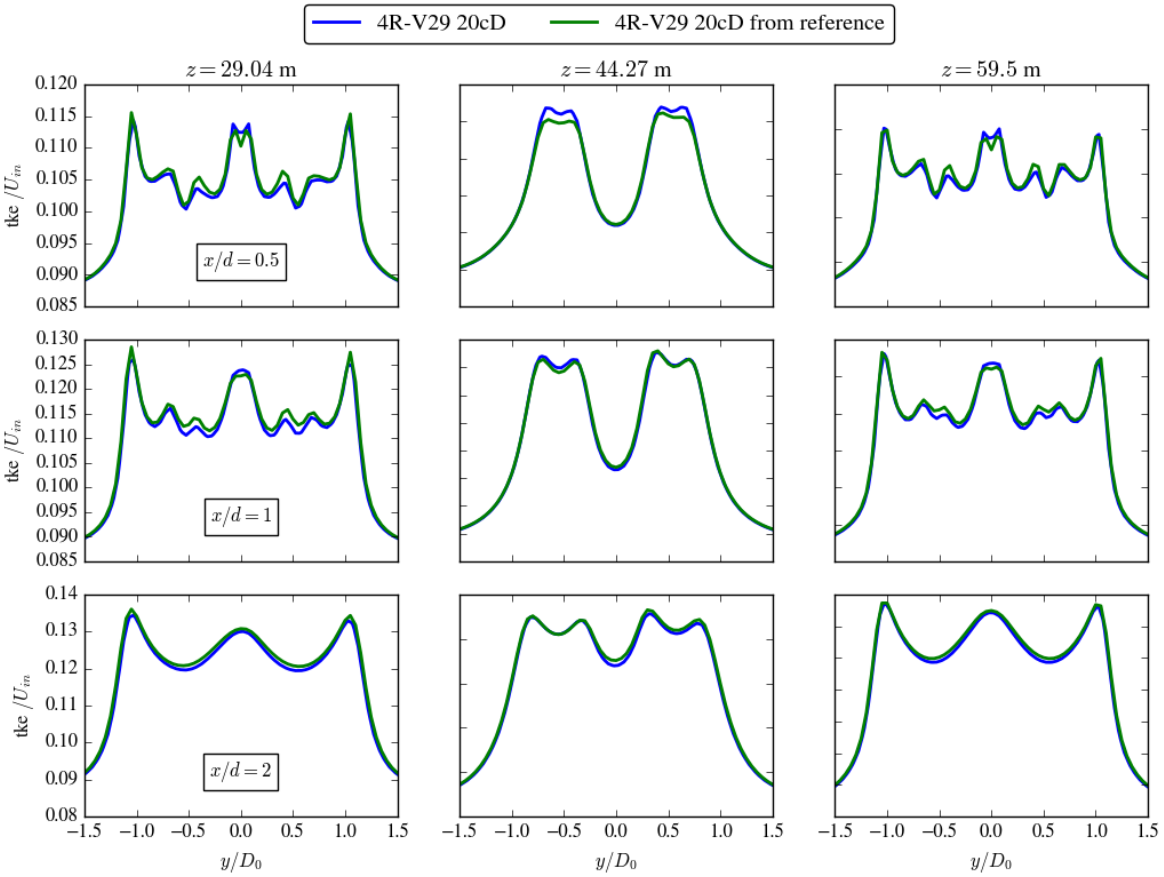

Figure A.2: profiles of stream-wise turbulence intensity at three heights and three downstream distances compared to RANS results from [van der Laan et al., 2019].

Being that the difference with the reference paper are lower than 3%, the *PyWakeEllipSys* workflow is then considered valid to pursue further RANS-AD simulations of multi-rotor-two (MR2) wind turbines. It is believed that the discrepancies are due to a change in the implementation of the airfoil loading within EllipSys. Nonetheless, further investigation with *PyWakeEllipSys v0.1* (released on May 2019) is required in order to confirm the latter statement.

B

2R-V29 wake model

The current appendix presents the algorithm used to generate the look-up tables and compares some wakes derived by RANS simulations and the conceived surrogate models.

B.1. Algorithm used to build the look-up tables $\Psi(I_\infty, U_\infty, \hat{x})$

As a summary of the present section, every step realized to store the base function coefficients in look-up tables $\Psi(I_\infty, U_\infty, \hat{x})$ is stated in algorithm 2.

Algorithm 2: Algorithm to generate the look-up tables of the surrogate wake model.

input : MR2 turbine airfoil data and geometrical specifications.
output: $\Psi(I_\infty, U_\infty, \hat{x})$: look up tables of the base function coefficients for the velocity deficit, $\Delta U/U_\infty$, and added turbulence intensity, I^+, as a function of the relative position $\hat{x}$ and wind inflow conditions (U_∞ and I_∞ at z_h).

for I_∞ *in* $[5, 10, 15, 20, 30]\%$ **do**
  for U_∞ *in* $[4, 5, 6, 7, 8, 10, 13, 16]$ m/s **do**
    RUN: RANS-AD simulation of a single MR2 turbine in EllipSys3D;
    Sample the hub height field;
    Compute the velocity deficit $\Delta U/U_\infty = \frac{U_\infty - U}{U_\infty}$;
    Compute the added turbulence intensity $I^+ = \sqrt{I^2 - I_\infty^2}$;
    Fit either the super-Gaussian or double-Gaussian base function to the velocity deficit $\frac{\Delta U}{U_\infty}$ for each axial position ($\hat{x}$) and save the fitted coefficients in a look-up table $\Psi(\hat{x}, U_\infty, I_\infty)$ as a function of: $\hat{x}$, U_∞ and I_∞.;
    Fit the super-Gaussian base function to the added turbulence intensity I^+ for each axial position ($\hat{x}$) and save the fitted coefficients in a look-up table $\Psi(\hat{x}, U_\infty, I_\infty)$.;
    Save the output power of the MR2 turbine in a look-up table $\Psi(U_\infty, I_\infty)$.;
  end
end

B.2. Surrogate model compared to RANS model on a single 2R-V29 turbine

The following two functions are used to model the wake profile for each given axial position, $\hat{x}$, ambient turbulent intensity, I_∞, and inflow speed, U_∞ at hub height:

Super Gaussian

$$\frac{\Delta U}{U_\infty} = C \times \exp\left(-\frac{1}{2}\frac{\hat{y}^n}{\sigma^2}\right), \tag{B.1}$$

Double Gaussian

$$\frac{\Delta U}{U_\infty} = C \times \left(\exp\left(-\frac{1}{2}\frac{(\hat{y} - n \text{ arm}/D_0)^2}{\sigma^2}\right) + \exp\left(-\frac{1}{2}\frac{(\hat{y} + n \text{ arm}/D_0)^2}{\sigma^2}\right)\right), \tag{B.2}$$

where the arm/D_0 variable is the normalized distance from the MR2 centroid to the rotors' axis and C, σ and n are function coefficients that are fitted for each $\hat{x}$ position using the Trust Region Reflective non-linear least squares algorithm [Branch et al., 1999] built in the python library *scipy.optimize.curve_fit*. The outcome of the latter fitting process of the velocity deficit, $\Delta U/U_\infty$, is illustrated at three downstream positions in Figure B.1. Furthermore, the coefficients of the super-Gaussian function that fits $\Delta U/U_\infty$ are stated in Table B.1, and the coefficients of the double-Gaussian function in Table B.2.

The super-Gaussian base function is also used to fit the added turbulence intensity, I^+, which is illustrated at three downstream positions in Figure B.2. Moreover, the latter function coefficients used are stated in Table B.3.

It is seen that all studied surrogate functions tend to a second order Gaussian in the far wake. The super-Gaussian order tends to two, and the double-Gaussian $\hat{y}$ shift tends to zero, thus merging both Gaussians.

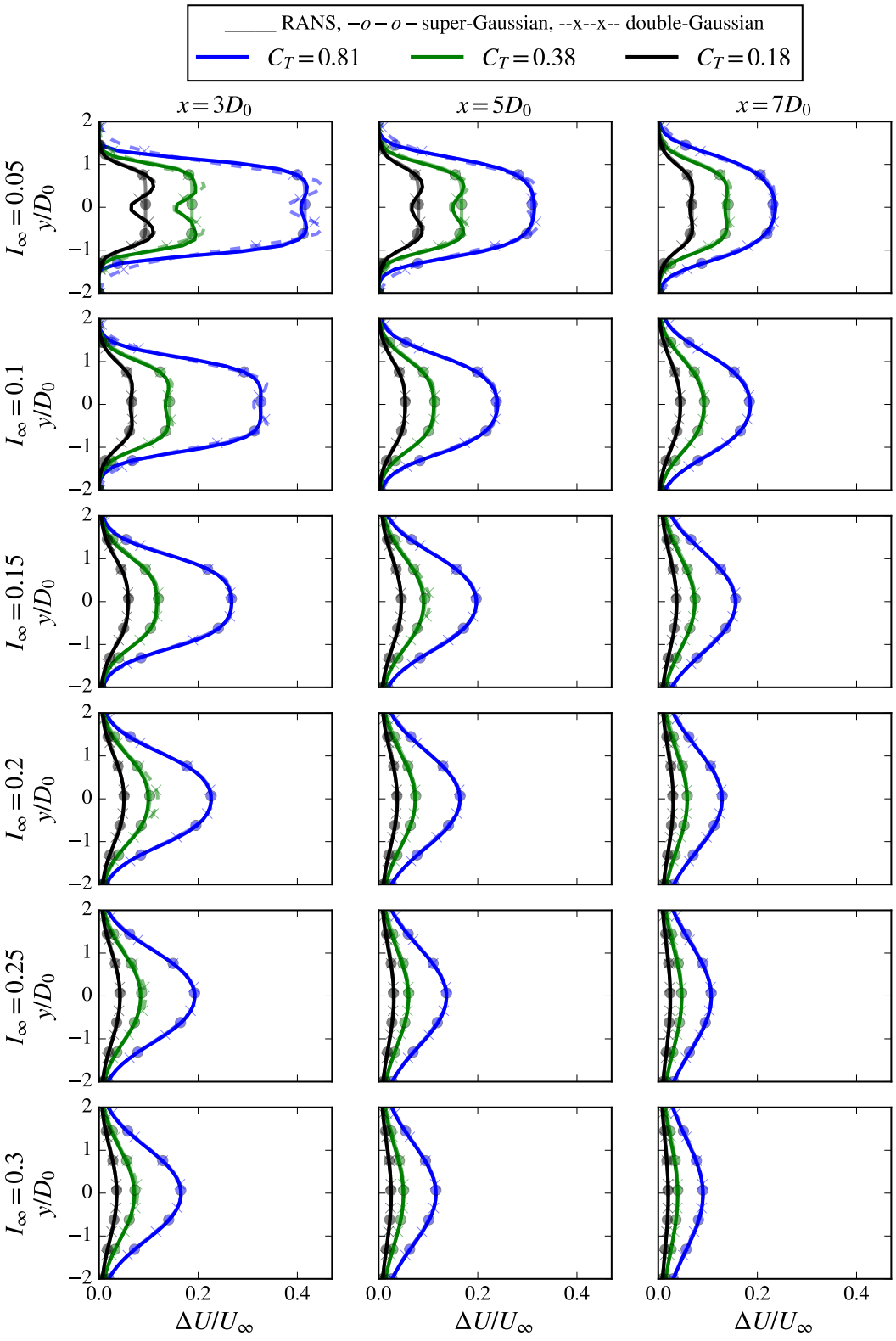

Figure B.1: velocity deficit, $\Delta U/U_\infty$, of the 2R-V29 turbine sampled at three different downstream positions for the RANS simulation and both the super-Gaussian and double-Gaussian models.

Table B.1: super-Gaussian function coefficients: C, σ and n that fit the velocity deficit, $\Delta U/U_\infty$, as a function of $\hat{x}$, U_∞ and I_∞.

I_∞ [%]	U_∞ [m/s] (C_T [-])	$x = 3D_0$			$x = 5D_0$			$x = 7D_0$		
		C	σ	n	C	σ	n	C	σ	n
5	8 m/s ($C_T = 0.81$)	0.42	1.27	7.58	0.31	1.17	4.87	0.23	1.21	3.86
	13 m/s ($C_T = 0.36$)	0.19	1.08	9.29	0.17	1.03	6.44	0.14	1.03	4.79
	16 m/s ($C_T = 0.18$)	0.09	0.87	8.6	0.08	0.94	6.25	0.07	0.97	4.56
10	8 m/s ($C_T = 0.81$)	0.33	1.08	4.87	0.24	1.07	3.26	0.18	1.13	2.75
	13 m/s ($C_T = 0.36$)	0.14	0.99	4.61	0.11	0.97	3.07	0.09	0.99	2.55
	16 m/s ($C_T = 0.18$)	0.07	0.95	4.11	0.05	0.95	2.86	0.04	0.97	2.44
15	8 m/s ($C_T = 0.81$)	0.27	1.02	3.21	0.2	1.06	2.41	0.16	1.13	2.16
	13 m/s ($C_T = 0.36$)	0.12	0.97	2.74	0.09	1.0	2.09	0.07	1.1	2.0
	16 m/s ($C_T = 0.18$)	0.06	0.96	2.31	0.05	1.05	2.0	0.04	1.2	2.0
20	8 m/s ($C_T = 0.81$)	0.23	1.01	2.56	0.16	1.08	2.12	0.13	1.19	2.0
	13 m/s ($C_T = 0.36$)	0.1	0.97	2.18	0.07	1.1	2.0	0.06	1.26	2.0
	16 m/s ($C_T = 0.18$)	0.05	1.01	2.0	0.04	1.21	2.0	0.03	1.41	2.0
25	8 m/s ($C_T = 0.81$)	0.19	1.02	2.31	0.14	1.13	2.05	0.11	1.27	2.0
	13 m/s ($C_T = 0.36$)	0.09	1.0	2.07	0.06	1.17	2.0	0.05	1.35	2.0
	16 m/s ($C_T = 0.18$)	0.04	1.05	2.0	0.03	1.28	2.0	0.02	1.49	2.0
30	8 m/s ($C_T = 0.81$)	0.17	1.04	2.22	0.12	1.19	2.03	0.09	1.35	2.0
	13 m/s ($C_T = 0.36$)	0.07	1.03	2.05	0.05	1.23	2.0	0.04	1.42	2.0
	16 m/s ($C_T = 0.18$)	0.04	1.08	2.0	0.02	1.33	2.0	0.02	1.55	2.0

Table B.2: double-Gaussian function coefficients: C, σ and n that fit the velocity deficit, $\Delta U/U_\infty$, as a function of $\hat{x}$, U_∞ and I_∞.

I_∞ [%]	U_∞ [m/s] (C_T [-])	$x = 3D_0$			$x = 5D_0$			$x = 7D_0$		
		C	σ	n	C	σ	n	C	σ	n
5	8 m/s ($C_T = 0.81$)	0.43	0.43	1.08	0.3	0.48	1.09	0.21	0.54	1.14
	13 m/s ($C_T = 0.36$)	0.21	0.38	1.06	0.18	0.4	1.05	0.14	0.45	1.05
	16 m/s ($C_T = 0.18$)	0.11	0.34	1.05	0.09	0.38	1.04	0.07	0.43	1.04
10	8 m/s ($C_T = 0.81$)	0.32	0.46	1.06	0.2	0.55	1.1	0.14	0.65	1.17
	13 m/s ($C_T = 0.36$)	0.14	0.44	1.04	0.09	0.53	1.05	0.07	0.63	1.07
	16 m/s ($C_T = 0.18$)	0.06	0.44	1.03	0.04	0.55	1.03	0.03	0.65	1.04
15	8 m/s ($C_T = 0.81$)	0.23	0.54	1.08	0.14	0.7	1.12	0.1	0.88	1.11
	13 m/s ($C_T = 0.36$)	0.09	0.57	1.06	0.05	0.89	0.51	0.04	1.1	0.01
	16 m/s ($C_T = 0.18$)	0.04	0.66	1.04	0.02	1.05	0.01	0.02	1.2	0.01
20	8 m/s ($C_T = 0.81$)	0.17	0.63	1.08	0.1	0.88	1.02	0.06	1.19	0.02
	13 m/s ($C_T = 0.36$)	0.06	0.82	0.53	0.04	1.1	0.02	0.03	1.26	0.01
	16 m/s ($C_T = 0.18$)	0.03	1.01	0.01	0.02	1.21	0.01	0.01	1.41	0.02
25	8 m/s ($C_T = 0.81$)	0.13	0.72	1.07	0.08	1.01	0.86	0.05	1.27	0.02
	13 m/s ($C_T = 0.36$)	0.05	0.9	0.49	0.03	1.17	0.01	0.02	1.35	0.02
	16 m/s ($C_T = 0.18$)	0.02	1.05	0.01	0.02	1.28	0.01	0.01	1.49	0.02
30	8 m/s ($C_T = 0.81$)	0.11	0.78	1.06	0.06	1.07	0.88	0.05	1.35	0.02
	13 m/s ($C_T = 0.36$)	0.04	0.95	0.47	0.03	1.23	0.02	0.02	1.42	0.02
	16 m/s ($C_T = 0.18$)	0.02	1.08	0.02	0.01	1.33	0.01	0.01	1.55	0.02

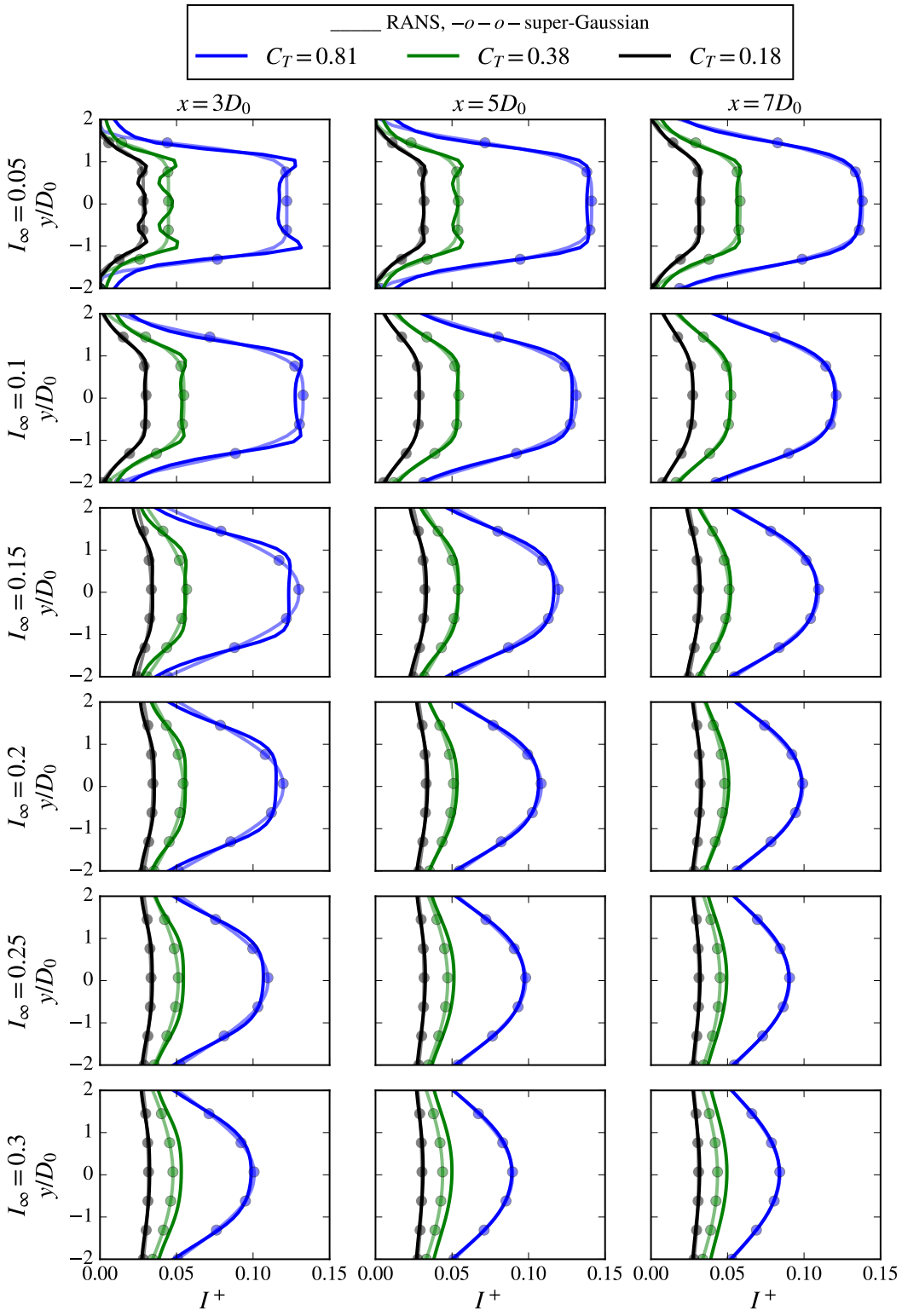

Figure B.2: added turbulence intensity, $I^+ = \sqrt{I^2 - I_\infty^2}$, of the 2R-V29 turbine sampled at three different downstream positions for the RANS simulation and the super-Gaussian model for I^+.

Table B.3: super-Gaussian function coefficients: C, σ and n that fit the **added turbulence intensity**, $\mathbf{I}^+$, as a function of $\hat{x}$, U_∞ and I_∞.

I_∞ [%]	U_∞ [m/s] (C_T [-])	$x = 3D_0$			$x = 5D_0$			$x = 7D_0$		
		C	σ	n	C	σ	n	C	σ	n
5	8 m/s ($C_T = 0.81$)	0.12	3.01	7.88	0.14	2.27	5.26	0.14	2.16	4.22
	13 m/s ($C_T = 0.36$)	0.04	2.69	7.59	0.05	2.26	5.81	0.06	2.03	4.69
	16 m/s ($C_T = 0.18$)	0.03	1.96	6.8	0.03	1.84	5.34	0.03	1.85	4.61
10	8 m/s ($C_T = 0.81$)	0.13	1.95	4.16	0.13	1.86	3.3	0.12	1.94	2.99
	13 m/s ($C_T = 0.36$)	0.05	2.01	4.3	0.05	1.97	3.57	0.05	1.95	3.14
	16 m/s ($C_T = 0.18$)	0.03	1.92	4.4	0.03	1.95	3.7	0.03	1.94	3.27
15	8 m/s ($C_T = 0.81$)	0.13	1.56	2.4	0.12	1.71	2.32	0.11	1.85	2.26
	13 m/s ($C_T = 0.36$)	0.06	1.81	2.0	0.05	1.94	2.0	0.05	2.09	2.0
	16 m/s ($C_T = 0.18$)	0.03	2.51	2.0	0.03	2.72	2.0	0.03	2.94	2.0
20	8 m/s ($C_T = 0.81$)	0.12	1.63	2.17	0.11	1.79	2.14	0.1	1.93	2.09
	13 m/s ($C_T = 0.36$)	0.05	2.15	2.0	0.05	2.33	2.0	0.05	2.52	2.0
	16 m/s ($C_T = 0.18$)	0.03	3.23	2.0	0.03	3.55	2.0	0.03	3.87	2.0
25	8 m/s ($C_T = 0.81$)	0.11	1.71	2.12	0.1	1.88	2.09	0.09	2.0	2.03
	13 m/s ($C_T = 0.36$)	0.05	2.33	2.0	0.05	2.54	2.0	0.05	2.71	2.0
	16 m/s ($C_T = 0.18$)	0.03	3.68	2.0	0.03	4.1	2.0	0.03	4.31	2.0
30	8 m/s ($C_T = 0.81$)	0.1	1.77	2.1	0.09	1.94	2.07	0.08	2.07	2.0
	13 m/s ($C_T = 0.36$)	0.05	2.47	2.0	0.04	2.68	2.0	0.04	2.81	2.0
	16 m/s ($C_T = 0.18$)	0.03	4.16	2.0	0.03	4.56	2.0	0.03	4.44	2.0

C

Wake superposition model

The present chapter is structured as follows: section C.1 compares different $U_{\infty,i}$ and $I_{\infty,i}$ sampling methods, which are used to map the freestream velocity and turbulence intensity seen by the i^{th} MR2 turbine, and later used to access the look-up table i.e. $\Psi(U_{\infty,i}, I_{\infty,i})$. Finally, section C.2 and section C.3 evaluate different turbulence intensity and velocity superposition methods, respectively. The complete superposition model is depicted in algorithm 1 and the final model is tested in section 4.2.

C.1. Computing $I_{\infty,i}$ and $U_{\infty,i}$ from the $z = z_h$ plane

Since the analytical wake model has been developed for the hub height (z_h) horizontal plane, we then need a form of representing the freestream wind conditions seen by the i^{th} turbine: $U_{\infty,i}$ and $I_{\infty,i}$, by using information from the $z = z_h$ plane exclusively. Thus, different methods are compared with RANS simulations and the mean square error (MSE) in between the studied methods and the higher fidelity RANS simulations is computed.

C.1.1. Computing $I_{\infty,i}$

This section answers how to compute the freestream turbulence intensity seen by the i^{th} turbine, $I_{\infty,i}$, by evaluating the following three methods:

Method A. $I_{\infty,i} = \langle I \rangle_{\mathrm{AD},z_h,i}$, computing the averaged turbulence intensity of the two segments that result from the intersection of both actuator disks (AD) of the MR2 turbine with the hub height plane $z = z_h$.

Method B. $I_{\infty,i} = I\big|_{\mathrm{MR\ centroid},i}$, hence the turbulence intensity of the multi-rotor centroid represents the turbulence intensity of the whole turbine.

Method C. $I_{\infty,i} = I_{\infty}$ directly taken from the inflow condition. Thus, all the turbines are subjected to the same ambient hub height turbulence intensity, I_{∞}.

All three methods are tested under the same conditions specified in Table C.1, were the velocity deficit, $[\Delta U/U_{\infty,i}]$, and the added turbulence intensity, I_i^+, of each turbine are taken from the look-up tables generated in chapter 3, using as index:

- $U_{\infty,i} = \langle U \rangle_{\mathrm{AD},z_h,i}$, the average velocity of the two segments resulting from the intersection of both actuator disks (AD) with the hub height plane ($z = z_h$) sampled at the location of the i^{th} turbine.
- $I_{\infty,i}$ defined by the tested method

Table C.1: analytical surrogate model setup to test different turbine freestream turbulence intensity, $I_{\infty,i}$, sampling methods. N is the total amount of MR2 turbines.

$I_{\infty,i}$ sampling method	Method A $I_{\infty,i} = \langle I \rangle_{\mathrm{AD},z_h,i}$	Method B $I_{\infty,i} = I\big\vert_{\mathrm{MR\ centroid},i}$	Method C $I_{\infty,i} = I_\infty$
$U_{\infty,i}$ sampling method	$\langle U \rangle_{\mathrm{AD},z_h,i}$		
Tower inter-spacing	$7D_0$		
U_∞ [m/s]	$[8, 10, 13, 16]$		
I_∞ [%]	$[5, 10, 15]$		
I^+ superposition method	$I^+ = \sqrt{\sum_{i=1}^{N} I_{+,i}^2}$		
$\Delta U/U_\infty$ superposition method	$\Delta U/U_\infty = \sum_{i=1}^{N} \left[\frac{\Delta U}{U_{\infty,i}}\right] \frac{U_{\infty,i}}{U_\infty}$		

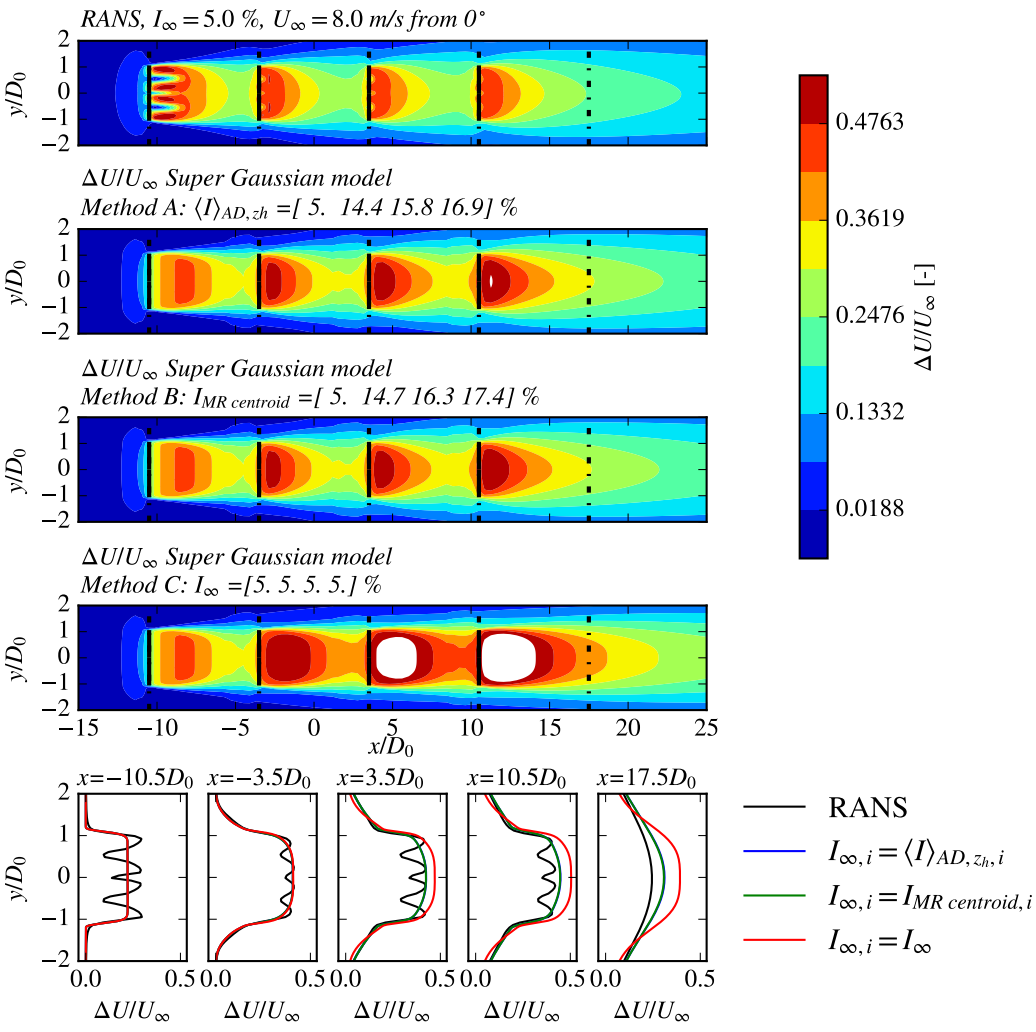

Figure C.1: hub height velocity deficit of 4 turbines distanced $7D_0$ from each other and subjected to $U_\infty = 8$ m/s and $I_\infty = 5\%$. The first row is RANS modelled and the second, third and fourth are obtained through the LUT model using different representations of $I_{\infty,i}$. The white colouring means that the velocity deficit is out of the colour-bar scale.

Figure C.1 shows the computed wake of the super-Gaussian model compared to the RANS-AD simulation for $U_\infty = 8$ m/s and $I_\infty = 5\%$. As observed in the second contour plot, assuming that every turbine operates in a free-stream flow of constant turbulence intensity $I_{\infty,i} = I_\infty$ leads to a sub-estimation of the actual turbulence intensity and thus to slower wake recoveries which is seen as higher velocity deficits. Method A and B account for a more turbulent wake since they use the in-situ turbulence intensity, com-

pared to method C, which supposes that all the turbines operate at I_∞, see Figure C.1. It is then observed that higher turbulence intensity sensed at the turbine location triggers a faster wake recovery and thus a lower $\Delta U/U_\infty$ if the turbulence intensity is sampled with method A or B rather than method C.

In order to compare which method is best in the whole range of U_∞ and I_∞ studied, the mean square error of the velocity deficit obtained by the three studied methods is computed against the RANS velocity deficit for the domain observed in Figure C.1 ($-15 < x/D < 25$, $-2 < y < 2$ on the $z = z_h$ plane):

$$\mathrm{MSE}(\Delta U/U_\infty) = \frac{1}{40D}\int_{-15D}^{25D}\frac{1}{4D}\int_{-2D}^{2D}\left[\frac{\Delta U}{U_\infty}\Big|_{\mathrm{RANS}} - \frac{\Delta U}{U_\infty}\Big|_{\mathrm{Model}}\right]^2_{(x,y,z_h)} dy\,dx, \tag{C.1}$$

where D is equivalent to the diameter of a single V29 rotor, D_0.

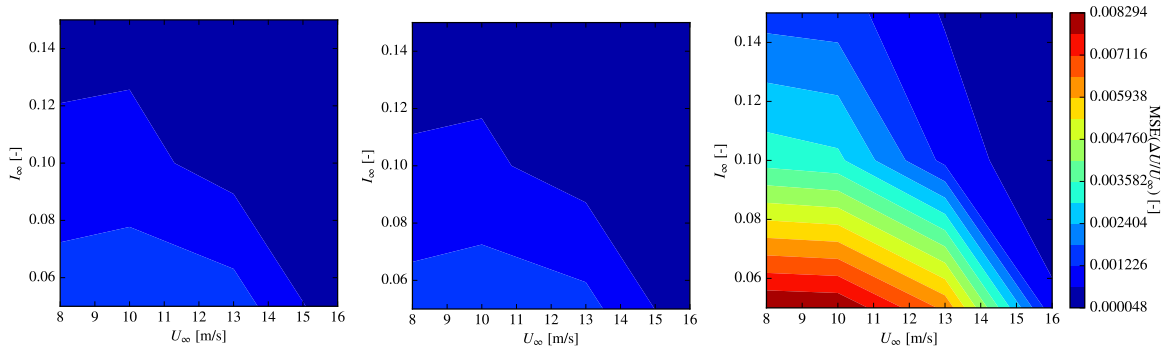

(a) Method A: $I_{\infty,i} = \langle I \rangle_{\mathrm{AD},z_h,i}$ **(b)** Method B: $I_{\infty,i} = I|_{\mathrm{centroid},i}$ **(c)** Method C: $I_{\infty,i} = I_\infty$

Figure C.2: mean square error (MSE) of the velocity deficit, $\Delta U/U_\infty$, of the super-Gaussian LUT surrogate model with three different representations of $I_{\infty,i}$, compared with the higher fidelity RANS simulation at the hub height plane, $z = z_{\mathrm{hub}}$, for $-15 < x/D < 25$ and $-2 < y/D < 2$.

The main difference in between the studied methods takes place at high loading (high C_T, thus low U_∞) and low ambient turbulence intensity, I_∞. Furthermore, there is no significant MSE difference in between sampling a single point at the multi-rotor centroid (method B) or computing $\langle U \rangle_{\mathrm{AD},z_h}$ (method A).

As a conclusion, due to its dependence on multiple points, $I_{\infty,i} = \langle U \rangle_{\mathrm{AD},z_h,i}$ (method A) is chosen as representative of the turbulence intensity felt by the whole turbine. It is in fact preferred to compute $I_{\infty,i}$ as an average of values instead of depending on a single sampling point.

C.1.2. Computing $U_{\infty,i}$

Based on the previous study, the freestream velocity seen by the i^{th} turbine ($U_{\infty,i}$), that will then be used to access the wake look-up table, is computed as the velocity average of both segments that result from intersecting the two actuator disks (AD) of the MR2 turbine with the hub height plane ($z = z_h$), i.e. $U_{\infty,i} = \langle U \rangle_{\mathrm{AD},z_h,i}$.

C.2. I^+ superposition model

In chapter 3 the velocity deficit, $\Delta U/U_\infty$, and the added turbulence intensity, $I^+ = \sqrt{I^2 - I_\infty^2}$, of the flow around a single turbine were saved in look up tables $\Psi(U_\infty, I_\infty)$ as a function of the freestream velocity, U_∞, and freestream turbulence intensity, I_∞, at hub height for all the fitted axial positions. By representing the freestream wind conditions with both $U_{\infty,i} = \langle U \rangle_{\mathrm{AD},z_h,i}$ and $I_{\infty,i} = \langle I \rangle_{\mathrm{AD},z_h,i}$, it is now possible to access the wake look-up table of any i^{th} 2R-V29 turbine of a wind farm as: $\Psi\left(U_{\infty,i}, I_{\infty,i}\right)$ and obtain[1] the power, P_i, the velocity deficit, $\frac{\Delta U}{U_{\infty,i}}$, and added turbulence intensity, $I_{+,i}$. Do note that the freestream wind conditions felt by a single MR2 turbine ($i = 1$) are still equivalent to the ambient wind conditions at hub height i.e. $U_{\infty,1} = U_\infty$ and $I_{\infty,1} = I_\infty$.

The present section evaluates the following three wake added turbulence intensity superposition models:

[1]The teal colored variables refer to variables obtained from Ψ.

Method A. Taking into account the added turbulence intensity, I_i^+, generated by the directly upstream turbine i only:

$$I^+ = I_i^+.$$

Method B. Quadratic sum of the I^+ of all the N upstream turbines by the method proposed by [Lingkan and Buxton, 2023]:

$$I^+ = \sqrt{\sum_{i=1}^{N} I_{+,i}^2}.$$

Method C. Superposing the I^+ of all the N upstream turbines by the method proposed by [Wessel et al., 2007]:

$$I = I_\infty + \sqrt{\sum_{i=1}^{N} I_{+,i}^2} \rightarrow I^+ = \sqrt{I^2 - I_\infty^2}.$$

The evaluated methods were proposed based on empiricism, thus lacking a theoretical background. By applying $\sqrt{\sum_{i=1}^{N} I_{+,i}^2}$, both methods **B** and **C** are summing the turbulent kinetic energy in between the wind turbines wakes. The difference lies in the fact that method **B** sums I_∞^2 to I_+^2, while method **C** linearly sums I_∞ to $\sqrt{\sum_{i=1}^{N} I_{+,i}^2}$ in order to compute I.

Four MR2 turbines spaced $7D_0$ are modelled with three different I^+ superposition models and compared to higher fidelity models (RANS-AD). The used parameters are detailed in Table C.2 where both I_i^+ and $[\Delta U/U_{\infty,i}]$ are obtained from the look-up tables of the super-Gaussian surrogate model fitted in chapter 3.

Table C.2: analytical surrogate model setup to test different I_i^+ superposition models. N is the total amount of rotors

I^+ superposition method	Model A I_i^+	Model B $\sqrt{\sum_{i=1}^{N} I_{+,i}^2}$	Model C $I = I_\infty + \sqrt{\sum_{i=1}^{N} I_{+,i}^2}$ $I^+ = \sqrt{I^2 - I_\infty^2}$
$U_{\infty,i}$ sampling method	$\langle U \rangle_{\mathrm{AD},z_h,i}$		
$I_{\infty,i}$ sampling method	$\langle I \rangle_{\mathrm{AD},z_h,i}$		
Tower inter-spacing	$7D_0$		
U_∞ [m/s]	$[8, 10, 13, 16]$		
I_∞ [%]	$[5, 10, 15]$		
$\Delta U/U_\infty$ superposition method	$\Delta U/U_\infty = \sum_{i=1}^{N} \frac{\Delta U}{U_{\infty,i}} \frac{U_{\infty,i}}{U_\infty}$		

Figure C.3 shows the velocity deficit field, $\Delta U/U_\infty$, and the added turbulent intensity, I^+, at hub height for four MR2 turbines separated $7D_0$ and subjected to $U_\infty = 8$ m/s and $I_\infty = 5$ %. The top row consist of the reference RANS-AD simulation, and the second, third and fourth rows velocity fields are obtained through the analytical surrogate model by making use of the three different I_i^+ superposition models. Then, the wake profile is sampled at each turbine location and at the hypothetical location of a fifth turbine to evaluate the model performances.

It is observed that the I^+ superposition model **C** predicts best the velocity deficit at the location of a potential fifth aligned turbine. However, surprisingly, this model over-predicts I^+. In fact this over-prediction of I^+ triggers a faster wake recovery, thus resulting in a good approximation of the accumulated velocity deficit $\Delta U/U_\infty$.

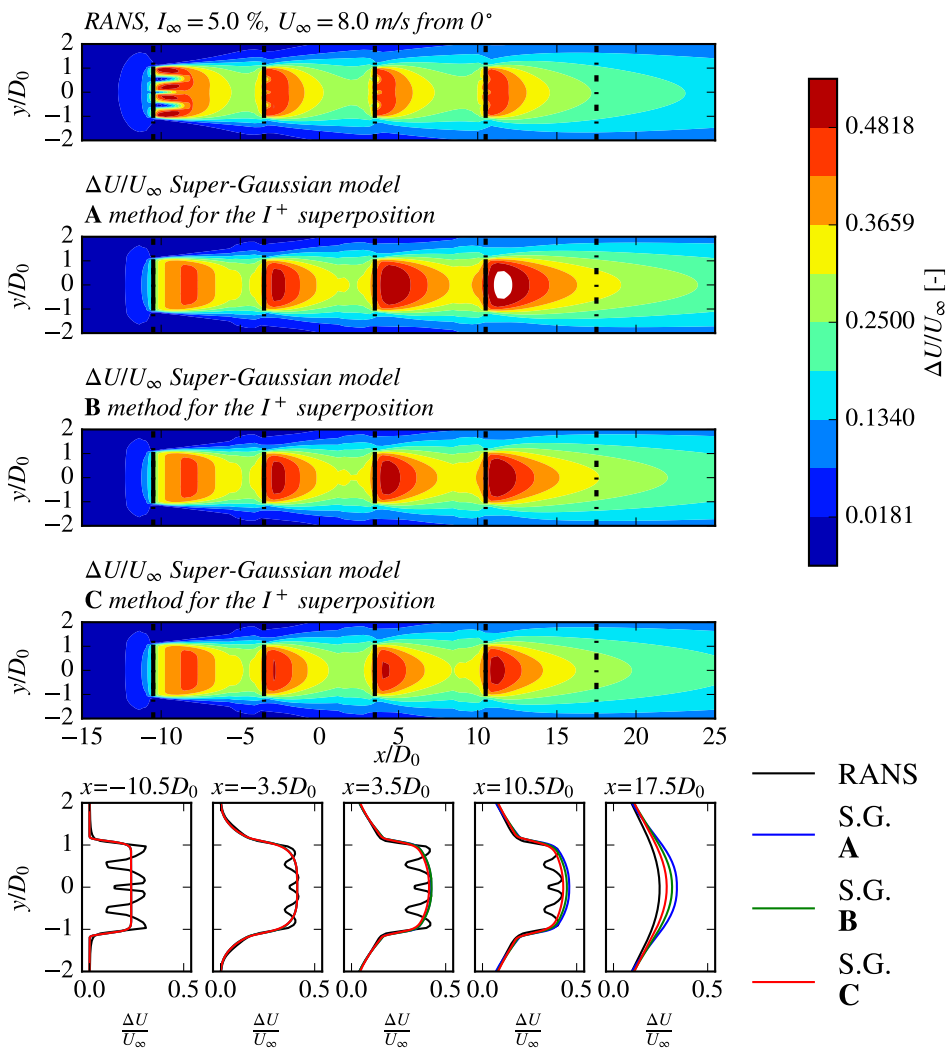

(a) $\Delta U/U_\infty$ profile on the $z = z_h$ plane.

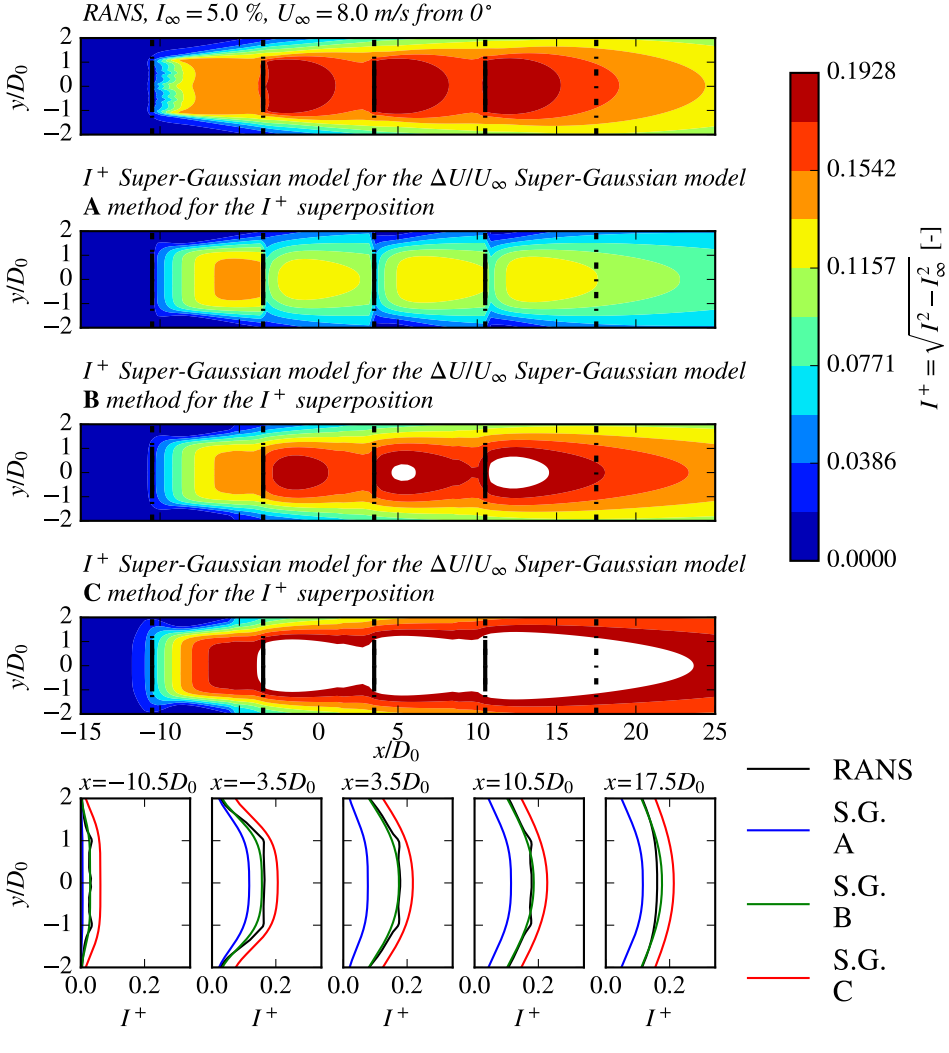

(b) I^+ profile on the $z = z_h$ plane.

Figure C.3: wake of four aligned MR2 turbines distanced $7D_0$ in between each other and subjected to $U_\infty = 8$ m/s and $I_\infty = 5\%$. On the left we observe the hub height velocity deficit, $\Delta U/U_\infty$, while the right side figures represent the added turbulence intensity at hub height. The top contour plots are obtained from RANS-AD simulations, the second, third and fourth row plots are obtained through the analytical surrogate model using the three different I_i^+ superposition methods. The white colouring means that the velocity deficit is out of the colour-bar scale.

In order to compare all three models along the evaluated range of U_∞ and I_∞, the mean squared error of each analytical velocity deficit field, $\Delta U/U_\infty$, is computed against the higher fidelity RANS simulation as per Equation C.1 and it is represented in Figure C.4. Analogously, the mean square error (MSE) of the added turbulence intensity field, I^+, is computed as

$$\mathrm{MSE}(I^+) = \frac{1}{40D}\int_{-15D}^{25D}\frac{1}{4D}\int_{-2D}^{2D}\left[I^+_{\mathrm{RANS}} - I^+_{\mathrm{Model}}\right]^2_{(x,y,z_h)}\,dy\,dx, \tag{C.2}$$

where $D \equiv D_0$, and I^+_{Model} corresponds to the added turbulence intensity obtained by the studied method (either A, B or C) at the location (x, y, z_h). The mean square error of all three methods is shown in Figure C.5 as a function of U_∞ and I_∞ at hub height. For all methods, the low U_∞ (high C_T) and low I_∞ case is the most challenging to predict its velocity deficit. As observed in Figure C.3b, the **B** superposition model predicts better I^+ however model **C** represents better the $\Delta U/U_\infty$ despite over-predicting I^+. The latter effect is related to the way we are representing the added turbulence intensity, $I^+ = \sqrt{I^2 - I_\infty^2}$, as introduced by [Crespo and Hernandez, 1996]. Nonetheless, if the turbulence intensity were to be computed as: $I^+ = I - I_\infty$, then the superposition method **C** may accurately represent I^+ and method **B** would be off. However, further studies are needed to evaluate its impact on $\Delta U/U_\infty$.

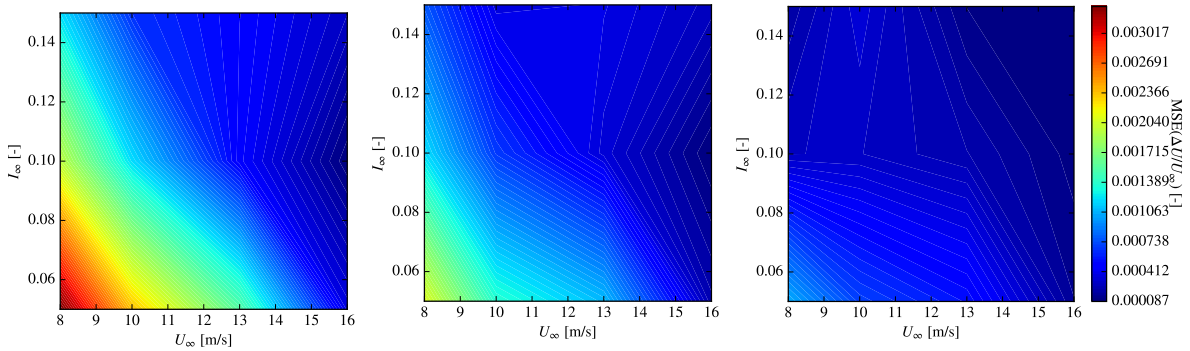

(a) Model **A**: $I^+ = I^+_i$.

(b) Model **B**: $I^+ = \sqrt{\sum_{i=1}^{N} I^2_{+,i}}$

(c) Model **C**: $I = I_\infty + \sqrt{\sum_{i=1}^{N} I^2_{+,i}}$

Figure C.4: mean square error (MSE) of the velocity deficit, $\Delta U/U_\infty$, of the super-Gaussian model computed with three different I^+_i superposition models compared to the higher fidelity RANS simulation at the plane $z = z_{\mathrm{hub}}$ for $-15 < x/D < 25$ and $-2 < y/D < 2$.

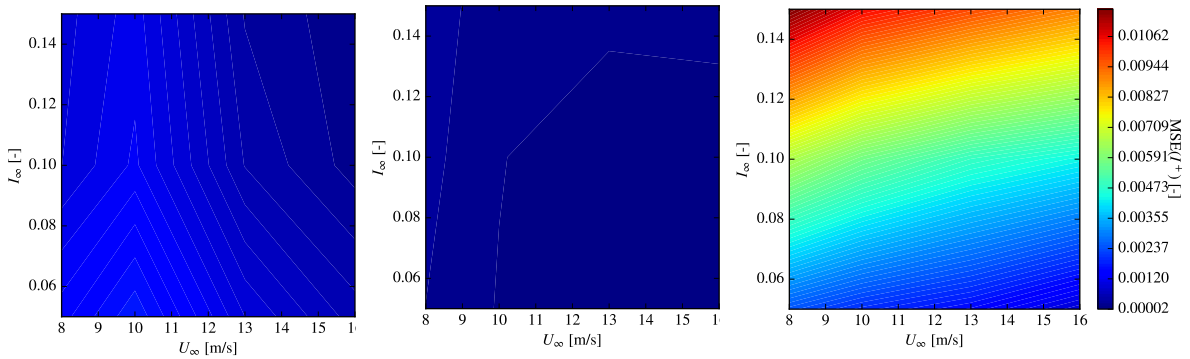

(a) Model **A**: $I^+ = I^+_i$.

(b) Model **B**: $I^+ = \sqrt{\sum_{i=1}^{N} I^2_{+,i}}$

(c) Model **C**: $I = I_\infty + \sqrt{\sum_{i=1}^{N} I^2_{+,i}}$

Figure C.5: mean square error (MSE) of the added turbulence intensity, I^+, of the super-Gaussian model computed with three different I^+_i superposition models compared to the higher fidelity RANS simulation at the plane $z = z_{\mathrm{hub}}$ for $-15 < x/D < 25$ and $-2 < y/D < 2$.

In Figure 3.2b of section 3.3 we noticed that the power produced by the MR2 turbine is more sensitive to velocity changes $U_{\infty,i}$ than to $I_{\infty,i}$, thus model **C** is selected since it approximate best the velocity field.

Hence, the added turbulence intensity of each turbine i, $I_{+,i}$, is superposed as

$$I = I_\infty + \sqrt{\sum_{i=1}^{N} I_{+,i}^2} \rightarrow I^+ = \sqrt{I^2 - I_\infty^2}. \tag{C.3}$$

C.3. $\Delta U/U_\infty$ superposition model

In a wind farm context, inner wind-turbines are often shaded by upstream turbines and their wakes merge together. The present section evaluates the following two velocity deficit, $\Delta U/U_\infty$, superposition models:

- **Linear sum**: proposed by [Voutsinas et al., 1990], where each individual velocity deficit obtained from the look up table is superposed as:

$$\frac{\Delta U}{U_\infty} = \sum_{i=1}^{N} \left[\frac{\Delta U}{U_{\infty,i}}\right] \frac{U_{\infty,i}}{U_\infty}, \tag{C.4}$$

  where N is the total number of MR2 turbines.

- **Sum of squares**: proposed by [Niayifar and Porté-Agel, 2016], where each individual velocity deficit is superposed as

$$\frac{\Delta U}{U_\infty} = \sqrt{\sum_{i=1}^{N} \left\{\left[\frac{\Delta U}{U_{\infty,i}}\right] \frac{U_{\infty,i}}{U_\infty}\right\}^2}. \tag{C.5}$$

Both methods claim to conserve some properties of the flow, for instance the linear sum claims to conserve the flow momentum, while the sum of squares claims to conserve the energy of the flow. Nevertheless, these relationships haven't been proved so far [Bastankhah et al., 2021].

Four MR2 turbines spaced $7D_0$ are modelled with two different $\Delta U/U_\infty$ superposition models and compared to higher fidelity RANS-AD models. The used parameters are detailed in Table C.3, where both I_i^+ and $[\Delta U/U_{\infty,i}]$ are obtained from the look-up tables of the super-Gaussian model fitted in chapter 3.

Table C.3: analytical surrogate model setup to test different $\Delta U/U_\infty$ superposition models.

$\Delta U/U_\infty$ superposition method	Linear sum $\sum_{i=1}^{N}\left[\frac{\Delta U}{U_{\infty,i}}\right]\frac{U_{\infty,i}}{U_\infty}$	Sum of squares $\sqrt{\sum_{i=1}^{N}\left\{\left[\frac{\Delta U}{U_{\infty,i}}\right]\frac{U_{\infty,i}}{U_\infty}\right\}^2}$
$U_{\infty,i}$ sampling method	$\langle U\rangle_{\mathrm{AD},z_h,i}$	
$I_{\infty,i}$ sampling method	$\langle I\rangle_{\mathrm{AD},z_h,i}$	
Tower inter-spacing	$7D_0$	
U_∞ [m/s]	$[8,10,13,16]$	
I_∞ [%]	$[5,10,15]$	
I^+ superposition method	$I = I_\infty + \sqrt{\sum_{i=1}^{N} I_{+,i}^2} \rightarrow I^+ = \sqrt{I^2 - I_\infty^2}$	

Figure C.6 shows the velocity deficit, $\Delta U/U_\infty$, at hub height of a RANS simulation and the two studied velocity superposition method for $U_\infty = 8$ m/s and $I_\infty = 10$ %. Then, both models are compared against the higher fidelity RANS results and the mean squared error in between the surrogate model and the RANS model velocity deficit is computed as per Equation C.1.

Figure C.7 shows the mean square error for the whole range of U_∞ and I_∞ studied. It is observed that the sum of squares model under-predicts the velocity deficit, thus the linear sum is chosen due to its lower mean squared error in comparison to the RANS simulations. The observed behaviour is aligned with the drawn conclusion of [Crespo et al., 1999] who observe that the linear sum estimated a greater velocity deficit than the quadratic sum.

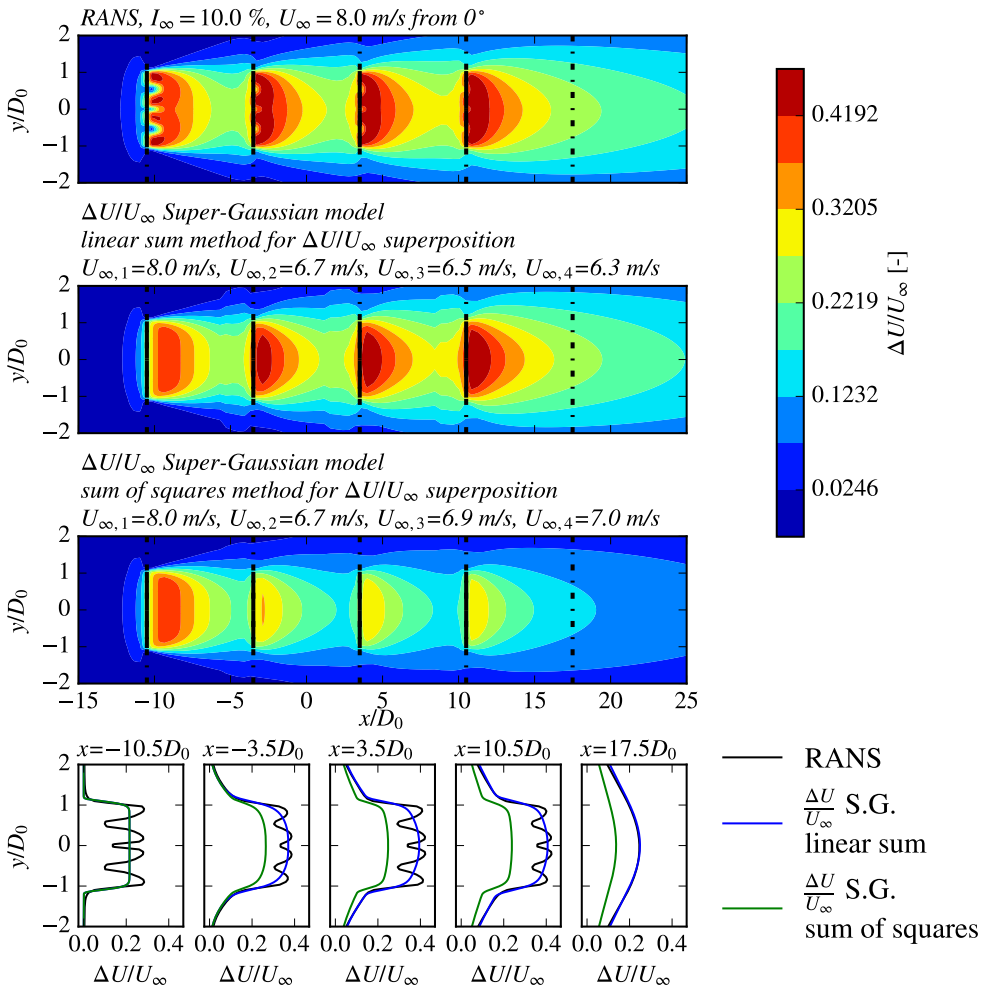

Figure C.6: hub height velocity deficit, $\Delta U/U_\infty$, for four MR2 turbines separated $S = 7D_0$ from each other and subjected to $U_\infty = 8$ m/s and $I_\infty = 10\%$ at hub height. The top contour plot is obtained from RANS-AD simulations, the second and third are obtained through the analytical surrogate model using two different velocity superposition methods.

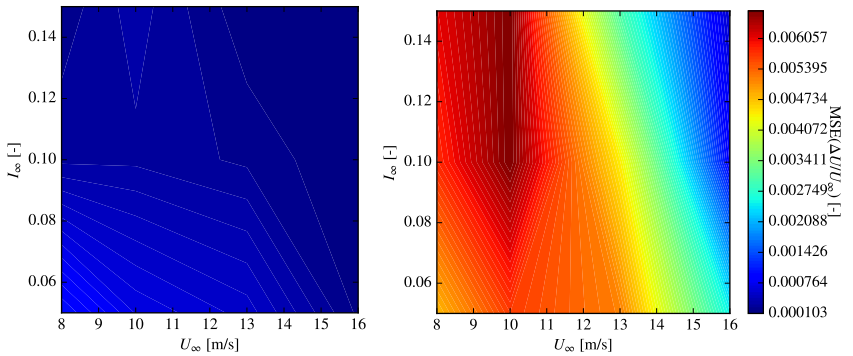

(a) Linear sum model. **(b)** Sum of squares model.

Figure C.7: mean square error (MSE) of the velocity deficit, $\Delta U/U_\infty$, predicted by the super-Gaussian model computed with two different superposition models compared to the higher fidelity RANS simulation at the plane $z = z_{\text{hub}}$ for $-15 < x/D < 25$ and $-2 < y/D < 2$.

D

Multi-rotor wind farm model vs RANS, additional results

The present appendix compiles all the results obtained from analyzing a 3×3 MR2 wind farm composed of 2R-V29 multi-rotor turbines uniformly spaced a distance $S = [5, 7]D_0$, subjected to $I_\infty = 5\%$ and a range of $U_\infty = [8, 10, 13, 16]$ m/s at hub height.

Figure D.1 shows the wind farm efficiency as a function of the wind direction for a range of wind speeds for a turbine inter-spacing $S = 5D_0$. The $U_\infty = 16$ m/s case isn't plotted since most of the turbines operate at rated power.

The relative error compared to the RANS simulations is computed as:

$$E_{\text{model}}(\text{WD}) = \frac{\sum_{i=1}^{N} P_{\text{model},i}(\text{WD}) - \sum_{i=1}^{N} P_{\text{RANS},i}(\text{WD})}{\sum_{i=1}^{N} P_{\text{RANS},i}(\text{WD})}, \tag{D.1}$$

where N is the total amount of wind turbines and P_i refers to the power produced by the i^{th} turbine. Then, the average value is computed as

$$E_{\text{model, AVG}} = \frac{\sum_{\text{WD}=1^\circ}^{360^\circ} \left[\sum_{i=1}^{N} P_{\text{model},i}(\text{WD}) - \sum_{i=1}^{N} P_{\text{RANS},i}(\text{WD})\right]}{\sum_{\text{WD}=1^\circ}^{360^\circ} \sum_{i=1}^{N} P_{\text{RANS},i}(\text{WD})}, \tag{D.2}$$

hence, first computing the average power produced by the wind farm along all the wind directions and then computing the relative difference in between the averaged power obtained by the surrogate model and the RANS simulations.Table D.1 compares the super- and double-Gaussian LUT models, the Park2 and the turbo-Gaussian-deficit models against higher fidelity RANS results for the characteristic distance $S = 5D_0$, which wind-farm efficiency is shown in Figure D.1. Analogously, Table D.2 compares the models for the characteristic distance $S = 7D_0$ shown in Figure D.2.

Table D.1: E_{model} [%] and $E_{\text{model, AVG}}$ [%] for the $3 \times 3 \times$MR2 layout with $S = \mathbf{5}D_0$.

		Double-Gassian LUT				Super-Gassian LUT				Park2				Turbo-Gaussian			
	U_∞ [m/s]	8	10	13	16	8	10	13	16	8	10	13	16	8	10	13	16
Wind direction [°]	270	-1.1	-0.7	0.2	-0.4	-1.2	-0.8	0.1	-0.3	-20.9	-16.3	-0.9	-3.3	-36.6	-37.1	-28.9	-4.5
	280	-2.4	-1.9	0.0	0.2	-2.8	-2.6	-0.5	0.3	-17.3	-14.3	-4.8	-2.3	-16.2	-15.8	-9.6	-2.2
	290	-1.3	-1.6	-0.7	0.2	-2.0	-2.4	-0.9	0.2	-14.7	-12.3	-5.3	-2.0	-15.5	-14.1	-6.7	-2.0
	300	-0.5	-0.8	-1.1	0.1	-1.4	-1.5	-1.2	0.1	-14.4	-12.2	-5.1	-2.1	-12.3	-10.7	-5.4	-2.1
	310	-0.2	-0.5	-1.1	0.2	-0.4	-0.7	-1.1	0.2	-17.3	-14.6	-5.5	-2.1	-15.0	-13.1	-5.8	-2.1
	320	-0.4	-0.8	-1.2	0.2	-0.6	-0.9	-1.2	0.2	-17.4	-14.8	-5.6	-2.1	-15.1	-13.2	-5.9	-2.1
	330	-0.6	-0.7	-1.0	0.1	-1.4	-1.5	-1.2	0.1	-14.4	-12.2	-5.1	-2.1	-12.4	-10.7	-5.4	-2.1
	340	-1.2	-1.5	-0.7	0.2	-1.9	-2.2	-0.9	0.2	-14.6	-12.2	-5.3	-2.0	-15.3	-13.9	-6.7	-2.0
	350	-2.2	-1.7	0.1	0.2	-2.6	-2.3	-0.4	0.3	-17.1	-14.0	-4.6	-2.3	-16.0	-15.5	-9.5	-2.2
	AVG	-1.1	-1.1	-0.6	0.1	-1.6	-1.7	-0.8	0.1	-16.3	-13.5	-4.8	-2.3	-16.6	-15.3	-9.1	-2.4

Table D.2: E_{model} [%] and $E_{\text{model, AVG}}$ [%] for the 3 × 3×MR2 layout with $S = \mathbf{7}D_0$.

		Double-Gassian LUT				Super-Gassian LUT				Park2				Turbo-Gaussian			
	U_∞ [m/s]	8	10	13	16	8	10	13	16	8	10	13	16	8	10	13	16
Wind direction [°]	270	-0.2	-0.7	-1.2	-0.6	-0.7	-1.1	-1.3	-0.6	-22.3	-18.6	-3.2	-3.4	-40.3	-40.6	-29.5	-4.1
	285	-0.7	-1.2	-1.2	0.2	-1.0	-1.6	-1.2	0.3	-14.1	-12.2	-5.6	-1.8	-11.1	-9.6	-5.3	-1.8
	300	-0.2	-0.5	-1.1	0.1	-0.4	-0.6	-1.1	0.1	-12.2	-10.6	-5.4	-1.9	-14.7	-13.7	-7.2	-1.9
	315	0.4	0.3	-1.3	-0.0	0.4	0.3	-1.4	-0.0	-16.2	-13.1	-5.0	-2.4	-30.2	-29.6	-18.1	-2.4
	330	-0.2	-0.4	-1.1	0.1	-0.4	-0.5	-1.1	0.1	-12.2	-10.5	-5.4	-1.9	-14.6	-13.6	-7.1	-1.9
	345	-0.6	-1.1	-1.2	0.2	-0.9	-1.4	-1.2	0.3	-14.1	-12.1	-5.6	-1.8	-10.8	-9.3	-5.3	-1.8
	AVG	-0.3	-0.6	-1.1	0.0	-0.5	-0.8	-1.2	0.0	-14.8	-12.6	-5.1	-2.2	-19.2	-18.3	-11.9	-2.3

As a general observation, all the models under-estimate the wind farm efficiency and the surrogate models based on look-up tables are an order of magnitude more accurate than the traditional engineering models i.e. Park2 and turbo-Gauss.

As expected, the LUT surrogate models present a wind direction rotational symmetry of 45° since they do not represent the rotation of the wake, and their higher discrepancies with RANS occurs when rotors are non-uniformly loaded. The latter condition happens when down-wind turbines operates partially in the wake of upstream turbines. The surrogate LUT models fail to represent the asymmetrical loading that takes place while partially operating in the wake of an upwind turbine since the higher-order Gaussian function and the double-Gaussian function selected as base functions for the surrogate model are both even functions and the model is trained under a uniform atmospheric surface layer profile.

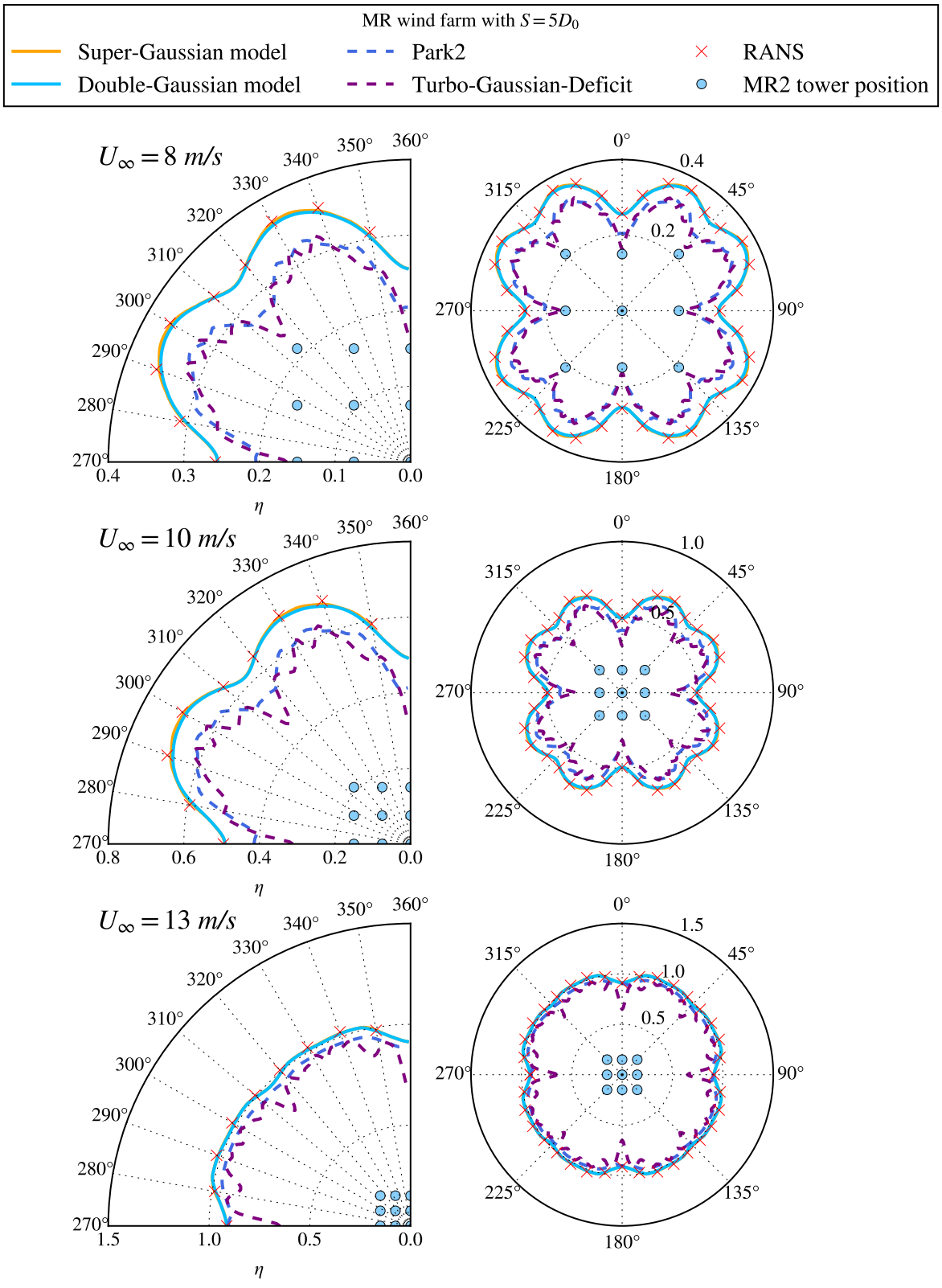

Figure D.1: efficiency of a 3 MR2 wind farm with 2R-V29 turbines spaced $S = \mathbf{5}D_0$. Results obtained from both super- and double-Gaussian LUT models, Park2 and turbo-Gaussian deficit model. All surrogate models are compared against higher order RANS-AD simulations (red crosses) and the MR2 wind farm layout is sketched in cyan.

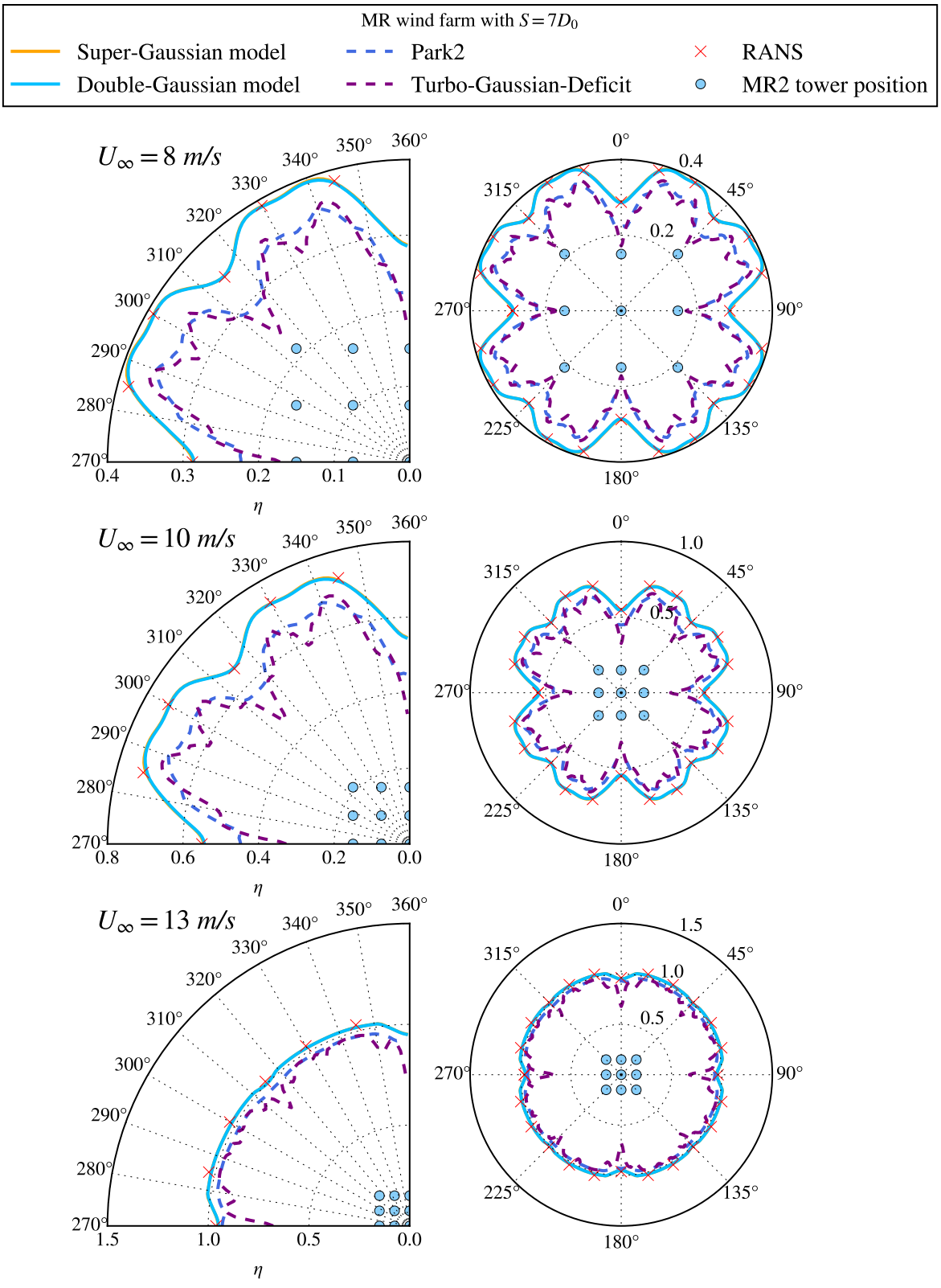

Figure D.2: efficiency of a 3 MR2 wind farm with 2R-V29 turbines spaced $S = 7D_0$. Results obtained from both super- and double-Gaussian LUT models, Park2 and turbo-Gaussian deficit model. All surrogate models are compared against higher order RANS-AD simulations (red crosses) and the MR2 wind farm layout is sketched in cyan.